Max-Planck-Institut
für Meteorologie

MAX PLANCK
GESELLSCHAFT

International Max Planck Research School
on Earth System Modelling

A new Eulerian iceberg module for climate studies:

Formulation and application to the investigation of the sensitivity of the AMOC to iceberg calving

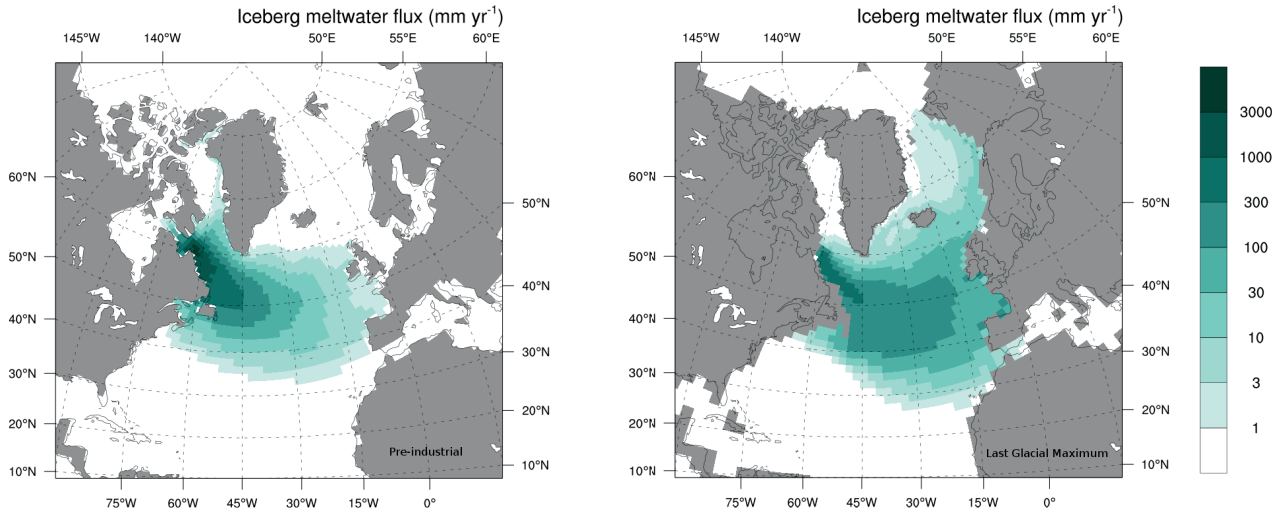

Olga Erokhina

Hamburg 2020

Berichte zur Erdsystemforschung
Reports on Earth System Science

238
2020

Hinweis

Die Berichte zur Erdsystemforschung werden vom Max-Planck-Institut für Meteorologie in Hamburg in unregelmäßiger Abfolge herausgegeben.

Sie enthalten wissenschaftliche und technische Beiträge, inklusive Dissertationen.

Die Beiträge geben nicht notwendigerweise die Auffassung des Instituts wieder.

Die "Berichte zur Erdsystemforschung" führen die vorherigen Reihen "Reports" und "Examensarbeiten" weiter.

Notice

The Reports on Earth System Science are published by the Max Planck Institute for Meteorology in Hamburg. They appear in irregular intervals.

They contain scientific and technical contributions, including Ph. D. theses.

The Reports do not necessarily reflect the opinion of the Institute.

The "Reports on Earth System Science" continue the former "Reports" and "Examensarbeiten" of the Max Planck Institute.

Anschrift / Address

Max-Planck-Institut für Meteorologie
Bundesstrasse 53
20146 Hamburg
Deutschland

Tel./Phone: +49 (0)40 4 11 73 - 0
Fax: +49 (0)40 4 11 73 - 298

name.surname@mpimet.mpg.de
www.mpimet.mpg.de

Layout

Bettina Diallo and Norbert P. Noreiks
Communication

Copyright

A new Eulerian iceberg module for climate studies:

Formulation and application to the investigation of the sensitivity of the AMOC to iceberg calving

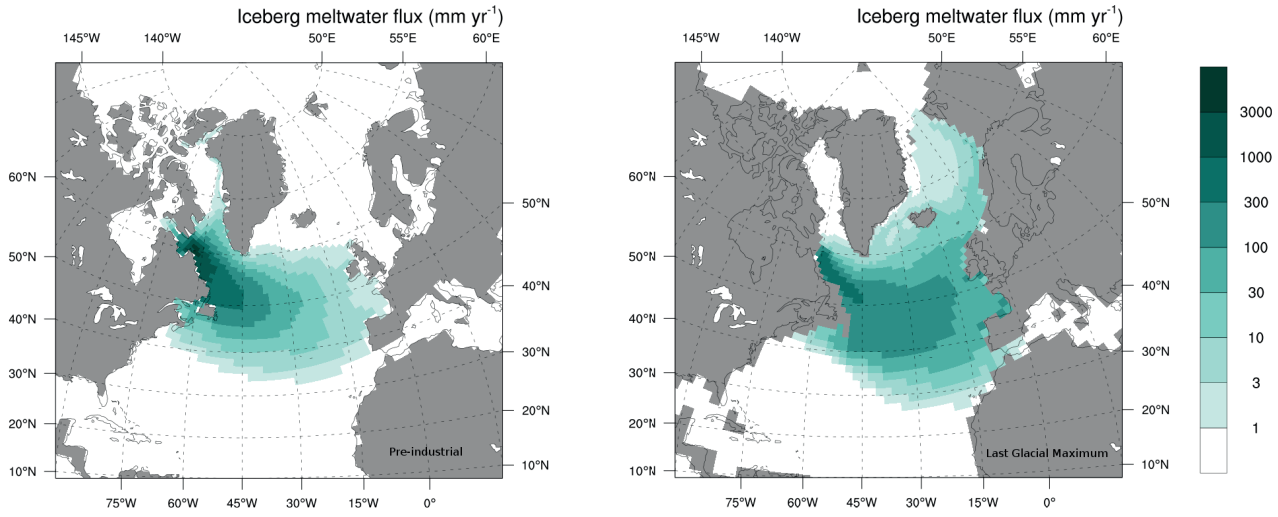

Olga Erokhina

Hamburg 2020

Olga Erokhina
aus Moskau, Russland

Max-Planck-Institut für Meteorologie
The International Max Planck Research School on Earth System Modelling
(IMPRS-ESM)
Bundesstrasse 53
20146 Hamburg

Universität Hamburg
Geowissenschaften
Meteorologisches Institut
Bundesstr. 55
20146 Hamburg

Tag der Disputation: 27. Oktober 2020

Folgende Gutachter empfehlen die Annahme der Dissertation:
Dr. Uwe Mikolajewicz
Prof. Dr. Gerhard Schmiedl

Vorsitzender des Promotionsausschusses:
Prof. Dr. Dirk Gajewski

Dekan der MIN-Fakultät:
Prof. Dr. Heinrich Graener

Berichte zur Erdsystemforschung / Max-Planck-Institut für Meteorologie 238
Reports on Earth System Science / Max Planck Institute for Meteorology 2020

ISSN 1614-1199

Abstract

Although it is well known that icebergs play an important role especially for the simulation of glacial climate, e.g. Heinrich events, standard climate models, as used in the Climate Model Intercomparison Project (CMIP), do not contain iceberg modules. Existing iceberg modules are formulated in the Lagrangian framework, optimal for tracking individual icebergs. However, in climate modelling, the key aspect of icebergs is the effect of their melting on the ocean. Therefore, a new formulation of an iceberg module in the Eulerian framework is presented. The module is introduced into the Max Planck Institute Earth System Model (MPI-ESM), allowing to simulate the effect of icebergs on the climate and feedbacks between them. The new iceberg module is tested in a set of simulations with the iceberg module coupled to the ocean component of MPI-ESM with prescribed observed iceberg calving fluxes. These simulations allow to validate the model against observed iceberg distributions. The sensitivity of the iceberg module against several model parameters is tested, and an optimal set of parameters, focusing on the iceberg meltwater flux as key variable, is determined.

The effect of icebergs on the simulation of iceberg discharge events is investigated in a set of simulations with the full MPI-ESM-Iceberg set-up. The experiments aim at determining the thresholds of the Atlantic Meridional Overturning Circulation (AMOC) against a prescribed hosing. In a setting with slowly varying forcing, different types of hosing are compared. In addition to a direct simulation of iceberg calving through the Hudson Strait, two freshwater hosing experiments are performed: a direct point source hosing in the Labrador Sea off the Hudson Strait and a latitude belt hosing between 50° and 70°N. For pre-industrial climate conditions, the results show that the sensitivity of the AMOC to the type of hosing is considerable. The threshold for an abrupt AMOC weakening in the latitude belt hosing is approximately four times lower than in the point source hosing in the Labrador Sea. The threshold for the iceberg experiment lies approximately in the middle of the values for the two freshwater hosing experiments.

A similar set of experiments under climate conditions representative for the Last Glacial Maximum (LGM; 21000 year before present) was performed to investigate the effect of the background climate on the aforementioned

results. For this climate state, the simulated mechanism of the formation of North Atlantic Deep Water (NADW) is different as compared to pre-industrial conditions. In the LGM simulations, NADW is formed in the Arctic and the Nordic Seas due to brine release from sea ice. This makes the AMOC more resilient against the iceberg/freshwater hosing and no abrupt transitions between a strong and a weak AMOC are simulated. The spread between the different types of hosing in the cold LGM climate is much smaller than for pre-industrial climate.

Further experiments were performed to investigate the effect of latent heat of icebergs on the AMOC sensitivity. While the effect of the latent heat is much smaller than the direct effect of the iceberg meltwater flux, it has a significant impact on the AMOC. Due to the latent heat of icebergs, the uppermost layers of the ocean, where melt takes place, cool. This reduces the iceberg melt and prolongs the lifetime of icebergs, allowing them to travel further away from the source region. This enhances iceberg melt in the north-eastern North Atlantic where it affects the deep water formation. The cooling occurring is a consequence of the strong hosing, and the resulting weak AMOC has a qualitatively similar effect on the distribution of the iceberg meltwater flux.

In a long-term transient simulation with the MPI-ESM-Iceberg set-up that is coupled to an ice sheet and solid earth models, the Eulerian iceberg module demonstrates its ability to simulate Heinrich events and resulting changes in iceberg meltwater distribution. The pattern of iceberg meltwater flux compares well with the reconstructed distribution of ice rafted debris from deep-sea sediment cores in the North Atlantic.

To sum up, a computationally cheap way to introduce icebergs in a standard ESM has been presented, and its suitability for long-term simulations has been demonstrated. The results presented in this thesis emphasize that for hosing experiments and long-term transient simulations of glacial and deglacial climate, a direct simulation of icebergs is necessary.

Zusammenfassung

Obwohl es allgemein bekannt ist, dass Eisberge eine wichtige Rolle für die Simulation des Glazialklimas spielen (z.B. bei Heinrich Events), wird deren Effekt in den Klimamodellen des Climate Model Intercomparison Projects (CMIP) ignoriert. Die bisher existierenden Eisbergmodule sind im Lagrangeschen Referenzsystem formuliert. Dieses Referenzsystem ist ideal zum Verfolgen von individuellen Eisbergen. Der Haupteffekt von Eisbergen auf das Klimasystem ist jedoch das Hinzufügen von Frischwasser durch Schmelzen. In dieser Arbeit, präsentiere ich ein neues Eisbergmodul im Eulerschen Referenzsystem. Dieses Eisbergmodul wird dem Max Planck Institute Earth System Model (MPI-ESM) hinzugefügt und erlaubt es nun, den Effekt von Eisbergen auf das Klima und Rückkopplungseffekte zwischen diesen beiden Komponenten zu untersuchen. Das neue Modul wird in einer Reihe von gekoppelten Simulationen mit dem MPI-OM Ozeanmodell mit vorgeschriebenen beobachteten Eisbergkalbungsflüssen getestet. Diese Simulationen erlauben es, das neue Model mit beobachteten Eisbergverteilungen zu vergleichen. Weiterhin wird die Sensitivität des Eisbergmoduls gegenüber der Wahl mehrerer Modelparameter getestet. Hierbei wird ein Satz optimaler Modelparameter mit dem Fokus auf einen plausiblen Eisbergschmelzwasserfluss ermittelt.

Der Effekt von Eisbergen im Zuge starker Eisbergkalbungsereignisse(z.B. Heinrichereignisse) wird in einer Reihe von Simulationen mit dem kompletten MPI-ESM-Eisberg Setup untersucht. In diesem Satz von Experimenten werden kritische Grenzwerte der Sensitivität der Atlantischen Meridionalen Umwälzzirkulation (AMOC) fgegenüber Frischwasserzufuhr bestimmt. Daher wird die Frischwasserzufuhr in allen Experimenten langsam verändert, wobei verschiedene Methoden der Frischwasserzufuhr miteinander verglichen werden. Zusätzlich zu einer Simulation, in der die Frischwasserzufuhr durch Eisberge in der Hudsonstraße erfolgt, werden noch zwei weitere Methoden der Frischwasserzufuhr untersucht. Zum Einen eine Punktquelle in der Labradorsee in der Nähe der Hudsonstraße und zum Anderen ein konstanter Frischwassereintrag zwischen 50 und 70 Grad Nord. Die Ergebnisse für vorindustrielle Klimabedingungen zeigen, dass die Sensitivität der AMOC sehr stark von der Methode der Frischwasserzufuhr abhängt. Der Grenzwert für eine abrupte Abschwächung der AMOC in dem Experiment mit einem konstanten Frischwassereintrag zwischen 50 und 70 Grad

Nord ist viermal niedriger als für das Experiment mit der Punktquelle in der Labradorsee. Der Grenzwert für das Eisbergexperiment liegt ungefähr in der Mitte der beiden anderen Frischwasserzufuhrexperimente.

Eine Reihe ähnlicher Experimente mit Klimabedingungen repräsentativ für das Letzte Glaziale Maximum (LGM, vor 21,000 Jahren) wurde durchgeführt um den Effekt des Hintergrundklimas auf die vorherigen Resultate zu untersuchen. Der Mechanimus der nordatlantischen Tiefenwasserbildung (NADW) ist deutlich unterschiedlich im Vergleich zum vorindustriellen Experiment. Unter LGM Bedingungen, findet die Bildung von NADW im arktischen Mittelmeer und im europäischen Nordmeer statt aufgrund von Salzlakenfreisetzung während der Meereisbildung. Dieser Prozess führt dazu, dass die AMOC in diesen Eperimenten widerstandsfähiger gegenüber Frischwasserzufuhr ist und kein abrupter Zusammenbruch der AMOC auftritt. Der Unterschied zwischen den verschiedenen Methoden der Frischwasserzufuhr ist auch deutlich geringer als unter vorindustriellen Klimabedingungen.

Eine Reihe weiterer Experimente wurde durchgeführt um den Effekt der Wärme des Eisbergschmelzens und dessen Auswirkung auf die AMOC zu untersuchen. Obwohl der Effekt der latenten Wärme deutlich geringer ist als der direkte Effekt des Eisbergschmelzwasserflusses, spielt er doch eine wichtige Rolle für die AMOC. An dem Ort, an dem die Eisberge schmelzen, führt die latenten Wärme der Eisberge zu einer Abkühlung der obersten Ozeanschichten. Dieser Prozess reduziert die Schmelzrate und verlängert zugleich die Lebenszeit der Eisberge, die weiter weg von ihrem Entstehungsgebiet getrieben werden können. Der Transport über eine größere Entfernung führt zu einem verstärkten Schmelzen von Eisbergen in dem östlichen und nördlichen Teil des Nordatlantiks, wo es Einfluss auf die Tiefenwasserbildung nimmt. Ein Abkühlen als Konsequenz der starken Frischwasserzufuhr und einer daraus resultiertenden schwachen AMOC hat einen ähnlichen Effekt.

In einer langen transienten Simulation (ca. 40,000 Jahre) mit dem MPI-ESM-Eisberg Setup und interaktiven Eisschild- und Geodynamikmodell konnte getestet werden, ob das Eisbergmodul Heinrichereignisse und damit in Verbindung stehende Eisbergkalbungsereignisse erfolgreich simulieren kann. Die Eisbergverteilung in der Simulation liefert hierbei gute Vergleichswerte mit aus marinen Sedeimentbohrkernen abgeleiteten Eisbergverteilungen aus dem Nordatlantik.

Zusammenfassend wurde in dieser Arbeit ein effizientes und schnelles Eisbergmodul in ein bestehes Erdsystemmodell implementiert. Die Ef-

fizienz des Moduls erlaubt es lange (>40,000 Jahre) Simulationen durchzuführen. Die hier vorgestellten Resultate heben die Wichtigkeit der Methode der Frischwasserzufuhr hervor und betonen die Notwendigkeit der expliziten Modellierung von Eisbergen für Kalbungsexperimente und lange Simulationen mit glazialem Klima.

Contents

1 Introduction

Past rapid climate changes associated with a significant cooling in the North Atlantic have fascinated geologists and climate modellers for a long time. One key mechanism often involved to explain rapid cooling events in the North Atlantic realm are changes in the Atlantic Meridional Overturning Circulation (AMOC) and the associated changes in northward ocean heat transport. Examples of such events are Heinrich events (HEs, Heinrich, 1988). Evidence of HEs can be found in the form of ice rafted debris (IRD, mineral grains comparable in size to sand which are transported by icebergs and released to the ocean during iceberg melt) layers in large parts of the North Atlantic. Several events have occurred during glacial times. The standard interpretation is that they are discharge of huge amount of icebergs (e.g., Heinrich, 1988).

1.1 Observational evidence of past ocean circulation changes

The AMOC is responsible for a large fraction of heat transport from the South to the North Atlantic (e.g. Broecker, 1991). It consists of two cells, the upper North Atlantic Deep Water (NADW) cell with present-day deep water formation in the Nordic Seas, and the lower Antarctic Atlantic Bottom Water (AABW) cell where present-day bottom water forms in the Weddell Sea. Paleo records allow in parts reconstructing past changes in water mass properties and the ocean circulation (e.g., Broecker et al., 1988; Sarnthein et al., 1995; Voigt et al., 2017; Böhm et al., 2015).

Paleo records indicate that since the last glacial period, the AMOC underwent three different states, namely, a warm, a cold and a weak mode (e.g., Sarnthein et al., 1995; Rahmstorf, 2002; Lynch-Stieglitz, 2017). During the Holocene, the AMOC was in the warm mode, which is characterized by a deep NADW cell with deep water formation mostly in the Nordic Seas (Greenland, Icelandic and Norwegian Seas), but also in the Labrador Sea and Irminger Sea. The glacial AMOC was in a cold mode with a much shallower NADW cell and deep water formation in the open North Atlantic. AABW expanded further to the north and the margin between the AABW and NADW cell was shifted upwards in comparison with the present state. The third state was a weak mode without deep water formation in the North Atlantic. AABW was filling the deep and mid-depth Atlantic basin

up to 1,000 m (Clark et al., 2002; Rahmstorf, 2002). The transition from the glacial to the interglacial was interrupted by a number of abrupt changes of the AMOC resulting in alterations between these modes (e.g., Broecker et al., 1988; Rahmstorf, 2002). The warm and the cold AMOC modes will be referred to as a strong mode in the following.

A widely used method to reconstruct sea surface temperatures (SST) is based on the composition of foraminiferas in a sediment core, e.g. the increase of species *Neogloboquadrina pachyderma (N. pachyderma)* indicates cold SSTs (e.g., Broecker et al., 1988). The oxygen isotopic composition $\delta^{18}O$ in foraminiferas, the ratio between the oxygen isotopes ^{18}O and ^{16}O, reveal changes in the temperature-salinity regime of the upper ocean (e.g., Sarnthein et al., 1995). Low values of $\delta^{18}O$ are indicative of warm and/or less saline water that points towards presence of glacial meltwater. The ratio between carbon isotopes ^{13}C and ^{12}C, $\delta^{13}C$, is an indicator of nutrient distribution and is used as a water mass tracer (e.g., Voigt et al., 2017). Newly formed water has high $\delta^{13}C$, close to the atmospheric value, that decreases with the remineralization of $\delta^{13}C$ depleted organic carbon, releasing nutrients. High $\delta^{13}C$ values are typical for the NADW, whereas extremely low $\delta^{13}C$ values are typical for AABW water masses. The latter depicts large nutrients accumulation and is often interpreted as being indicative of an AMOC with suppressed NADW formation and AABW filling in the North Atlantic (e.g., Lynch-Stieglitz, 2017; Voigt et al., 2017). The AMOC strength can be reconstructed, e.g. from the ^{231}Pa/^{230}Th, the ratio between protactinium and thorium isotopes that is a product of uranium decay homogeneously distributed in the ocean (e.g., Yu et al., 1996; McManus et al., 2004; Voigt et al., 2017). The residence time of ^{230}Th is much shorter than the residence time of ^{231}Pa which allows farther ^{231}Pa advection by ocean currents and, therefore, an estimation the circulation strength. A weak AMOC is characterized by high values of ^{231}Pa/^{230}Th as a result of small ^{231}Pa transport. Different studies reveal contradictory glacial AMOC strength that is attributed to uncertainties in ^{231}Pa/^{230}Th sedimentary (e.g., Yu et al., 1996; McManus et al., 2004). The uncertainties can be reduced by accounting for ϵNd, a neodymium isotope (^{143}Nd/^{144}Nd), that allows a tracing of the origin of the water mass. Low ϵNd values are typical for the NADW (e.g., Böhm et al., 2015; Lynch-Stieglitz, 2017). Overall, geochemical proxies indicate that during the Last Glacial Maximum (LGM; nearly 21,000 yrs before present (BP)), the ocean water was colder, the NADW cell was shallower with deep water formation in the open North Atlantic,

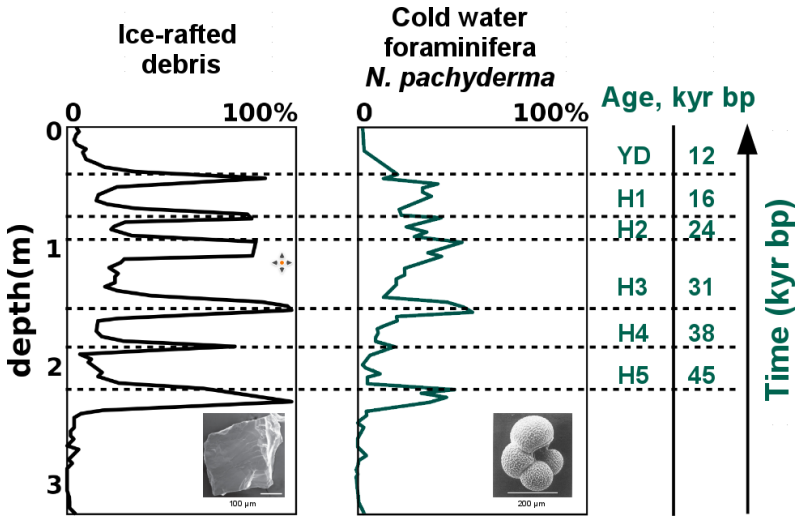

Figure 1.1: Core record of M01-032 at 47°34.7'N 18°56.0'W (Heinrich, 1988). Abundance of IRD (left) and foraminifera *N.pachyderma* (right) in the core. The amount of IRD is given as part of the total split. The amount of *N.pachyderma* species is given as part of the sum of planktonic foraminiferas in a split. Left axis denotes the depth, right axis denotes age in 1,000 years before present (kyr bp). YD is the Younger Dryas event, H1-H5 are Heinrich events. IRD figure (left) is from Stickley et al. (2009). *N.pachyderma* figure (right) is from Kohfeld et al. (1996).

and the AMOC strength was close to modern values (e.g., Sarnthein et al., 1995; Yu et al., 1996; Alley and Clark, 1999; Lynch-Stieglitz, 2017).

Deep-sea sediment cores from the coast of Portugal and other places in the North Atlantic reveal a number of abrupt climate changes, i.e. when the AMOC collapsed to a weak mode (e.g., Ruddiman, 1977; Broecker et al., 1988). These events are most obvious from an increased amount of IRD (Fig. 1.1, Heinrich, 1988). They are known as Heinrich or Hudson Strait Heinrich events (Ruddiman, 1977; Heinrich, 1988; Broecker et al., 1988; Bond et al., 1992; Alley and Clark, 1999; Andrews and Voelker, 2018), and interpreted as massive iceberg discharge events. HEs have a typical duration of a few hundreds to a thousand years with a typical recurrence time of roughly 7,000 years. One of the suggested mechanisms was iceberg release from an oscillating ice sheet (MacAyeal, 1993; Bond and Lotti, 1995; Dowdeswell et al., 1995). A decade before HEs were explained, Ruddiman (1977) mapped the spatial disposition of IRD, also known as Ruddiman belt, between 46° to 50°N in the Northern Atlantic. It was shown that the thicknesses of IRD layers in cores decreased eastwards with increasing distance from the Hudson Straight, indicating that the main origin of icebergs was the Laurentide ice sheet and that icebergs crossed the North Atlantic from west to east reaching the Iberian peninsula in the past (Ruddiman, 1977;

Heinrich, 1988; Dowdeswell et al., 1995). The IRD maxima also coincided with an increase in abundance of *N.pachyderma* and, hence, indicating surface cooling (Fig. 1.1, Heinrich, 1988). Simultaneous ocean cooling and a weak AMOC mode indicates that iceberg release and suppression of NADW formation are correlated. Overall, Heinrich (1988) identified six such events over the last 100,000 years. Estimates of the solid discharge from the Laurentide ice sheet during HEs from modelling studies yielded values around 40 mSv (with a plausible range of 20–80 mSv (Roberts et al., 2014; Ziemen et al., 2019); 1 Sv=10^6 m^3s^{-1}). For comparison, the present-day Greenland ice sheet solid discharge is estimated to be 18 mSv for the years 1958–2010 (Bamber et al., 2012).

1.2 Freshwater hosing experiments

One of the way to simulate HEs in Earth System Models (ESMs) is to treat calved ice mass as freshwater. There were number of studies aiming to understand the AMOC response to a huge amount of freshwater injection that are known as (freshwater) hosing experiments. From model studies it is well known that freshwater hosing can cause fast and rapid weakening of the AMOC and, due to the reduced North Atlantic poleward heat transport, a strong surface cooling and extended sea ice cover (Maier-Reimer and Mikolajewicz, 1989; Mikolajewicz and Maier-Reimer, 1994; Schiller et al., 1997; Ganopolski and Rahmstorf, 2001; Gregory et al., 2003; Stouffer et al., 2006; Peltier et al., 2006; Otto-Bliesner and Brady, 2010; Roche et al., 2014). The AMOC sensitivity depends strongly on the location of the freshwater input (e.g., Maier-Reimer and Mikolajewicz, 1989; Rahmstorf, 1996; Schiller et al., 1997; Smith and Gregory, 2009; Otto-Bliesner and Brady, 2010; Roche et al., 2014) as it defines the amount of freshwater that can interact with deep water formation areas. Ganopolski and Rahmstorf (2001) examined the AMOC response to freshwater hosing for different background climates and found its strong dependence on the background climate. For the pre-industrial climate, the freshwater hosing leads to abrupt AMOC switches between a strong and a weak mode, whereas for LGM climate conditions, the AMOC response to the freshwater forcing is very gradual.

In freshwater hosing experiments, there are two typical ways to prescribe the forcing: either as point source forcing (e.g., Maier-Reimer and Mikolajewicz, 1989) or as homogeneous forcing over a latitude belt (e.g., Otto-Bliesner and Brady, 2010). The direct freshwater injection approach

for simulating ice surge events neglects iceberg dynamics and thermodynamics leading to a significantly simplified interaction with the ocean. Nevertheless, it is a simple approximation easily feasible within any climate model. Motivation for the choice of such a forcing has been that the remains of melting icebergs, IRD, can be found within this area in the North Atlantic (Ruddiman, 1977). Another potential reason, not explicitly mentioned in the paper, is likely to be that a point source requires an ocean component with a free surface. Some climate models still use ocean components with a rigid lid approximation, implying the need to treat the freshwater flux as salt flux, which, for point source hosing, leads to strongly negative salinities. The latitude belt freshwater hosing has been used as forcing for model Climate Model Intercomparison Project/ Paleo Model Intercomparison Project (CMIP/ PMIP) projects. Stouffer et al. (2006) investigated the AMOC sensitivity for present-day conditions to freshwater hosing for different climate models, both for Earth Models of Intermediate Complexity (EMIC) and for General Circulation Models (GCM). In this study, all models show a qualitatively similar response to freshwater hosing homogeneously distributed between 50° and 70°N: a shallowing of NADW formation and a weakening of the AMOC strength with reduced North Atlantic heat transport, which leads to a surface cooling.

For modelling past events like HEs, one would choose an experimental design with a prescribed hosing over a certain period of time (or even a time-depending discharge). In the past, many studies have been run in such a set-up (e.g., Maier-Reimer and Mikolajewicz, 1989; Stouffer et al., 2006; Peltier et al., 2006; Otto-Bliesner and Brady, 2010; Roche et al., 2014). While this approach can work well for simulating specific events, it is not optimal for understanding of the system as it makes the comparison between different modelling studies complicated. In this approach, the response of the AMOC depends both on the amount as well as on the duration of a given perturbation. These two degrees of freedom make it difficult to compare the outcome from different studies.

Another approach is to investigate the steady-state response to a given forcing (Mikolajewicz and Maier-Reimer, 1994; Schiller et al., 1997; Rahmstorf, 1996, 2002; Gregory et al., 2003) and the resulting hysteresis curve including potentially occurring multiple steady states (Stommel, 1961). For this, the hosing is slowly increased and decreased. Such approach allows to estimate the stability behavior of the system and to identify threshold values and points in parameter space, where the effect of a given pertur-

bation is no longer reversible which can then be compared for different models.

However, to modelling HEs, icebergs are need to be added to the system in order to get an adequate spatial distribution of the meltwater input. Hereafter, meltwater is referred to as melting icebergs and freshwater as a direct freshwater injection. In contrast to direct freshwater hosing, this would also allow for a change of the meltwater input pattern in case of surface cooling due to a weakening of the AMOC as well as the effect of heat extraction from the ocean to melt icebergs. Standard coupled climate models typically do not contain interactive iceberg components, therefore, the number of studies investigating the effect of iceberg hosing is much smaller than the number of studies investigating freshwater hosing.

1.3 Iceberg modelling

In earlier studies, iceberg modules accounted either for iceberg dynamics (e.g., Mountain, 1980; Smith, 1993) or thermodynamics (e.g., El-Tahan et al., 1987). Bigg et al. (1997) included both, iceberg dynamics and thermodynamics, in the same module that is now a standard iceberg module configuration. All existing iceberg modules can be divided into two large groups according to the task they aim to solve, namely, the "Titanic" problem and the "Heinrich" problem (Clarke and La Prairie, 2001). The first, the "Titanic" problem, focuses on the prediction of iceberg trajectories (e.g., Mountain, 1980; Smith, 1993; Bigg et al., 1997; Lichey and Hellmer, 2001; Gladstone et al., 2001; Keghouche et al., 2009; Bigg and Wilton, 2014; Turnbull et al., 2015; Rackow et al., 2017; Bigg et al., 2018). The second, the "Heinrich" problem, aims at determining of locations and amount of the meltwater injection due to icebergs melt and drift and its interaction with the ocean (e.g., Death et al., 2006; Gladstone et al., 2001; Levine and Bigg, 2008; Wiersma and Jongma, 2010; Martin and Adcroft, 2010; Bigg et al., 2011; Jongma et al., 2009, 2013; Hill and Condron, 2014; Marsh et al., 2015; Bügelmayer et al., 2015; Bügelmayer-Blaschek et al., 2016; Rackow et al., 2017). Traditionally, iceberg modelling has focused on predicting iceberg distributions in order to avoid collisions with ships, or the "Titanic"-like problem. For this purpose, Lagrangian formulation works best. Therefore, all existing iceberg modules follow this line. All Lagrangian iceberg modules are also applicable for "Heinrich"-like problem but result in more complicated and computationally expensive calculations as an increase in

the number of icebergs within the module leads to an increase in the computational costs.

There are different approaches to account for icebergs in modelling studies depending on the focus of the study. An iceberg module can either operate independently or be integrated into climate models. It can be forced by a climatology or by the model output data. When integrated within the complex model, it can interact with the model or only uses its output. Thus, for a number of studies that are focused on solving the "Titanic"-like problem, iceberg modules are implemented as stand-alone models (e.g., El-Tahan et al., 1987; Smith, 1993; Bigg et al., 1997; Wagner et al., 2017), whereas in some approaches it is included into ESMs of different complexities (EMICs or GCMs) in different configurations but does not interact with it (e.g., Death et al., 2006; Keghouche et al., 2009; Rackow et al., 2017). For "Heinrich"-like problems, the module must be interactive with the ESM (e.g., Jongma et al., 2009; Martin and Adcroft, 2010; Wiersma and Jongma, 2010; Bügelmayer et al., 2015; Marsh et al., 2015). The minimum Earth system configuration in these studies consists of an ocean and a sea-ice component (Marsh et al., 2015). Most of the models, account for atmosphere and vegetation (Jongma et al., 2009; Martin and Adcroft, 2010; Wiersma and Jongma, 2010). Only one EMIC, iLOVECLIM, is coupled with interactive ice sheets (Bügelmayer et al., 2015). The typical interaction between icebergs and the ocean is implemented as a 2D-feedback, meaning that meltwater and latent heat fluxes associated with iceberg melt are applied to the ocean surface layer. The more comprehensive iceberg-ocean interaction is a 3D-feedback, where salinity and temperature changes due to iceberg melt are applied to the adequate ocean layer. Such an interaction is only implemented in the EMIC iLOVECLIM (e.g., Wiersma and Jongma, 2010; Jongma et al., 2013; Bügelmayer et al., 2015).

Several studies aimed at understanding the effect of including icebergs for past climate events, or solving "Heinrich"-like problems, and compare this response with the response from the system that is forced by a direct freshwater injection (Levine and Bigg, 2008; Wiersma and Jongma, 2010; Bigg et al., 2011; Jongma et al., 2013). Typical for these studies is that models were forced by constant forcing. The length of the simulations was no longer than 1,000 years and, most importantly, all these simulations were performed with Lagrangian iceberg modules coupled to different EMICs. All these experiments showed that the AMOC sensitivity strongly depends on the type of hosing, namely, icebergs or a direct freshwater

input. In order to run these simulations within reasonable computational costs, some modification of Lagrangian iceberg modules were necessary.

Thus, Levine and Bigg (2008) ran an EMIC coupled to the Lagrangian iceberg module to simulate a "Heinrich"-like event. In this set-up, icebergs were released from multiple locations four times a year in order to account for the seasonality and to reduce the number of icebergs in the module. The released calving flux was distributed within ten different iceberg classes and several release locations. Numbers of icebergs in every class were scaled according to the total released volume of ice and their fractional distribution (Table 1, Bigg et al., 1997). Therefore, every single iceberg represents a group of icebergs. This approach results in 5,000–7,000 active icebergs in the module which leading to an up to two times increase in the number of computations per ocean time step. Millennial simulations in such a set-up are possible, but if icebergs were released in ten classes at every ocean time step, the total number of icebergs in the module would increase by a factor of 300. Such computation would not be possible with reasonable computational costs. Therefore, for further studies, improvements to Lagrangian iceberg modules are required to make it possible to release as many icebergs as needed and to run such a set-up within GCMs (here Max Planck Institute Earth System Model MPI-ESM) to simulate past climate events over a long time period like, e.g. the last deglaciation.

Considering the role of icebergs for climate studies, or solving "Heinrich"-like problems, the key aspect is iceberg melt with the release of meltwater and consumption of heat. For climate purposes, the focus lies rather on the integrated effect of all icebergs and not on the fate of individual icebergs. Therefore, the most natural way to formulate an iceberg module for climate studies is using an Eulerian framework. This strongly simplifies the implementation into existing Eulerian ocean models and allows the easy use of existing infrastructure for efficient parallelization and data input/output.

1.4 Objectives of thesis

To study a response of AMOC to hosing as icebergs, a new iceberg module needs to be designed. For this, a new iceberg module formulated in the Eulerian framework is introduced and is implemented into MPI-ESM. This new module is used to study the near equilibrium response of the AMOC to iceberg hosing for different climate conditions. The results are compared to

the results from freshwater hosing at a point source off the Hudson Strait and freshwater hosing distributed equally over the Atlantic at a latitude belt 50° to 70°N. So far, a similar approximation of a hysteresis curve with a slowly increasing and decreasing input for iceberg hosing has not been done before. The new Eulerian iceberg module is applied for long-term simulations and its application in a coupled climate simulations aiming to understand the effect of including icebergs in simulations of ice surge events and answer following questions:

RQ 1 **How does the climate system response differ to hosing as icebergs rather than as a direct freshwater input?**

RQ 2 **What is the effect of the background climate on the iceberg meltwater flux? How does the background climate affect the climate system response to different type of hosing?**

RQ 3 **Can the iceberg module reproduce a plausible iceberg meltwater flux over glacial simulations?**

2 Model description and validation

2.1 Max Planck Institute Earth System Model (MPI-ESM)

I use the Max Planck Institute Earth System Model (MPI-ESM, Mauritsen et al., 2019). MPI-ESM consists of the atmospheric component ECHAM6 (Stevens et al., 2013) with the land subcomponent JSBACH (Reick et al., 2013) being a part of ECHAM6, and the ocean component MPI-OM (Jungclaus et al., 2013). The atmosphere and the ocean are coupled via the Ocean Atmosphere Sea Ice Soil coupler OASIS3 (Valcke, 2013).

ECHAM6 is a primitive-equations atmospheric general circulation model on mixed finite-difference/ spectral discretization. The spectral horizontal resolution in a coarse resolution set-up corresponds to the triangular truncation at wave number 31 (T31, $3.75° \times 3.75°$ resolution in the grid point space). The vertical discretization is implemented on a 31 hybrid σ-pressure layers (L31) reaching up to 100 hPa of the atmosphere (Stevens et al., 2013). A natural land cover change model JSBACH is a part of ECHAM6 and runs on the same grid (Reick et al., 2013; Schneck et al., 2013). The natural land cover change is implemented as "plant functional type" where each grid cell is split into several "tiles" corresponding to different dynamically changeable vegetation type. The water budget over the land is closed by the river runoff module HD (Hagemann and Dümenil, 1997).

MPI-OM is a primitive-equation ocean general circulation model on z-coordinate system (Marsland et al., 2003; Jungclaus et al., 2006, 2013). The spatial discretization is implemented on a bi- or three- polar curvilinear Arakawa C-grid (Arakawa and Lamb, 1977). To design and test iceberg module, I use the stand-alone ocean model MPI-OM at different resolutions. The coarse resolution (CR) set-up of the model has a formal resolution of $3°$ (GR30), the low-resolution of $1.5°$ (GR15). For these configurations, grid poles are located over the Greenland and Antarctica. This allows having higher resolution in areas where deep water formation occurs. A high-resolution configuration is $0.4° \times 0.4°$ (TP04) and is implemented on the three-polar grid with poles located over the North America, Siberia, and Antarctica that allows better resolving of the AABW. In all set-ups, the ocean has 40 unevenly distributed vertical levels (L40) with the thinnest of

15 m for the surface and the thickest of 600 m for the bottom layer, correspondingly, with nine levels to describe the first 100 m of the ocean. Sea ice dynamics and thermodynamics are formulated within the MPI-OM model and is based on viscous-plastic Hibler rheology (Hibler, 1979; Marsland et al., 2003).

The atmosphere and the ocean models are coupled using OASIS3 coupler (Valcke, 2013). The coupling is implemented by fluxes exchange between ECHAM6 to MPI-OM and MPI-OM to ECHAM6 once per day. SST, sea ice thickness and concentrations, snow thickness, and ocean surface velocity are transferred from MPI-OM to ECHAM6. Stress components over the ocean and sea ice, rainfall and snowfall, heat fluxes over the ocean and ice, heat flux residual, short wave radiation and wind speed are transferred from ECHAM6 to MPI-OM.

The set-up of the coarse resolution MPI-ESM-CR has been generated with an automated procedure based on the algorithms for ocean bathymetry generation by Meccia and Mikolajewicz (2018). The river direction file has been generated as described in Riddick et al. (2018).

2.2 Eulerian iceberg module

In the Lagrangian approach (e.g., Bigg et al., 1997; Martin and Adcroft, 2010), individual groups of icebergs are considered and tracked with typical state variables such as iceberg dimension (length, width and height), position (latitude and longitude) and velocities. Whereas in the Lagrangian framework a continuous distribution of iceberg sizes is modeled, in the Eulerian framework a limited number of iceberg size classes need to be introduced. In the Eulerian framework, instead of individual icebergs, iceberg concentrations are main state vectors. Therefore, the transition from the Lagrangian to the Eulerian space results in changes in prognostic variables in the iceberg module. Thus, likewise the Lagrangian approach, in the Eulerian formulation, iceberg velocities are tracked. Changes in iceberg size now result in a transition between iceberg size classes with matching changes in concentration. In the Eulerian approach, prognostic variables are iceberg concentration, as well as iceberg velocities for every iceberg size class on each grid point.

For simplicity, here is used a 1D size class distribution with iceberg volume as the only variable. For each volume class, fixed values of length, width and height are defined. In principle, the model could easily be ex-

tended into 2D (area and depth) or 3D (length, width, and depth) iceberg size classes distribution. However, the computational cost would increase substantially. As an additional assumption, it is supposed that the icebergs do not interact with each other, which is also frequently assumed in Lagrangian iceberg modules.

In the Eulerian iceberg module, it is assumed that in every single ocean grid point exists N iceberg size classes with a known mass $m(n)$ ($n = \overline{1;N}$). Icebergs move with velocities $\vec{v}(n)$ and their concentration in every ocean grid point is $C(n)$. Change in concentration of icebergs of each size class are due to the horizontal advection of iceberg concentrations, the transfer of icebergs from one size class (n) to the adjacent class ($n \pm 1$) (the model's representation of iceberg melt and growth), as well as the generation of new icebergs due to the ice sheet calving $V_{source}(n)$. Iceberg velocities and mass loss calculations are done using the same set of parameterizations as in the Lagrangian formulation. These parameterizations are based on the oceanic and the atmospheric state on every time step. Iceberg mass loss $V_{melt}(n)$ is calculated after the iceberg velocity as melting depends not only on the ocean and atmosphere state but also on the earlier determined iceberg velocities. Total mass loss is expressed by transferring a part of the bigger icebergs size class $C(n)$ to the next smaller iceberg size class $C(n-1)$, keeping the total number of icebergs constant. Only discharge from calving locations is allowed to increase the total number of icebergs. Only melt in the smallest iceberg size class is allowed to result in a decrease in the total number of icebergs. Therefore, the evolution of iceberg concentration for every iceberg size class is:

$$\frac{\partial C(n)}{\partial t} + \vec{\nabla}\big(\vec{v}(n)C(n)\big) = -\frac{V_{melt}(n)}{V(n) - V(n-1)} + \frac{V_{melt}(n+1)}{V(n+1) - V(n)} + \frac{V_{source}(n)}{V(n)} \tag{1}$$

where n - is an iceberg size class ($n = \overline{1;N}$), N - is the total number of iceberg size classes in the module, $C(n)$ - is the iceberg concentration of size class n, $V(n)$ - is the volume of an individual iceberg of size class n, $V_{melt}(n)$ - is the melted volume of an iceberg of size class n, $V_{source}(n)$ - is the iceberg volume of a size class n added due to ice sheet calving.

As mentioned before, parameterizations of calculation of the drift and the melt components are the same as in the Lagrangian framework. Key components, which describe an iceberg lifetime after the calving from the

ice sheet, are based on study of Bigg et al. (1997) and simplifications by Martin and Adcroft (2010). Thus, for every iceberg of a size class n, changes in size fit to:

$$\rho_{ice}\frac{d\big(L(n)W(n)H(n)\big)}{dt} = \\ = \rho_{ice}\Big(- L(n)W(n)M_{bas}(n) - H(n)\big(L(n)+W(n)\big)\big(M_{we}(n)+M_{bc}(n)\big)\Big) \tag{2}$$

where ρ_{ice} - is the ice density, $L(n)$, $W(n)$ and $H(n)$ - are the length, the width and the height of an iceberg of a size class n, $M_{bas}(n)$ - is the basal melt, $M_{we}(n)$ and $M_{bc}(n)$ - are mass loss due to the wave erosion and the buoyant convection of an iceberg of a size class n, respectively.

The basic drift equation for every iceberg size class n is that suggested by Bigg et al. (1997) and widely used in other studies (e.g., Gladstone et al., 2001; Martin and Adcroft, 2010; Jongma et al., 2013). Here the advection of momentum is neglected:

$$m(n)\frac{\partial \vec{v}_{dr}(n)}{\partial t} = \vec{F}_a(n) + \vec{F}_w(n) + \vec{F}_{si}(n) + \vec{F}_r(n) + \vec{F}_p(n) + \vec{F}_{cor}(n) \tag{3}$$

where $\vec{F}_a(n)$ - is the air drag, $\vec{F}_w(n)$ - is the water drag, $\vec{F}_{si}(n)$ - is the sea ice drag, $\vec{F}_r(n)$ - is the wave radiation force, $\vec{F}_p(n)$ - is the pressure gradient, and $\vec{F}_{cor}(n)$ - is the Coriolis force of an iceberg of a size class n.

Below, the iceberg size class index n is omitted for simplicity.

2.2.1 Iceberg dynamics

Changes in the drift velocity $\vec{v}$ of an iceberg of a mass m for every iceberg size class n are driven by the wind, sea ice, ocean currents, waves and the sea slope (Eq. 3).

1. Air drag $\vec{F}_a$. The subaerial part of the iceberg (sail) is pushed by the wind. The drag is proportional to the square of the iceberg-air relative velocity as in Bigg et al. (1997) with the modification by Martin and Adcroft (2010):

$$\vec{F}_a = \rho_a\Big(0.5\ c_{a,v}WH_s + c_{a,h}LW\Big)\,|\vec{v}_a - \vec{v}|\,\Big(\vec{v}_a - \vec{v}\Big) \tag{4}$$

   Here ρ_a - is the density of air, W and L - are the iceberg width and

length, H_s - is the sail height, $c_{a,v}$ and $c_{a,h}$ - are the vertical and horizontal air drag coefficients, $\vec{v}_a$ - is the air velocity.

2. Water drag $\vec{F}_w$. The submerged iceberg part (keel) is affected by ocean currents (Martin and Adcroft, 2010) and is calculated separately for each of the ocean model layer (Smith, 1993):

$$\vec{F}_w = \rho_w \sum_{k=1}^{k_{bot}} \Big(0.5\ c_{w,v} W H(k) + c_{w,h} L W\Big) \left|\vec{v}_w(k) - \vec{v}\right| \Big(\vec{v}_w(k) - \vec{v}\Big) - \\ -\rho_w 0.5\ c_{w,v} W H_{si} \left|\vec{v}_{sf} - \vec{v}\right| \Big(\vec{v}_{sf} - \vec{v}\Big) \tag{5}$$

Here ρ_w - is the water density, k - is the ocean layer index ($k = \overline{1; k_{bot}}$), k_{bot} - is the ocean layer index corresponding to the bottom of the iceberg, W and L - are the iceberg width and length, $H(k)$ - the height of the iceberg in the ocean layer k, H_{si} - is the sea ice thickness, $c_{w,v}$ and $c_{w,h}$ - are the vertical and horizontal water drag coefficients, $\vec{v}_w$ - is the ocean velocity of the ocean layer k ($k = k_{sf}$ is the surface ocean velocity).

3. Sea ice drag $\vec{F}_{si}$. The top of submerged part of an iceberg can also be pushed by sea ice. The classical approach (Bigg et al., 1997) is modified to account for the concentration of sea ice:

$$\vec{F}_{si} = 0.5\ A_{si}\ \rho_{ice} c_{si,v} W H_{si} \left|\vec{v}_{si} - \vec{v}\right| \Big(\vec{v}_{si} - \vec{v}\Big) \tag{6}$$

Here ρ_{si} - is the sea ice density, A_{si} - is the sea ice concentration, W - is the iceberg width, H_{si} - is the sea ice thickness, $c_{si,v}$ - is the vertical sea ice drag coefficients, $\vec{v}_{si}$ - is the sea ice velocity.

4. Wave radiation force $\vec{F}_r$. Each iceberg is also affected by incident waves which push it in addition to the air drag force. The parameterization is as in Martin and Adcroft (2010):

$$\vec{F}_r = 0.5\ \rho_w c_r a \vec{g}\ \min(a, H_s) \frac{2LW}{L+W} \frac{\vec{v}_a}{|\vec{v}_a|} \tag{7}$$

where ρ_w - is the water density, $\vec{g}$ - is the Earth gravity, H_s - is the sail height, W and L - are the iceberg width and length, $\vec{v}_a$ - is the air velocity, a - is the wave amplitude $a = 0.010125 \left|\vec{v}_a - \vec{v}\right|^2$ and the wave radiation coefficient

$$c_r = 0.06 \min\Big(\max[0, \frac{L - L_c}{L_f - L_c}], 1\Big) \tag{8}$$

where the cutoff length $L_c = 0.125 L_w$ and the upper limit $L_t = 0.25 L_w$ with a wave length $L_w = 0.32 \ |\vec{v}_a - \vec{v}|^2$.

5. Pressure gradient $\vec{F}_p$. The pressure gradient is a basic force that influences on any object in the water due to difference in the sea level height:

$$\vec{F}_p = -m\vec{g} \ \vec{\nabla}\zeta \tag{9}$$

where $\vec{g}$ - is the Earth gravity, ζ - is the sea surface elevation.

6. Coriolis force $\vec{F}_{cor}$. The Coriolis force affects the iceberg due to Earth rotation. Thus, in the Northern Hemisphere, any moving object tends to decline to the right:

$$\vec{F}_{cor} = -m\vec{f} \times \vec{v} \tag{10}$$

where f - is the Coriolis parameter,

$$f = 2 \ \Omega \ sin(\phi) \tag{11}$$

and Ω - is the Earth rate of rotation and ϕ is the latitude in radians.

The solution of eq.3 is the drift velocity $\vec{v}_{dr}$. The final iceberg velocity $\vec{v}$ depends on the concentration and thickness of sea ice in the grid cell. If the sea ice concentration is not too high ($A_{si} \leq 90\%$), the iceberg velocity is exactly the drift velocity as in eq.3. If the sea ice concentration and strength are high enough, the iceberg is blocked by sea ice and moves with its velocity ($A_{si} \geq 90\%$ and $P \geq P^*$; Keghouche et al., 2009; Hunke and Comeau, 2011). Here, a smoother transition between the two regimes is implemented. This is done by applying a linear combination dependent on sea ice strength between calculated iceberg drift velocity and iceberg velocity equal to the sea ice velocity when sea ice concentration is high ($A_{si} \geq 90\%$):

$$\vec{v} = \begin{cases} \vec{v}_{dr}, & A_{si} \leq 90\% \\ \dfrac{P \ \vec{v}_{dr} + P^* \ \vec{v}_{si}}{P + P^*}, & A_{si} > 90\% \\ \vec{v}_{si}, & A_{si} > 90\% \text{ and } P \geq P^* \end{cases} \tag{12}$$

where P - is the measure of resistance of sea ice:

$$P = P^* H_{si} \exp(-20\ \big(1 - A_{si}\big)). \tag{13}$$

and P^* - is the sea ice strength threshold value (Hibler, 1979). Threshold values are derived from observations (Keghouche et al., 2009).

2.2.2 Iceberg thermodynamics

The melted iceberg volume per time step for every iceberg size class n ($n = \overline{1;N}$) is a matter of mass loss due to the wave erosion, the bottom melt, and the buoyant convection (Eq. 2):

$$V_{melt} = \Big(LW M_{bas} + H\big(L + W\big)\big(M_{we} + M_{bc}\big)\Big)dt \tag{14}$$

where W, L and H - are the iceberg width, length and height, M_{bas} - the basal melt rate, M_{we} - the wave erosion melt rate, M_{bc} - the buoyant convection melt rate, dt - time step.

1. Wave erosion M_{we}. The mass loss due to wave absorption on iceberg walls at the water level is a function of sea state, sea ice coverage and the SST (Martin and Adcroft, 2010). This parameterization is modified to directly include ocean freezing temperature:

$$M_{we} = \frac{1}{12} S_s \Big(1 + cos(\pi A_{si}^3)\Big)\Big(T_{sf} - T_{freeze}\Big) \tag{15}$$

   where T_{sf} - is the SST, T_{freeze} - is the ocean freezing temperature ($-1.9°C$), A_{si} - is the sea ice concentration, S_s is the sea state function calculated in accordance with Beaufort scale (Martin and Adcroft, 2010):

$$S_s = \frac{3}{2} \left|\vec{v}_a - \vec{v}_w(k_{sf})\right|^{0.5} + \frac{1}{10} \left|\vec{v}_a - \vec{v}_w(k_{sf})\right| \tag{16}$$

   Here $\vec{v}_a$ and $\vec{v}_w$ - are air and water velocities, respectively; k_{sf} - the index of the surface ocean layer. The wave erosion component also accounts for the calving of the overhanging slab.

2. Basal melt M_{bas}. The basal melt is driven by the turbulent flow on the base of the iceberg and is a function of the velocity difference between ocean and iceberg and the temperature difference (Bigg et al., 1997):

$$M_{bas} = 0.58 \left|\vec{v} - \vec{v}_w(k_{bot})\right|^{0.8} \frac{T_w(k_{bot}) - T_{ib}}{L^{0.2}} \tag{17}$$

where $\vec{v}_w$ - is the water velocity, k_{bot} - the ocean layer index corresponding to the iceberg bottom, T_w - is the temperature of the corresponding ocean layer, T_{ib} - is the iceberg temperature ($-4.0°C$), L - is the iceberg length. The basal melt for the grounded iceberg is set up to zero.

3. Buoyant convection M_{bc}. The buoyant convection is the melt along the keel walls of the iceberg that is driven by the temperature difference between the iceberg and the ocean (El-Tahan et al., 1987). The buoyant convection is calculated independently for every ocean layer:

$$M_{bc} = \sum_{k=1}^{k_{bot}} \left(7.62 \times 10^{-3} T_w(k) + 1.29 \times 10^{-3} T_w(k)^2\right) \frac{H(k)}{H_k} \qquad (18)$$

Here T_w - is the ocean temperature of the layer k, k - is the ocean layers index ($k = \overline{1; k_{bot}}$), k_{bot} - is the ocean layer index corresponding to the iceberg bottom, $H(k)$ - the height of the iceberg in the ocean layer k, H_k - the iceberg keel height.

2.2.3 Coupling with the MPI-ESM

The coupling between MPI-ESM and the Eulerian iceberg module is implemented by exchanging fluxes between the iceberg module and MPI-ESM on every ocean time step. From the ocean model, the Eulerian iceberg module requires ocean temperature, salinity and velocity; sea ice concentration, thickness and velocity; and sea surface elevation. From the atmosphere, the module requires a 2-m air temperature, wind speed, and wind stresses. Icebergs change only ocean physical properties and do not affect the ocean dynamics. Thus, the momentum transfer to the ocean through icebergs is neglected. So the feedback from icebergs on the ocean is restricted to mass (meltwater) and heat. These feedbacks are implemented in a 3D way, injecting the amount of meltwater into and extracting the latent heat required to melt iceberg from the respective ocean model layer. Here, icebergs do not affect the atmosphere directly.

The ocean model set-ups used here are rather coarse resolution. Therefore, narrow fjords and their sill depths are not well represented. Releasing icebergs in these fjords (as it happens in quite some outlet glaciers) will lead to artificial accumulation of icebergs there due to the too shallow rep-

resentation of sills. One way to avoid this problem would be to introduce icebergs only at the shelf edge and to transfer the iceberg sources further into the ocean. Another approach that is assumed here is that grounded icebergs cannot move. For high resolution set-ups, the grounding problem does not occur and the artificial assumption is not necessary.

It is also assumed that icebergs do not interact with each other, that there is no limitation on the iceberg concentration in a grid box, and that the number of icebergs per grid point can be fractional.

2.2.4 Module framework and time integration

The Eulerian iceberg module is a part of MPI-OM infrastructure and is implemented on the Arakawa-A grid (Arakawa and Lamb, 1977). It is forced by atmospheric and ocean fields from MPI-ESM, therefore vector atmospheric and ocean forcing for the iceberg module are linearly interpolated from the MPI-ESM Arakawa-C to the Eulerian iceberg module Arakawa-A grid on every time step. Iceberg drift velocities are integrated on the Arakawa-A grid by the implicit Euler scheme (as in Savage, 2001) with the MPI-OM time step. Iceberg mass loss and concentration advection are also integrated on the Arakawa-A grid but by the explicit Euler scheme with the MPI-OM time step. The melt is calculated after the velocity calculation and before the iceberg concentration advection.

2.3 Eulerian iceberg module assumptions and module validation

2.3.1 Eulerian iceberg module assumptions: general module assumptions

The majority of icebergs in the Northern Hemisphere originates from the Greenland ice sheet, can have any different shape, and often contain impurities like stones. Icebergs in the Southern Hemisphere have different origins, namely, ice shelves. They almost do not contain any pollutants, have tabular shape, and can be very large (Diemand, 2001). For the simplicity, here it is assumed that calving icebergs have the same size distribution in both hemispheres. However, this could easily be modified allowing different size distribution for different ice shelves/outlet glaciers.

2.3.2 Eulerian iceberg module assumptions: iceberg size classes parameterization

To produce a realistic simulation of iceberg meltwater distribution, it is necessary to choose the appropriate way to seed the ocean with icebergs and specify iceberg sizes. Patterns of at least two last Heinrich layers in cores indicate that iceberg drift trajectories and sizes were very similar (Dowdeswell et al., 1995). Therefore, it is assumed that iceberg sizes do not depend on the background climate and the same distribution will be used in all studies which include icebergs. The iceberg size distribution is based on studies on iceberg sizes distribution for present-day from observational data (e.g., Weeks and Mellor, 1978; Dowdeswell and Forsberg, 1992) and summarized by Bigg et al. (1997). These studies showed that the distribution follows a log-normal function of length. Bigg et al. (1997) and the following studies used this assumption in the Lagrangian iceberg module. Bigg et al. (1997) included ten different iceberg size classes excluding huge icebergs from consideration (bigger than 1,000 m in a length; Table 1 in Bigg et al., 1997). A typical iceberg in the module has a tabular shape where the length to width ratio is nearly $L : W = 1.5 : 1$. The relation for keel height is more complicated as it also depends on the glacier/ ice shelf thickness from where the iceberg originates. Thus, for small icebergs up to 300 m widths, the keel height can be calculated from the sail height using the ratio between ocean and ice densities; here it is assumed to be the same as iceberg width. For bigger icebergs, like e.g. in Antarctica where many big icebergs are calved from ice shelves, the keel height is defined as an ice shelf thickness and normally does not exceed 300–400 m. Therefore, a number of big icebergs have the same keel height. It should be noted that iceberg sizes can be slightly different (e.g., Martin and Adcroft, 2010). Thus, the maximal iceberg width included in the Bigg et al. (1997) Lagrangian iceberg module for simulation of Northern Hemisphere icebergs was 1,000 m. This value reaches nearly 1,500 m in several studies of Antarctica icebergs (e.g., Martin and Adcroft, 2010). Exclusion of bigger icebergs can be explained by the fact that their calving is a much more rare event when compared with the calving of relatively small icebergs. At the same time, the release of huge icebergs mostly happens in the Southern Hemisphere. Accounting for huge icebergs also requires some iceberg module modification that should include, e.g. calving of small icebergs from a huge one that is not covered in these studies.

In Lagrangian iceberg modules, the ocean layer where subsurface ice-

berg meltwater is injected gradually changes during the iceberg lifetime. In the Eulerian framework, if the iceberg size classes distribution is kept as in the classical input function (Bigg et al., 1997), the meltwater for several iceberg size classes will be injected to the same ocean level that will lead to less realistic ocean changes. Therefore, this standard way to seed the ocean with icebergs is needed to be modified (Table 1 in Bigg et al., 1997). Such a module modification should allow uniformly inject iceberg meltwater between the ocean surface layer and the layer corresponding to the bottom of the biggest iceberg.

For the new iceberg size class discretization applicable for the Eulerian framework, it is assumed that icebergs are tabular and iceberg volumes are the function of only one dimension, namely, the iceberg width. A length to width ratio is kept as it is in the Lagrangian approach, $L : W = 1.5 : 1$. The parameterization of iceberg height can be defined differently and needs a special discussion (chapter 2.3.3). Therefore, for new iceberg size classes, the new total number of size classes N, the minimal width of the smallest iceberg class W_{min} and the maximal height of the biggest iceberg size class H_{max} are required. Such an approach allows easily changing the size of the biggest and the smallest iceberg size classes. The parameterization of iceberg dimensions includes the assumption of a non-rolling (Bigg et al., 1997). The volume of the biggest iceberg size class is defined to be the same as the volume of the biggest size class in the input function (Table 1 in Bigg et al., 1997). To make it possible to account for small icebergs or "bergy bits", the volume of the smallest iceberg size class is different from the volume of the smallest iceberg in the input function. It is prescribed as a function of minimal iceberg width W_{min} (1.5 correspond to the ratio $L : W = 1.5$ and 1.2 follows from observations):

$$V_{max} = V_{max\_observed} \tag{19}$$

$$V_{min} = 1.5 \times 1.2 \times W_{min}^3 \tag{20}$$

Iceberg volumes are equidistantly distributed from the smallest to the biggest iceberg size classes (n is the iceberg size class, $n = \overline{1; N}$):

$$\frac{V(n)}{V(n-1)} = \left(\frac{V_{max}}{V_{min}}\right)^{\left(\frac{1}{n-1}\right)} \tag{21}$$

New fractions for every new iceberg size class are linearly interpolated from the iceberg size class fractions from input function taking into account old and new iceberg volumes.

Below, the model sensitivity to the parameterization of iceberg height and sensitivity to the total number of iceberg size classes in the module are studied (chapters 2.3.3, 2.3.4).

2.3.3 Eulerian iceberg module validation: sensitivity to the iceberg height parameterizations

As in the Eulerian approach continuous size distribution is replaced by iceberg size classes with fixed dimensions, it is essential too evaluate how the choice of iceberg height affects the iceberg meltwater flux pattern. For this, I run sensitivity experiments using the non-interactive stand-alone MPI-OM-Iceberg set-up in mid-resolution (GR15) with 40 unevenly distributed layers to represent the ocean (L40). The model is forced with the observational present-day calving flux from the Greenland and Antarctic ice sheets (Bamber et al., 2012; Rignot et al., 2013) and re-analysis climatology (Röske, 2001). Here, the total number of iceberg size classes is equal to 17 ($N = 17$). Experiment continued for 20 years and the last five years is used for the analysis.

In these experiments, as described in the previous paragraph, for input iceberg size parameterization, the classical input function is used (Bigg et al., 1997). The volume of the biggest iceberg is fixed. The volume of the smallest iceberg is calculated as a function of the smallest iceberg width. A volume ratio between the two neighbor classes is assumed to be fixed. In all experiments, the iceberg length and the height are functions of the iceberg width. If the ratio between iceberg length and width is the same in all sensitivity experiments ($L(n) : W(n) = 1.5 : 1$), the parameterization of iceberg height is different.

Thus, in the first sensitivity experiment, iceberg height parameterization is the same as in the classical icebergs input function. But unlike the classical input function, iceberg size classes are modified with regard to new volume distribution assumptions and the addition of extra iceberg size classes.

In the second sensitivity experiment, iceberg height is a linear function of iceberg width:

$$H(n) = a + bW(n) \tag{22}$$

where a and b depend on iceberg dimensions.

And in the third sensitivity experiment, the iceberg height is an exponential function of the iceberg width:

$$H(n) = H_{max}\left(1 - e^{-\frac{W(n)}{H_{max}}}\right) \tag{23}$$

where H_{max} is the prescribed maximal height of iceberg. In last two experiments, the parameterization of iceberg height allows more realistically distributing iceberg meltwater between the ocean surface and the bottom of the biggest icebergs size class. This plays important role for the ocean circulation changes in a case of an interactive iceberg module.

Simulated iceberg meltwater flux spatial distribution show that the Eulerian iceberg module can produce a realistic meltwater spatial pattern as it lies within the observational iceberg extent (Fig. 2.1). Iceberg velocities are mainly determined by water drag, wave radiation force, and pressure gradient in areas free of sea ice. In sea ice covered areas, sea ice velocities also can regulate iceberg drift if the sea ice coverage area and its thickness are high enough. In some areas, the air drag contribution is as high as the water drag. The most iceberg melt happens on the ocean surface as the wave erosion component results in the highest rate of iceberg mass loss. The second important term is the basal melt that freshens the ocean layer corresponding to the bottom of icebergs. Lateral melt due to buoyant convection on iceberg sides is the least important in comparison with the latter two. The highest iceberg meltwater rate is reached close to calving sites and logarithmically decreases with a distance increase from these release locations. Icebergs that are big enough are capable of drifting further away as they need more time to be melted. The iceberg meltwater flux is more zonally declined for bigger icebergs rather than for small icebergs (not shown). The most expensive part of the module is the calculation of iceberg mass loss as it requires the largest number of computing operations to process one time step.

Here, in all three experiments (exponential, linear, and classical iceberg height parameterizations), iceberg volumes for the same iceberg size classes are the same but their sizes are different. Consequently, a difference in the representation of iceberg height results in a difference in iceberg width and length. In the parameterization based on classical iceberg input function, four biggest iceberg size classes have the same height

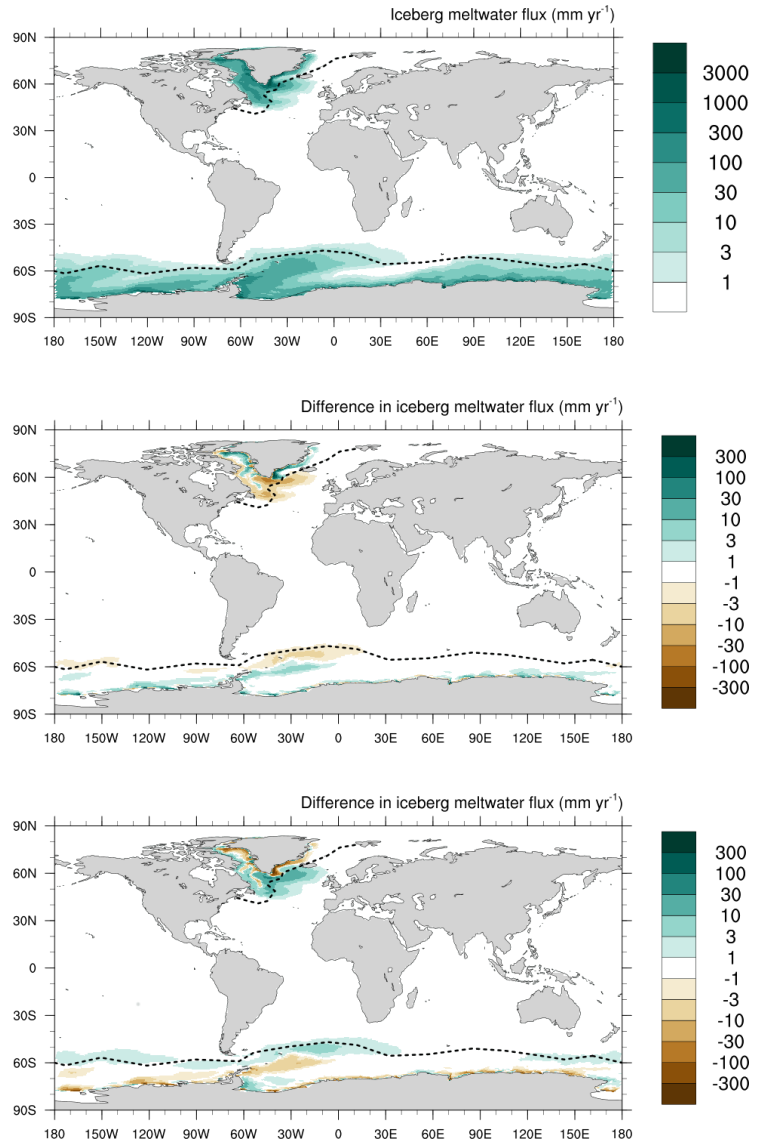

Figure 2.1: Annual mean iceberg meltwater flux (mm yr^{-1}) for exponential iceberg height parameterization with $N = 17$ (top). Total Greenland calving flux is 576 Gt yr-1 (Bamber et al., 2012). Total Antarctica calving flux is 1325 Gt yr-1 (Rignot et al., 2013). Difference in annual mean iceberg meltwater flux between the parameterization based on classical input function and exponential iceberg height parameterizations (middle); and between linear and exponential iceberg height parameterizations (bottom). Black dashed lines denote the normal iceberg extent from observations (Wagner et al., 2017; Jongma et al., 2009). Note the logarithmic scale of the colorbar.

resulting that a significant amount of iceberg meltwater flux due to basal melt is injected into the same ocean layer. In exponential and linear iceberg height parameterizations, the injection depths are gradually distributed between the ocean surface and the ocean layer corresponding to the bottom

of the biggest iceberg. Gradually distributed iceberg meltwater injection (as in linear and exponential iceberg height parameterization) implies a more realistic iceberg-ocean interaction.

The iceberg surface area in the classical iceberg height parameterization experiment is about 15% less, whereas in the linear iceberg height parameterization experiment is about 30% more than in the exponential parameterization of the iceberg height experiment. The iceberg side area is about 10% more and 12% less in classical and the linear iceberg height parameterization experiments than in the exponential, respectively. All these differences result in different iceberg velocities and consequent different iceberg melt pattern even though the volume of all iceberg size classes are the same in all parameterizations.

Thus, the iceberg meltwater flux difference between the exponential and the linear iceberg height parameterizations, and the exponential and the classical iceberg height parameterizations is less than 100 mm yr^{-1} in most locations, exceeding this value in some areas close to calving sites in the Northern Hemisphere (Fig. 2.1). As the most important melt component is the wave erosion that is applied on iceberg sides on the ocean surface, the total melting rate is higher in the classical iceberg height parameterization experiment close to calving locations and smaller in remote areas when compared to the exponential iceberg height parameterization (Fig. 2.1). The iceberg meltwater flux difference between linear and exponential iceberg height parameterization shows the opposite effect. The melt rate is less intense at calving sites and more intense in remote areas (Fig. 2.1). Consequently, the melt rate in exponential iceberg height parameterization is in between classical and linear iceberg height parameterizations experiments. Therefore, accounting also for the fact that in the exponential experiment, the meltwater is gradually distributed from the ocean surface to the ocean depth corresponding to the bottom of the biggest iceberg, this parameterization is a reasonable choice for the representation of the iceberg height.

2.3.4 Eulerian iceberg module validation: sensitivity to the number of iceberg size classes

In the Eulerian approach, iceberg size classes and corresponding to every iceberg size class iceberg concentration are defined per grid point. Therefore, an increase in the number of iceberg size classes leads to an increase

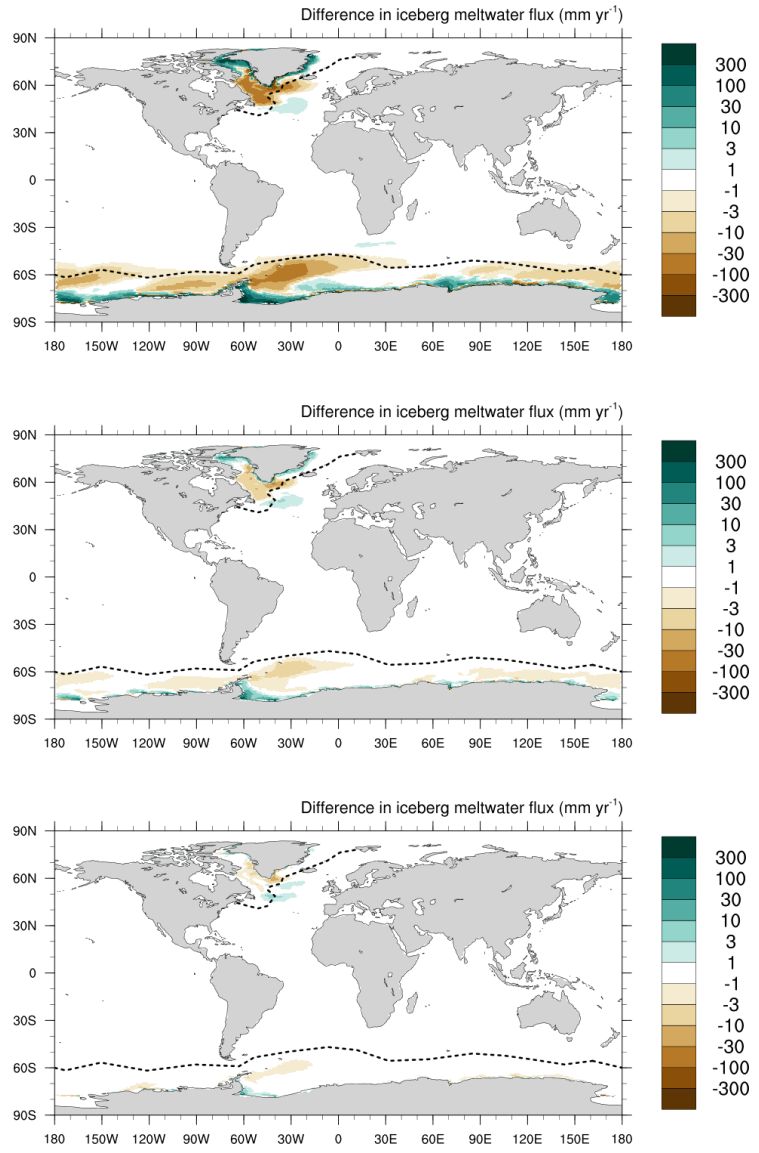

Figure 2.2: Difference in annual mean iceberg meltwater flux (mm yr^{-1}) between $N = 2$ and $N = 17$ (top); $N = 5$ and $N = 17$ (middle); $N = 9$ and $N = 17$ (bottom). Black dashed lines denote the normal iceberg extent from observations (Wagner et al., 2017; Jongma et al., 2009). Note the logarithmic scale of the colorbar.

in computational time. To make it possible to reproduce a realistic meltwater spatial distribution with low computational expenses, the number of iceberg size classes needs to be reduced.

To estimate the sufficient number of iceberg size classes, I run sensitivity experiments with an exponential iceberg height parameterization in the same model configuration as before (the non-interactive stand-alone MPI-OM-Iceberg set-up (GR15L40); see chapter 2.3.3) for a different number of

Class	Length (m)	Width (m)	Keel (m)	Sail (m)	Fraction (%)
1	32.2	21.5	18.5	2.3	0.0
2	78.5	52.4	43.3	5.5	13.0
3	195.6	130.4	97.1	12.3	31.8
4	513.4	342.2	196.1	24.8	43.6
5	1,544.9	1,029.9	301.3	38.1	11.6

Table 1: Iceberg sizes in the Eulerian iceberg module with the number of size classes $N = 5$.

iceberg size classes, defined as:

$$N = 2^i + 1 \tag{24}$$

where $i = 0; 1; 2; 3; 4$ (or $N = 2; 3; 5; 9; 17$) whereby moving from i to $i + 1$ adds exactly one additional iceberg size class in between every neighbor pair in the previous parameterization. For the analysis, I use the last five years of the simulation.

Sensitivity experiments show, that the small number of iceberg size classes ($N = 2; 3$ (three is not shown)) leads to high iceberg meltwater flux close to calving locations and low in the remote areas (Fig. 2.2). Increasing the number of iceberg size classes to 17 results in lowering the iceberg meltwater flux at calving sites and increasing the flux far away from it. The difference in iceberg meltwater flux spatial patterns between 5 and 9, 9 and 17, and 5 and 17 iceberg size classes does not result in a serious changes of calculated iceberg meltwater flux. Thus, the difference for the small number of iceberg size classes $N \leq 5$ ($N = 2; 3$) and $N = 17$ can be higher than 300 mm yr^{-1} whereas the difference between $N \geq 5$ ($N = 5; 9$) and $N = 17$ iceberg size classes does not exceed 100 mm yr^{-1}.

The computational time for the Eulerian iceberg module directly depends on the number of iceberg size classes. Increasing the number of iceberg size classes from 2 to 5 leads to an increase in computational costs by a factor of 1.3, whereas an increase from 2 to 17 leads to an increase by a factor of 2.6. Accounting for the iceberg meltwater flux spatial distribution accuracy and computational costs, five iceberg size classes is a reasonable trade-off to produce a realistic iceberg meltwater flux with exponential iceberg height parameterization (Fig. 2.2). Iceberg characteristics for $N = 5$ are presented in the Table 1.

3 Hosing experiments for the pre-industrial climate

3.1 Spin-up and background climate for pre-industrial conditions

Initial conditions for the pre-industrial climate were taken from the transient simulations integrated over the last 26,000 yrs to present-day. The simulation is described in Kapsch et al. (2020). In this simulation, greenhouse gas concentrations are taken from Köhler et al. (2017), and insolation is calculated according to Berger and Loutre (1991). To account for changing glacial conditions, ice sheets were prescribed from the GLAC-1D reconstructions by Tarasov et al. (2012). Throughout the simulation, the glacier mask and associated changes in the topography, land-sea mask and rivers routing were automatically adjusted (see Riddick et al., 2018; Meccia and Mikolajewicz, 2018, for details). Starting from a transient simulation, a 4,500 year spin-up was performed with pre-industrial greenhouse gases and orbital parameters shown in Table 2 as well as constant topography, land-sea mask and ice sheets configuration corresponding to year 1840.

3.2 Experimental set-up of hosing experiments

The idealized hosing experiments, conducted for this study are summarized in Table 3. In the first set of experiments, hosing is treated as icebergs, which delays the meltwater release to the ocean leading to transportation of this meltwater away from hosing locations due to iceberg drift (as in Jongma et al., 2009, 2013). In the first iceberg experiment, hereafter referred to as IB, icebergs are fully interactive. This means, that iceberg meltwater is added to the adequate ocean depth and the heat needed for the melting is removed from the same ocean depth. In the second iceberg experiment (IBnoLH), only the meltwater spatial distribution is accounted for, without

Eccentricity	Perihelion	Obliquity	pCO_2	pN_2O	pCH_4
0.0167683	280.274048	23.460928	284.01	270.44	775.32

Table 2: Pre-industrial orbital parameters and greenhouse gas concentrations. pCO_2 is given in ppm, pN_2O and pCH_4 in ppb.

removing the latent heat from the respective ocean depth. This allows to understand the effect of the location of the meltwater injection without accounting for cooling of the ocean layers due to melting icebergs. In the second set of experiments, hosing is treated as direct freshwater injection as liquid water. In a classical freshwater point source hosing experiment (FWPS), the freshwater is treated as liquid precipitation released to the ocean surface in one location (like in, e.g. Maier-Reimer and Mikolajewicz, 1989; Schiller et al., 1997). In the freshwater North Atlantic experiment (FWNA), the freshwater is uniformly distributed in the northern North Atlantic between 50° and 70°N (like in, e.g. Stouffer et al., 2006; Otto-Bliesner and Brady, 2010; Kageyama et al., 2013). Fig. 3.1 shows the hosing locations for all experiments. To investigate the climate response from the model drift, the experiments set-up includes a pre-industrial control experiment (CTRL). It includes a diagnostic non-interactive Eulerian iceberg module that uses MPI-ESM output as forcing. In this experiment, melting icebergs do not affect the ocean. This allows studying the effect of hosing induced ocean climate changes on iceberg distribution and melting.

In all experiments, the input-freshwater-hosing-rate (hereafter referred to as input rate) increases from 0 to 0.35 Sv in the first 3,500 years of each experiment and decreases afterwards to 0 Sv within another 3,500 years. The rather slow rate of change in input freshwater by 0.1 Sv in 1,000 years results in an almost steady-state response of the climate system. This experimental design aims at determining threshold-freshwater-hosing-rates (threshold rates) for an AMOC collapse from a strong to a weak mode (and back) for different hosing types. After the input rate reaches zero, all experiments are continued for an additional 500 years until they arrive at new equilibrium states. All simulations (IB, IBnoLH, FWPS, FWNA, CTRL) start from the same spin-up with pre-industrial climate conditions in a

Experiment	Experiment description
IB	Iceberg experiment
IBnoLH	Iceberg experiment with no latent heat
FWPS	Freshwater point source experiment
FWNA	Freshwater North Atlantic experiment with hosing between 50° to 70°N
CTRL	Control experiment

Table 3: List of pre-industrial experiments.

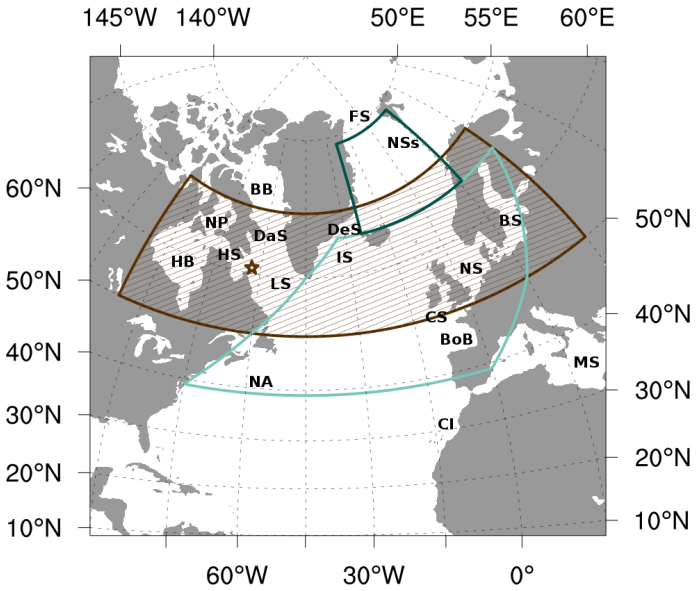

Figure 3.1: Location of hosing sites in the pre-industrial experiments: brown star denotes the location in IB, IBnoLH and FWPS; brown box in FWNA. Light green and dark green boxes denote locations of the northern North Atlantic (NA) and Nordic Seas (NSs) basins, respectively. Abbreviations are BB - Baffin Bay; BoB - Bay of Biscay; BS - Baltic Sea; CI - Canary Islands; CS - Celtic Sea; DaS - Davis Strait; DeS - Denmark Strait; HB - Hudson Bay; HS - Hudson Strait; FS - Fram Strait; IS - Irminger Sea; MS - Mediterranean Sea; LS - Labrador Sea; NP - Northwestern Passages; NS - North Sea.

coarse resolution of MPI-ESM-CR-Iceberg model (GR30L40, T31, 5 iceberg classes; see chapter 3.1) with fixed bathymetry and are continued for 7,500 years.

3.3 Results

To understand the effect of different types of hosing on the ocean circulation, I compared system responses with a slowly increasing input rate to a reference non-perturbed state (CTRL). In hosing experiments, the main interest lies in the understanding of different types of hosing effect on deep water formation in the northern North Atlantic and the Nordic Seas and corresponding AMOC changes. Therefore, SST and sea surface salinity (SSS) fields, mixed layer depth, winter, and summer sea ice extent are presented for the northern North Atlantic.

In the reference experiment CTRL (Fig. 3.2), the vast majority of deep water forms in the Nordic Seas where the maximal mixed layer depth reaches 3,400 m. A corresponding maximal ventilated volume is $2.00 \times 10^{15} \mathrm{m}^3$. The maximal mixed layer depth indicates the presence of deep

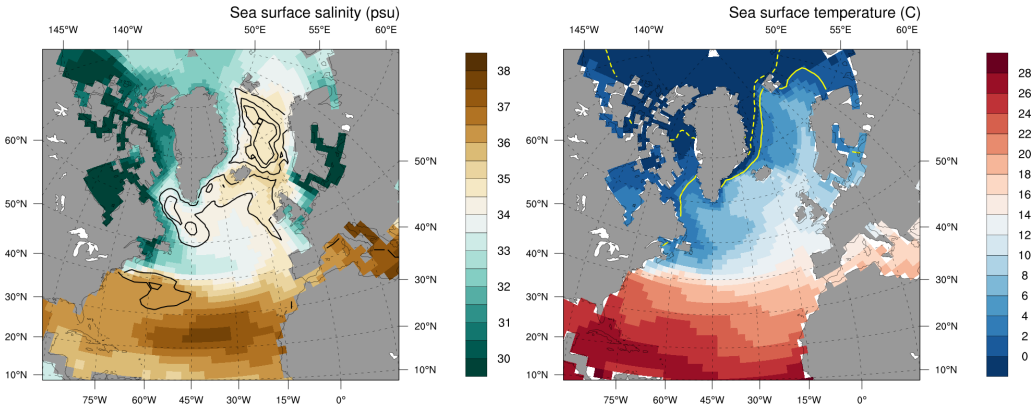

Figure 3.2: 200-years mean SSS (psu; left) overlayed by the maximal mixed layer depth (m; isolines denote values of 500 m, 1,500 m, 2,500 m, and 3,500 m); and SST (°C; right) overlayed by the sea ice extent (yellow lines; winter (solid) and summer (dashed) sea ice concentration of 15%) in CTRL.

convection. The maximal ventilated volume depicts the amount of water in the convection region that is limited by the maximal mixed layer depth. Some deep water formations also take place in the Labrador Sea, south of Greenland, and in the Irminger Sea, south-east of Greenland, with a maximal mixed layer depth of 2,000 m (Fig. 3.2, left). NADW is a mixture of the deep water formed in the Nordic Seas that outflows the Denmark Strait, where it mixes with water masses formed in the Irminger and the Labrador Seas and surrounding water masses. The AMOC strength at 26°N at 1,000 m is 16.44 Sv (Fig. 3.3), and the northward heat transport at 26°N in the Atlantic is 0.73 PW (PW=10^{15} W). In winter, sea ice covers a part of the Labrador Sea, a part of the Denmark Strait, and the Fram Strait, whereas, in summer, these areas stay ice-free with a coastal part of the Arctic being also free of sea ice (Fig. 3.2; right). Areas of deep water formation in the Nordic Seas and the Irminger Sea stay ice-free in all seasons.

3.3.1 Pre-industrial ocean response to hosing

Hosing experiments with a slowly changing input rate are aiming to determine how different will be the threshold rates when the AMOC abruptly changes from a strong to a weak mode (and back) depending on the type hosing. The system response to hosing depends on both, the input rate and the locations of fresh/ meltwater injection. If the total amount of hosing released to the ocean is defined by the input rate (Fig. 3.3), the spatial fresh/ meltwater flux and, consequently, the added amount of fresh/ melt-

water in every single location depends on the type of hosing (see chapter 3.3.2). This spatial disposition of fresh/ meltwater injection, in its turn, defines how much of the released hosing reaches areas important for the ocean circulation, e.g. the deep water formation areas. Adding the fresh/ meltwater to the surface stabilizes the water column as the water density decreases. On the other hand, the cooling destabilizes the water column as with temperature decrease, the water density increases. However, the density change per unit temperature change decreases strongly with decreasing temperature due to the nonlinearity of the equation of state. Overall, the freshening is the dominating effect and, consequently, water density decreases. Therefore, low-salinity and less dense fresh/ meltwater input into the ocean reduces the ocean's potential density. This induces a more stable stratification of the water column causing a decrease of the maximal ventilated volume (Fig. 3.3). This leads to a reduction of the convection and the AMOC collapse. The closer fresh/ meltwater release locations to areas of deep water formation, the more fresh/ meltwater is capable of reaching these areas, the smaller is the collapse-threshold-freshwater-hosing-rate (hereafter referred to as collapse rate) for the abrupt AMOC collapse.

To allow better interpretation, the AMOC strength is shown as a function of the input rate in Fig. 3.4 similarly to classical studies (e.g., Stommel, 1961; Mikolajewicz and Maier-Reimer, 1994; Rahmstorf, 1996, 2002; Gregory et al., 2003). Similarly to these works, experiments show that with a slowly increasing input rate, the AMOC strength linearly decreases until the hosing reaches the collapse rates when abrupt changes occur. With an input rate decrease, the system similarly (including abrupt changes) returns to its initial state but with a delay. This hysteresis could reveal that multiple steady states might exist.

For input rates below 0.046 Sv, the system is an almost linear function of the input rate for all experiments (Fig. 3.3, 3.4). Such a small hosing governs a nearly linear decrease of surface density and maximal ventilated volume, indicating that less deep water is formed. The linear decrease of the maximal ventilated volume in deep water formation areas results in a linear weakening of the AMOC strength from nearly 16 to 14 Sv which causes a nearly 10% decrease in the northward heat transport at 26°N in Atlantic. When less heat is accessible for the ocean, its SST in the northern North Atlantic cools down resulting in an increase of sea ice in this region (Fig. 3.3).

The system response stays an almost linear function of the input rate

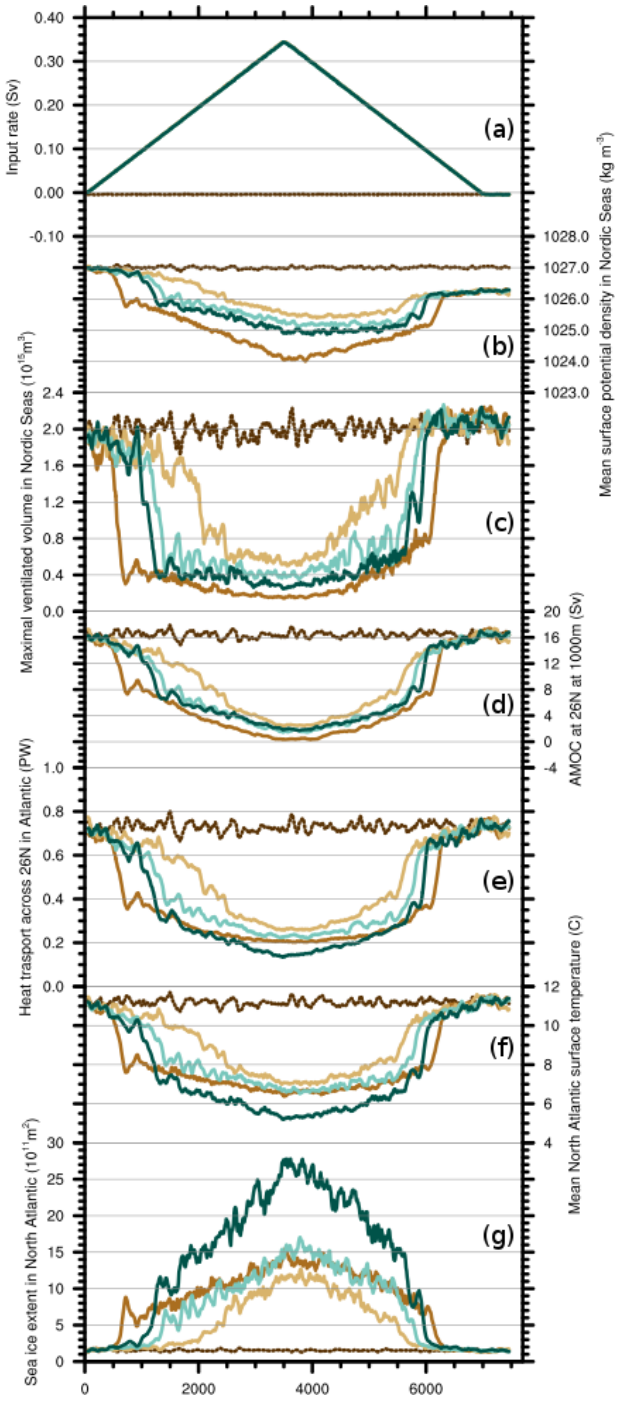

Figure 3.3: 100-years running mean of (a) input rate (Sv); (b) mean surface potential density in Nordic Seas (kg m^{-3}); (c) maximal ventilated volume in Nordic Seas (m^3); (d) AMOC at 26°N at 1,000 m (Sv); (e) heat transport across 26°N in Atlantic (PW); (f) mean SST in the northern North Atlantic (°C); (g) the sea ice extent in the northern North Atlantic (m^2). The northern North Atlantic and the Nordic Seas basins are presented in Fig. 3.1. Brown dotted line corresponds to CTRL, light brown to FWPS, medium brown to FWNA, dark green to IB, and light green to IBnoLH.

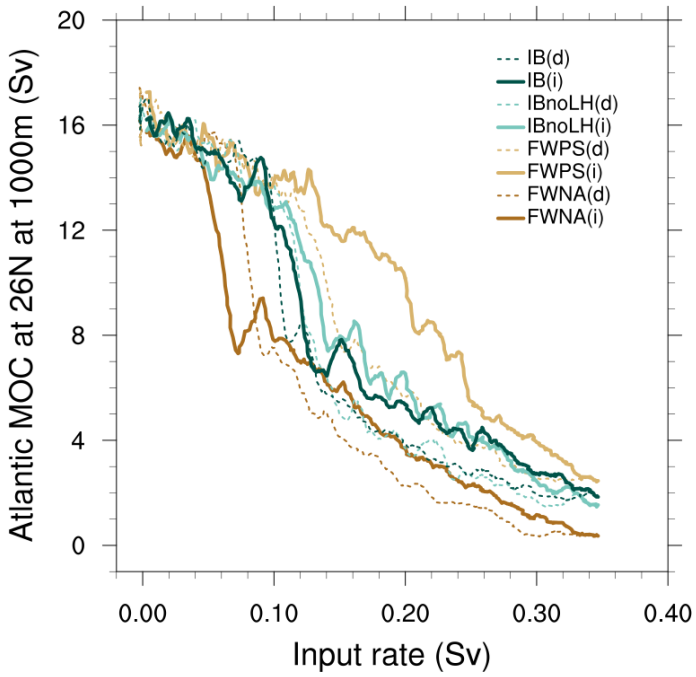

Figure 3.4: 100-years mean AMOC strength at 26°N at 1,000 m (Sv) versus input rate (Sv). Solid lines (i) depict the first part of experiments when input rate increases; dashed lines (d) correspond to the second part of experiments when input rate decreases.

until it reaches a critical value, a collapse rate. Beyond the collapse rate, deep convection in part of deep water formation sites is no longer possible, which typically is an abrupt process due to the convective instability. Depending on the type of hosing, the collapse rate is different. The collapse rates lie between 0.046–0.19 Sv (Fig. 3.3, 3.4) and are reached when the AMOC strength decreases to 11–15 Sv. In the experiment IB, where iceberg meltwater injection locations are defined by iceberg drift and melt, the abrupt convection suppression occurs at the collapse rate of 0.09 Sv and an AMOC strength of 14.5 Sv. In the experiment FWNA, where some freshwater is directly injected into deep water formation areas, the AMOC collapse occurs earlier, at a collapse rate of 0.046 Sv and an AMOC strength of 15 Sv. The largest difference in the response is evident in the experiment FWPS where the AMOC strength declines almost linear over the whole part of the experiment when the input rate increases. This is mainly due to the remoteness of the freshwater injection site from deep water formation areas. In the experiment FWPS, the AMOC collapse occurs in two stages corresponding to two stages of maximal ventilation volume decrease in the Nordic Seas (Fig. 3.3). Therefore, the collapse occurs later than in experiments IB and FWNA, at a collapse rate of 0.19 Sv and an AMOC strength

of 11 Sv. In all experiments, after the abrupt AMOC collapse, the AMOC strength lies within 6–8 Sv. After the AMOC collapse follows an overshooting of the AMOC. As the input rate still increases after the AMOC collapse, the AMOC strength keeps linearly decreasing until the input rate starts to return back to zero (Fig. 3.3, 3.4).

In all experiments, abrupt changes in the AMOC strength result in approximately 50% decrease of the Atlantic northward heat transport (from 0.73 PW to 0.37 PW), leading to an abrupt decrease of the SST and increase in sea ice in the northern North Atlantic (Fig. 3.3). Besides cooling due to the reduced northward heat transport, the melting of icebergs requires heat. The heat is extracted from the ocean resulting in an additional cooling of the upper ocean. For the peak input rate of 0.35 Sv, this effect can be as large as 2.0°C for the northern North Atlantic and leads globally to cooling of 0.3°C when compared with the experiment FWNA. The additional ocean surface cooling causes an increase in sea ice. The strongest effect is reached in the northern North Atlantic basin (Fig. 3.3). This difference is also high when compared with other hosing experiments. The experiment FWPS shows the weakest SST cooling and also the smallest increase in sea ice cover among all hosing experiments (Fig. 3.3).

The AMOC strength reaches a minimum slightly after the input rate has reached its maximum of 0.35 Sv. The delay is an artifact of the prescribed rate of change of the input rate. After the AMOC collapse, deep water formation is suppressed in all experiments. The AMOC strength increases almost linearly until the recovery-threshold-freshwater-hosing-rate (hereafter referred to as recovery rate) is reached. This typically happens at smaller input rate compared to the one for the collapse. When the input rate decreases, the water column stability decreases, allowing eventually for the occurrence of deep convection (indicated by the maximal ventilated volume in Fig. 3.3), resulting in a strengthening of the AMOC. In its turn, the strong AMOC causes an increase in the northward Atlantic heat transport and warming of the ocean surface, causing the reduction of sea ice in the northern North Atlantic (Fig. 3.3).

The AMOC recovery happens in the reverse order when compared to the AMOC collapse. Typically, it occurs when the AMOC exceeds 7.5 Sv, with the recovery rate being between 0.09–0.16 Sv. The AMOC recovery in experiment IB happens at the recovery rate of 0.14 Sv and the AMOC strength of 8 Sv. The recovery to a strong AMOC in the freshwater experiments FWPS and FWNA occurs from the same AMOC strength of 7.5

Sv but at different recovery rate, 0.16 Sv and 0.09 Sv, respectively. The AMOC strength range just after the recovery lies between 13 Sv (FWPS) and 15 Sv (FWNA), with IB experiments being in the middle (14.5 Sv). After the AMOC recovery, the system again shows a nearly linear response to the hosing as in the first phase before the AMOC collapse. At the end of experiments, the ocean circulation recovers to a state very similar to the initial state, but with a $\sim$1 psu global surface salinity freshening.

The AMOC response to hosing varies for different types of hosing but almost does not change for the collapse and recovery phase. The strongest effect is reached in the experiment FWNA where the AMOC-collapse-response-rate is -21.31 mSv indicating that in order to decrease the AMOC strength by 1 Sv, the input rate of 21.31 mSv is needed. The AMOC-recovery-response-rate is nearly 2% lower, indicating that the AMOC recovers faster than it collapses. AMOC-collapse-response-rates are -23.43 mSv and -24.43 Sv in experiments IB and FWPS, respectively. In both experiments IB and FWPS, the AMOC-recovery-response-rate is nearly 1% higher than the collapse rate resulting in a slightly delayed AMOC recovery (Fig. 3.4).

At the recovery phase, there is no stable AMOC between 8 Sv and 13 Sv, while during the collapse phase, the AMOC is unstable between 8 Sv and 11 Sv. If the experiment FWPS, where the AMOC collapse is less pronounced when compared with other experiments, is excluded from the comparison, the instability interval of the AMOC strength is nearly the same as at the recovery phase, between 8 Sv and 13 Sv. When the AMOC strength higher than 11 Sv, AMOC is in a strong mode, values lower than 8 Sv corresponds to a weak mode. Transitions between a strong and a weak AMOC modes happen as a step function due to convective instability. Hosing experiments show that there are no multiple steady-states in the considered set-up. The model tends to stay in a strong AMOC mode, and, consequently, when hosing is turned off, the AMOC strength recovers to its initial state.

To explain differences in the AMOC collapse rate in different hosing experiments, I consider a time slice before the AMOC collapse (chapter 3.3.2) corresponding to a mean input rate of 0.04 Sv. The effect of the latent heat is discussed in a separate chapter (chapter 3.3.3).

3.3.2 The AMOC sensitivity to the type of hosing

The ocean state shortly before the AMOC collapse is shown relative to the CTRL experiment in Fig. 3.5. Although the input rate is increased to 0.04 Sv, AMOC is still strong in all hosing experiments. In response to hosing, the ocean surface becomes less salty in the northern North Atlantic and the Nordic Seas (Fig. 3.5, left column) as the released fresh/ meltwater is much fresher than the surrounding ocean water. The ocean surface also becomes colder as a response to the slowing down of the circulation (Fig. 3.5, right column). The type of hosing defines the spatial distribution of the freshening pattern and its evolution as a result of different fresh/ meltwater release locations and, therefore, the amount of fresh/ meltwater that is capable of reaching deep water formation areas.

In experiment IB, the iceberg meltwater flux is heterogeneously distributed across the ocean with the highest meltwater release rate close to calving sites (Fig. 3.6). This explains high freshening rate in this region (Fig. 3.5). The iceberg drift is determined by winds and ocean currents, the iceberg meltwater distribution is determined by the ocean circulation only. Released iceberg and iceberg meltwater partly joins the subpolar gyre (SPG) and partly the subtropical gyre (STG), causing effective freshening along the north-eastern North Atlantic and the Canary Current (Fig. 3.5). Some icebergs are able to drift directly to the deep water formation areas in the Labrador and the Irminger Seas, which takes place in the center of the subpolar gyre (SPG), and melt there. At an input rate of 0.04 Sv, there are no icebergs that reach the deep water formation area in the Nordic Seas as all icebergs melt in the North Atlantic and meltwater can only be advected there with ocean currents. When compared with other hosing experiments, the iceberg meltwater flux causes relatively uniform freshening in the northern North Atlantic.

In the experiment FWPS, all freshwater is injected to the ocean immediately at the calving site and is advected by the Labrador current. This injected freshwater does not directly interact with deep water formations in the Labrador and Irminger Seas. It leaves to the open ocean with the Labrador current causing the highest freshening in the western Labrador Sea from the southern tip of Baffin Island to the Newfoundland Island (Fig. 3.5). After leaving to the open ocean, part of the released freshwater joins the STG. The amount of this freshwater is higher than in the experiment IB, therefore, the amount of freshwater that is advected to SPG is smaller

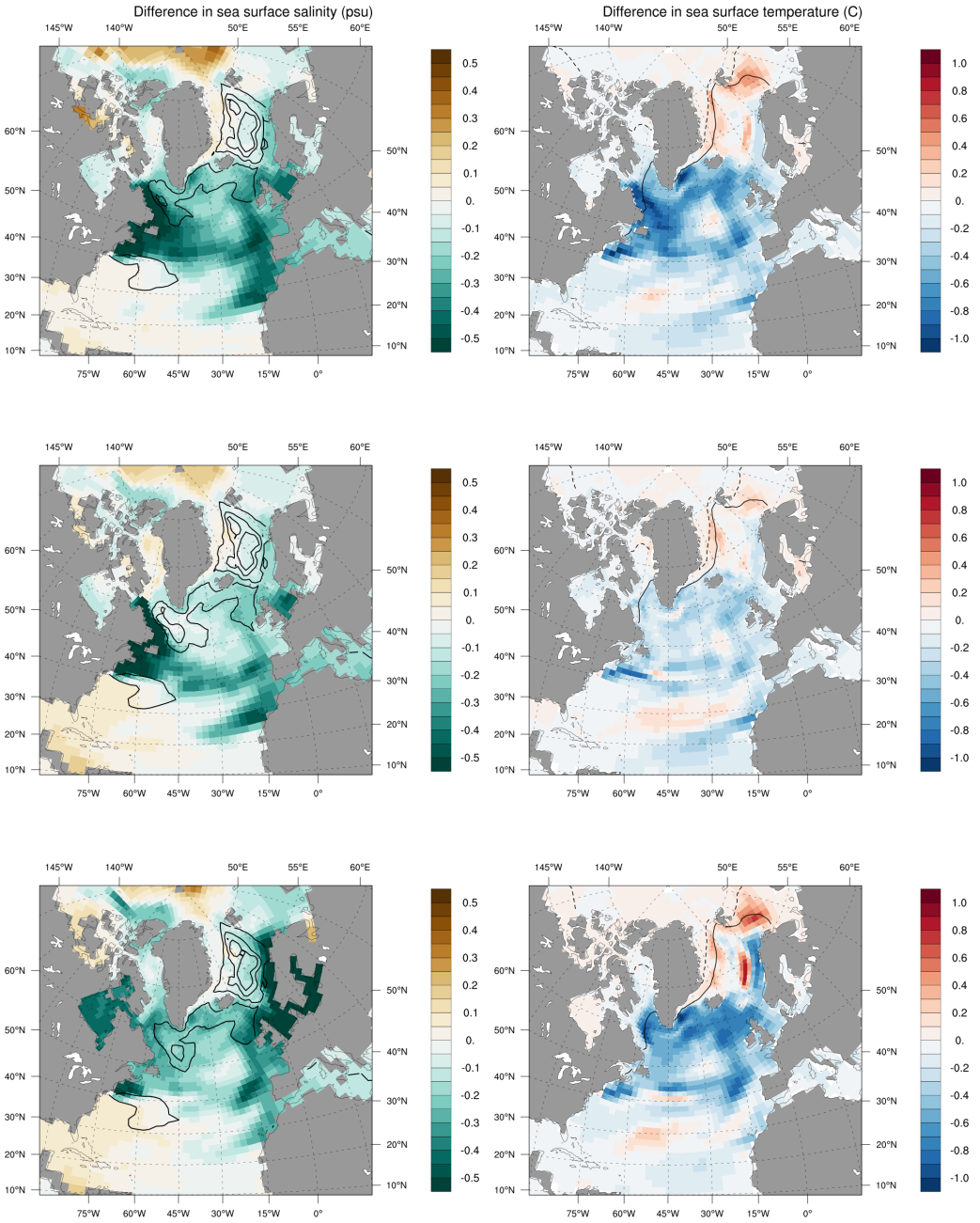

Figure 3.5: Difference in 200-years mean SSS (psu; left) between hosing experiment and CTRL. Isolines denote mixed layer depth (m; 500 m, 1,500 m, 2,500 m, and 3,500 m). Difference in 200-years mean SST (°C; right) between hosing experiment and CTRL. Isolines denote sea ice concentration of 15% in hosing experiment. Solid line corresponds to winter and dashed to summer sea ice concentrations. Hosing experiments are IB (top), FWPS (middle), and FWNA (bottom). All differences are calculated before the AMOC collapse at the input rate of 0.04 Sv.

than in the experiment IB. Hence, in the experiment FWPS, less freshwater interacts with the deep water formation in the North Atlantic than in

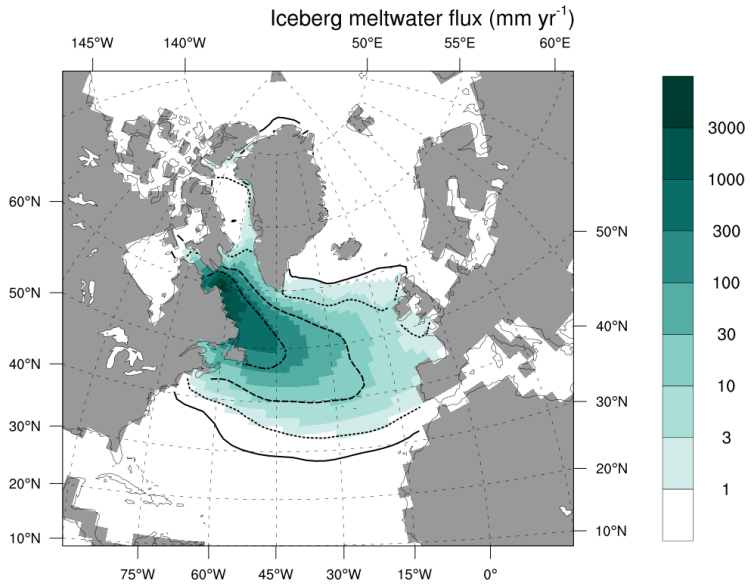

Figure 3.6: 200-years mean iceberg meltwater flux (mm yr^{-1}) before the AMOC collapse at 0.04 Sv. Isolines denote iceberg volume (solid $10^6 m^3$, dotted $10^7 m^3$, dashed $10^8 m^3$, dashed-dotted $10^9 m^3$). Input rate in FWNA is 140 mm yr^{-1}, and 20,626 mm yr^{-1} in IB, IBnoLH, and FWPS. Note the logarithmic scale of the colorbar.

the experiment IB. The part of released freshwater that joins the STG is advected to the north-eastern North Atlantic where it joins the Canary Current, causing a freshening that is strong but not as strong as in the experiment IB (Fig. 3.5).

In the experiment FWNA, the freshwater injection is uniformly distributed between 50° and 70°N (Fig. 3.1). This results in significant freshening in the north-eastern North Atlantic, along the Scandinavian coast and in the North and the Baltic Seas. The freshening also occurs in the Hudson Bay and in the north-western North Atlantic. These areas in the north-eastern and the north-western North Atlantic are parts of the latitude belt where released freshwater is injected (Fig. 3.5). Such a hosing allows freshwater to immediately affect areas of deep water formation in the Labrador and the Irminger Seas as well as in part of the Nordic Seas. This results in the highest rate of freshwater accumulation in the areas of deep water formation, leading to a stronger stratification of the water column as compared with other hosing experiments. The freshening along the Canary Current is relatively small when compared with other hosing experiments as most of the released freshwater is injected into the SPG and only a small part is advected to the STG.

In all experiments, the SST decreases in the Labrador Sea and the

northern North Atlantic and slightly increases in the Nordic Seas. The warming in the Nordic Seas can be attributed to the advection and upwelling of warm subsurface water from the south, transported with the SPG. The ocean surface cooling is a feedback to the hosing, namely, a decrease of the northward heat transport (Fig. 3.3). The enhanced cooling in the experiment IB is also a result of the additional ocean heat loss to melt icebergs. In the experiment IB, the maximal cooling occurs in the Labrador Seas, the area with a high iceberg melt rate (Fig. 3.6). As a response to cooling, sea ice increases and slightly extends eastward into the Labrador Sea and further to the east of Greenland (Fig. 3.5, right column).

Different types of hosing results in different freshening patterns. In the experiment IB, the meltwater is heterogeneously distributed across the northern North Atlantic. This results in the more realistic interaction of iceberg meltwater with deep water formation areas due to accounting for the physics of icebergs as compared to the freshwater experiments. In the experiment FWPS, the released freshwater is located in the western part of the northern North Atlantic resulting in the strongest freshening there. In this experiment, the distance between the hosing site and deep water formation areas is the most remote. Moreover, a significant amount of freshwater is captured by the STG that prevents it from being advected to deep water formation areas. Both these effects result in less freshwater accessible in deep water formation areas among all hosing experiments. In the experiment FWNA, some part of released freshwater is injected directly at deep water formation areas resulting in the highest freshening rate in these locations, causing an immediate interaction between the released freshwater and deep water formation areas.

3.3.3 The AMOC sensitivity to latent heat needed to melt icebergs

Treating calved ice mass as icebergs rather than as a direct freshwater input results not only in a different spatial pattern of meltwater injection locations but also in a cooling of the surrounding ocean due to the latent heat required for iceberg melting. To understand the effect of this cooling on the iceberg meltwater flux and the ocean response, I compare two iceberg experiments with and without the latent heat loss from the ocean (IB and IBnoLH). For the analysis, I consider the system response over the entire experiments (IB and IBnoLH; Fig. 3.3, green lines) and the time slice at the input rate of 0.04 Sv to derive the difference between two iceberg

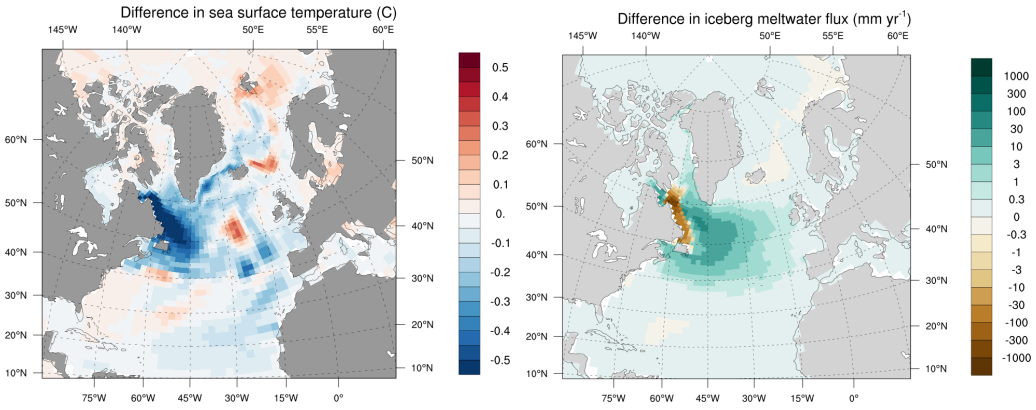

Figure 3.7: Difference in 200-years mean SST (°C; left) and difference in 200-years mean iceberg meltwater flux (mm yr^{-1}; right) between IB and IBnoLH before the AMOC collapse. Note the logarithmic scale of the colorbar on the right.

experiments.

A comparison shows that the maximal ventilated volume, the AMOC strength, and the heat transport response to hosing are very similar in both experiments IB and IBnoLH (Fig. 3.3). This clearly demonstrates that the effective meltwater induced by the iceberg migration is the main cause for the differences between the IB and the FWPS, and the IB and the FWNA experiments. There are, however, differences. In the experiment IB, SST becomes colder in a response to the additional heat loss due to iceberg melting (Fig. 3.3, shown for the northern North Atlantic, ∼1.5°C SST difference at the maximal input rate of 0.35 Sv). This cooling results in more sea ice (Fig. 3.3; nearly twofold sea ice coverage increase at the maximal input rate). Another effect of the additional cooling is that the collapse rate in the experiment IBnoLH is approximately 0.02 Sv higher than in IB (Fig. 3.4).

To understand the difference between the two iceberg experiments, I compare SST and iceberg meltwater flux anomalies between the experiment IB and IBnoLH (Fig. 3.7). Freshening and cooling have different effects on the potential water density that defines the water column stability and, consequently, the AMOC strength (see chapter 3.3.1). In the experiment IB, ocean temperatures are colder due to ocean heat loss in response to iceberg melt. Temperatures are colder specifically in areas with high iceberg concentrations, close to release sites. Therefore, the experiment IB should result in a stronger destabilization of the water column, as compared to IBnoLH. However, in both experiments, temperature effect on density is only

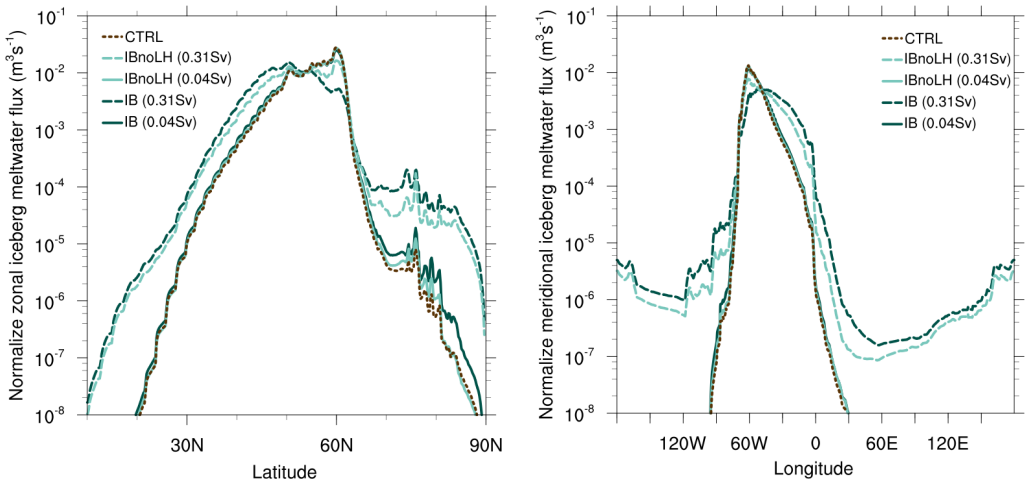

Figure 3.8: Normalized zonal (left) and meridional (right) iceberg meltwater flux (m^3 s^{-1}). Note that Y-axis is logarithmic.

half an order of magnitude of the freshening effect, hence, both experiments show a similar potential density decrease and water column stabilization, causing the AMOC strength to decrease. It should be noted, that additional cooling due to latent heat loss from the ocean mainly occurs in areas close to the iceberg release site that is relatively remote from the main deep water formation area in the Nordic Seas.

In both experiments, patterns of iceberg meltwater flux are similar with the strongest iceberg melt happening close to the calving site (here shown for the full iceberg experiment IB, Fig. 3.6) but the signal strength is slightly different (Fig. 3.7; right). As the ocean temperature cools close to the release site in the experiment IB, there is less iceberg melt there than in the experiment IBnoLH and more melt in remote areas (Fig. 3.7; right). This indicates that icebergs in the experiment IB can drift further away from the calving site, releasing more meltwater closer to deep water formation areas when compared to the experiment IBnoLH (Fig. 3.7; right). The mean zonal iceberg meltwater flux also depicts iceberg expansion further from calving sites in the experiment IB (Fig. 3.8; left; solid lines). Meridional total iceberg meltwater extent has almost not changed between 90°W to 30°E (Fig. 3.8; right; solid lines). Note that after the AMOC collapse (Fig. 3.8, dashed lines), the difference in iceberg meltwater flux becomes stronger (more details in chapter 3.3.4) as a response to stronger changes of the ocean circulation.

Iceberg meltwater injection locations play a major role in the AMOC collapse, causing water column stabilization. The latent heat has a minor

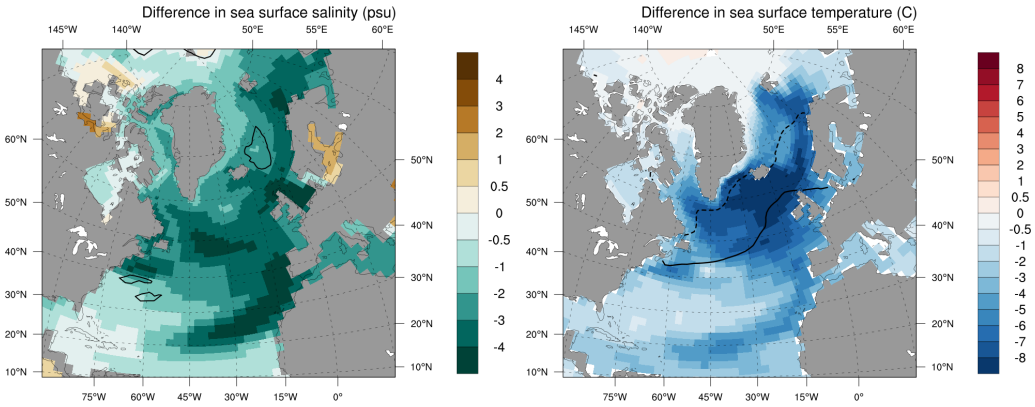

Figure 3.9: Difference in 200-years mean SSS (psu; left) between IB and CTRL. Isolines denote mixed layer depth (m; 500 m, 1,500 m, 2,500 m, and 3,500 m). Difference in 200-years mean SST (°C; right) between IB and CTRL. Isolines denote sea ice concentration of 15% in IB. Solid line corresponds to winter and dashed to summer sea ice concentration. All differences are calculated after the AMOC collapse at the input rate of 0.31 Sv.

role and, on the one hand, causes water column destabilization due to potential density decrease but, on the other hand, leads to iceberg lifetime increase resulting in more effective interaction with deep water formation areas. The overall outcome is the more effective water column stabilization and a lower collapse rate in the experiment IB as compared to the experiment IBnoLH. The latent heat needed to melt icebergs is also responsible for an increase of sea ice as a response to the additional surface ocean cooling.

3.3.4 Iceberg meltwater flux response to changes in the ocean circulation

After the AMOC collapse, the northern North Atlantic is much colder and fresher in all hosing experiments as compared to the experiment CTRL (Fig. 3.9). Collapsed states are very similar to each other but still reflect the type of hosing as it was before the AMOC collapse (chapter 3.3.2). Here I consider the iceberg response to changes in the ocean circulation. I also consider the hypothesis that instead of running an iceberg module with a model time step, one could calculate the iceberg meltwater flux once and scale it depending on the input rate. This would reduce the computational costs as the iceberg module would not be executed on every time step. For this, I examine the iceberg meltwater flux in the experiment IB before and

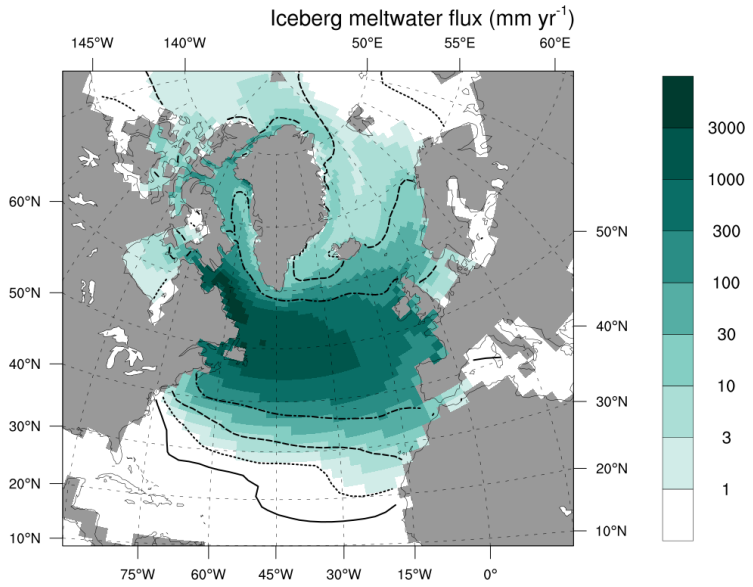

Figure 3.10: 200-years mean iceberg meltwater flux (mm yr^{-1}) after the AMOC collapse at 0.31 Sv. Isolines denote iceberg volume (solid $10^6 m^3$, dotted $10^7 m^3$, dashed $10^8 m^3$, dashed-dotted $10^9 m^3$). Input rate in FWNA is 1,086 mm yr^{-1}, and 159,849 mm yr^{-1} in IB, IBnoLH, and FWPS. Note the logarithmic scale of the colorbar.

after the AMOC collapse to understand how is it different depending on the AMOC strength with respect to diagnostic icebergs in the experiment CTRL. I chose two time slices corresponding to the mean input rate of 0.04 Sv at a strong AMOC mode and the mean input rate of 0.31 Sv at a weak AMOC mode. At an input rate of 0.31 Sv, the AMOC has collapsed for more than 500 years and the system is close to a new quasi-equilibrium state (Fig. 3.3).

In the collapsed AMOC state, the entire northern North Atlantic is covered by a freshwater lid and is much colder than the experiment CTRL (Fig. 3.9). An enhanced freshening occurs along the north-eastern North Atlantic and the Canary Current due to significant amount of icebergs melting there. The released iceberg meltwater is also advected there by the ocean circulation. The highest cooling rate is reached south of Iceland. In the experiment CTRL, this area is relatively warm, whereas after the AMOC collapse this area is covered by sea ice at least in winter resulting in most drastic cooling. Strong cooling is also evident along the Canary Current caused by the changes in the ocean circulation, iceberg melt and iceberg meltwater advection there by the ocean. Deep water formation is suppressed in the Labrador, the Irminger, and the Nordic Seas, with small remaining convection in the Nordic Seas with the maximal ventilated vol-

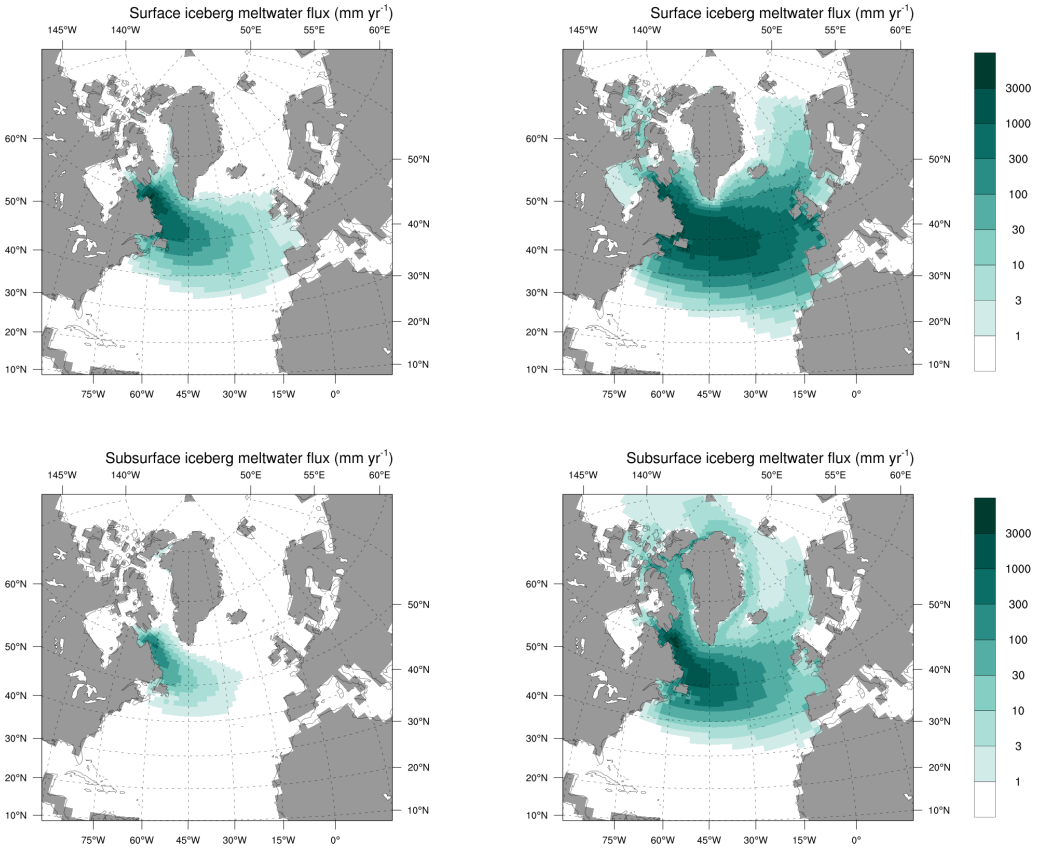

Figure 3.11: 200-years mean surface (top) and subsurface (bottom) iceberg meltwater flux (mm yr^{-1}) before (left) and after (right) the AMOC collapse. Note the logarithmic scale of the colorbar.

ume of $0.32 \times 10^{15} m^3$ (Fig. 3.3; Fig. 3.9, left). The AMOC strength at 26°N in 1000 m is 2.70 Sv (Fig. 3.3). The heat transport is reduced to 0.26 PW (at 26°N in Atlantic; Fig. 3.3) explaining the significant ocean cooling. The cooling leads to an increase of sea ice in the northern North Atlantic (Fig. 3.9; right). In summer, sea ice covers the Labrador Sea, the Denmark Strait, and part of the Nordic Seas, whereas in winter sea ice reaches 50°N with even higher southward expansion in the north-western North Atlantic. Only a small area near the British Isles stays free of sea ice.

After the AMOC collapse, the iceberg meltwater flux changes (Fig. 3.6, 3.10, 3.11). With much colder conditions, icebergs can enter the Arctic via Northwestern Passages and drift to the south, reaching to 20°N. At small input rates, icebergs mostly melt on the surface (Fig. 3.11). As a response to an input rate increase, surface melting decreases from 92% to 71% due to much colder surface conditions that prevents icebergs from melting. In the Arctic, icebergs mainly melt in the subsurface as the ocean

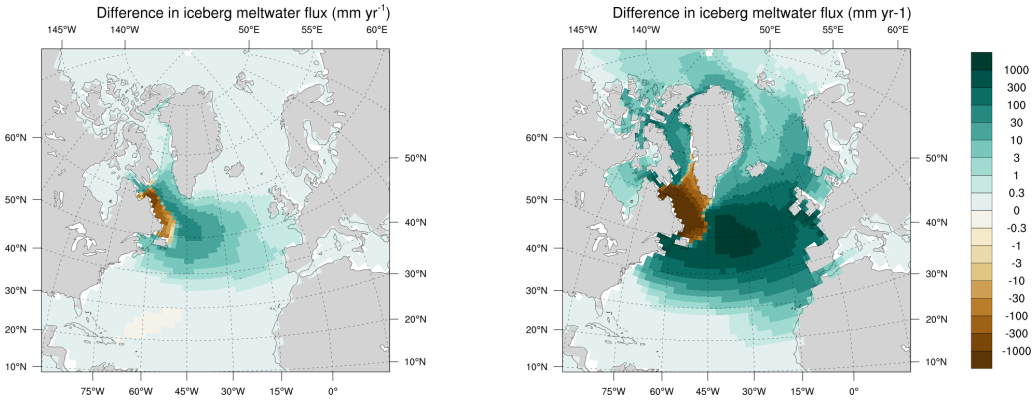

Figure 3.12: Difference in 200-years mean iceberg meltwater flux (mm yr^{-1}) between IB and CTRL before (left) and after (right) the AMOC collapse. Note the logarithmic scale of the colorbar.

surface is close to freezing point that limits iceberg melting. The mean zonal iceberg meltwater flux shows significant amount of icebergs in the Arctic and signs of icebergs even at 10°N but with a very small melting rate (Fig. 3.8). Icebergs' presence in the Arctic is also depicted in Fig. 3.8 (right) as iceberg meltwater flux increases to west of 90°W and east of 30°E. Therefore, changes in the ocean circulation cause significant changes in the iceberg meltwater spatial pattern with an increase of subsurface melting allowing more icebergs to drift further away from the calving sites.

To discern the effect of the input rate increase from the effect of the ocean circulation changes induced by melting icebergs, I compare iceberg meltwater flux in the experiment IB with the diagnostic iceberg meltwater flux in the experiment CTRL before and after the AMOC collapse (Fig. 3.12). For two different input rates, both anomalies show enhanced melting of diagnostic icebergs close to the release location. This is explained by the warmer ocean in the experiment CTRL as it is not affected by icebergs and stays unperturbed. The effect enhances with the input rate increase as a higher input rate causes more drastic circulation changes in the experiment IB. These changes induce differences in the iceberg meltwater spatial extent. Thus, at a strong input rate when AMOC is weak in the experiment IB, the ocean is cold, and icebergs can drift significantly further away from calving sites entering the Arctic and reaching as far south as 20°N. At a strong input rate but unaffected ocean, iceberg meltwater flux extent does not significantly differ from the extent of a small input rate (not shown). This indicates that icebergs can not drift far away from calving sites and,

therefore, can not reach the Arctic and Canary Current. Moreover, in the experiment IB, icebergs can drift to the Nordic Seas, which does no occur to diagnostic icebergs in the experiment CTRL due to the warm ocean. Therefore, scaling from the iceberg meltwater pattern at a strong AMOC mode can not reproduce the iceberg meltwater flux at a weak AMOC mode The iceberg meltwater flux is circulation dependent and can not be prescribed and scaled depending on the input rate from a fixed iceberg meltwater flux.

4 Hosing experiments for the LGM climate

In order to test the sensitivity of the results described in the previous chapter to a different background climate, a similar set of experiments is performed for the LGM.

4.1 Spin-up and background climate for LGM conditions

The model set-up used here is identical to the one used for the simulations described in the previous chapter (see chapter 3.1). Atmospheric greenhouse gas concentrations and orbital parameters are shown in the Table 4. For the 5,900 year long spin-up simulation the forcing, topography, land-sea mask, glacial mask, rivers routing were kept constant at conditions corresponding to 21,000 yrs BP.

4.1.1 LGM reference ocean

The climate of the reference LGM experiment (hereafter referred to as lgmCTRL) is very different from the climate of the reference pre-industrial experiment CTRL. Results shown are averaged over the entire 7,500 years of the experiments CTRL and lgmCTRL. The simulated global mean 2-m air temperature in LGM is 280.07 K that is 6.54 K colder than in pre-industrial with significantly stronger cooling over the Northern Hemisphere (Fig. 4.1). Reconstructions show a temperature difference between present and LGM of about -5.2 to -3.2 K (in review; Kageyama et al., 2020), indicating that model here simulates colder climate than the reconstructed data. The mean cooling over ocean points is 5.11 K, and over land 8.97 K. The strongest cooling over land is found over areas covered by ice sheets, which can be explained by the height changes associated with the ice sheets that extend over large parts of North America and Eurasia. The maximum cooling

Eccentricity	Perihelion	Obliquity	pCO_2	pN_2O	pCH_4
0.0189938	294.238800	22.944859	187.37	205.10	381.73

Table 4: LGM orbital parameters and greenhouse gas concentrations. pCO_2 is given in ppm, pN_2O and pCH_4 in ppb.

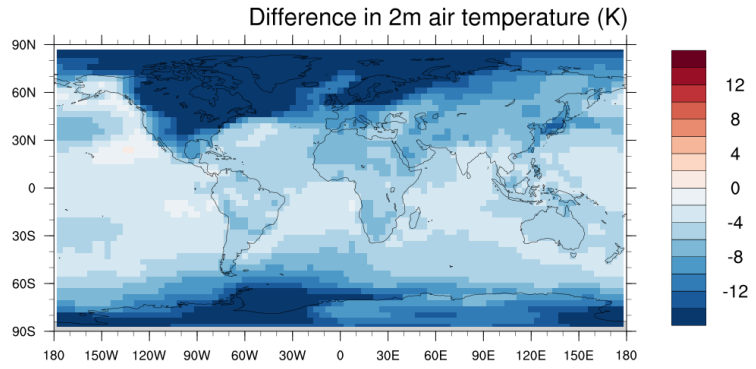

Figure 4.1: Differences in 2-m air temperature (K) between lgmCTRL and CTRL.

exceeds 30 K over the Laurentide ice sheet in the northern part of North America and 20 K over the Fennoscandian ice sheet in northern Europe.

The global mean SSS in LGM is 35.08 psu, which is 0.73 psu saltier than in the pre-industrial experiment. This corresponds to nearly 80 m lower sea level in the GLAC-1D reconstruction (Tarasov et al., 2012). The global mean SST in LGM is 14.01°C, 3.23°C colder than the pre-industrial. The highest salinity and/ or temperature differences are reached in the northern North Atlantic, the Labrador Sea and the Baffin Bay, the Nordic Seas, and the Arctic (Fig. 4.2, 4.3). Therefore, I will focus on these regions.

SSS in the Arctic in lgmCTRL is 3.18 psu saltier compared to CTRL. The intense halocline, associated with relatively fresh water at the surface and salty water in lower layers, which is characteristic for present-day climate conditions in the Arctic, is absent in lgmCTRL. The LGM SSS in the Arctic is even higher than in the subpolar North Atlantic. In the subpolar North Atlantic, the SSS is lower than at pre-industrial, which is a strong freshening signal given the generally higher salinities in the LGM ocean. This salinity pattern is a consequence of the enhanced sea ice formation in the Arctic during LGM, the enhanced sea ice export from the Arctic to the subpolar North Atlantic and subsequent melting (Fig. 4.4). Strong negative SSS anomalies south of the British Isles in the northern North Atlantic are due to different river rerouting of major North and Central European rivers where the Fennoscandian ice sheets blocks the normal river discharge (e.g., Neva, Elbe, Rhine) to the Baltic and the North Sea and through the English Channel. Due to the river rerouting of these European rivers, their mouths are now located significantly further away from the Nordic Seas and the Arctic, and, therefore, these rivers contribute less to the freshening in high latitudes. Other strong negative anomalies are observed south to

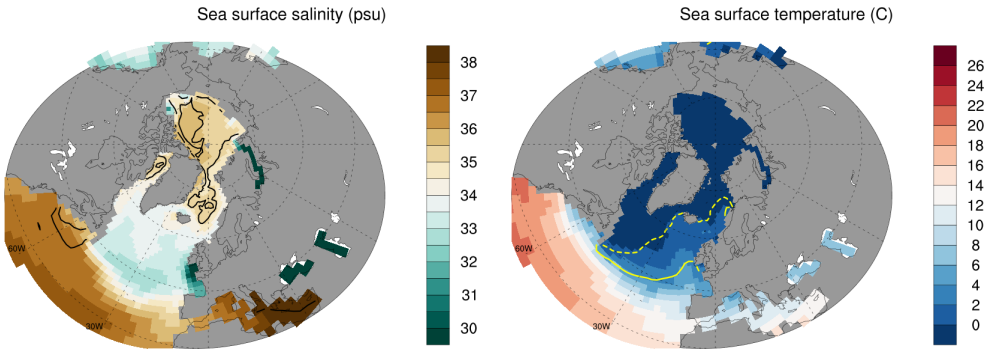

Figure 4.2: SSS (psu; left) overlayed by maximal mixed layer depth (m; 500 m, 1,500 m, 2,500 m, and 3,500 m); and SST (°C; right) overlayed by sea ice extent (yellow lines; winter (solid) and summer (dashed) sea ice concentration of 15%) in lgmCTRL.

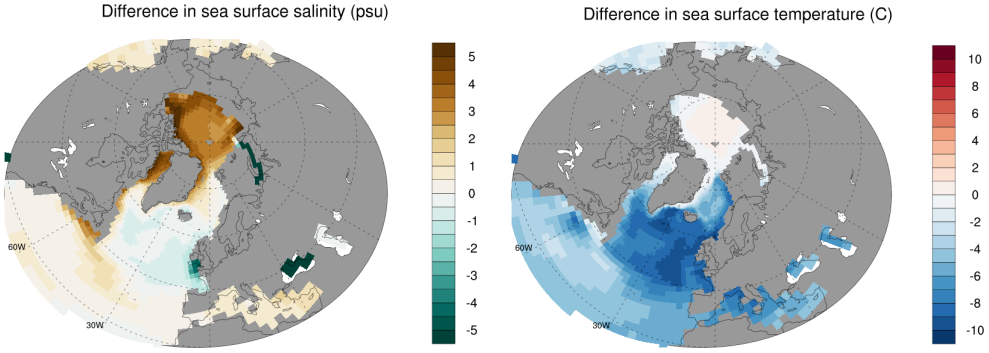

Figure 4.3: Differences in SSS (psu; left) and SST (°C; right) between lgmCTRL and CTRL.

Severnaya Zemlya in the Arctic which can be explained by a rerouting of Siberian rivers in LGM (Ob and Yenisey).

The SST difference in the Arctic between LGM and pre-industrial is very small 0.37 °C, which can be explained by the fact that the Arctic SST in CTRL is close to the freezing point. The freezing point limits the achievable cooling and thus the signal in SST is rather small in contrast to the strong cooling of the overlying air. The SST in the Nordic Seas and the Labrador Sea at LGM is by 4.23 °C and 3.83 °C lower, respectively, due to presence of sea ice in LGM. The highest SST anomaly of 6.14 °C is reached in the northern North Atlantic with the strongest decrease in the Irminger Sea, which is covered year round by sea ice at LGM. The sea ice export through Denmark Strait contributes to this. At pre-industrial, relative deep winter mixed layers limit winter cooling due to the large heat capacity of the water

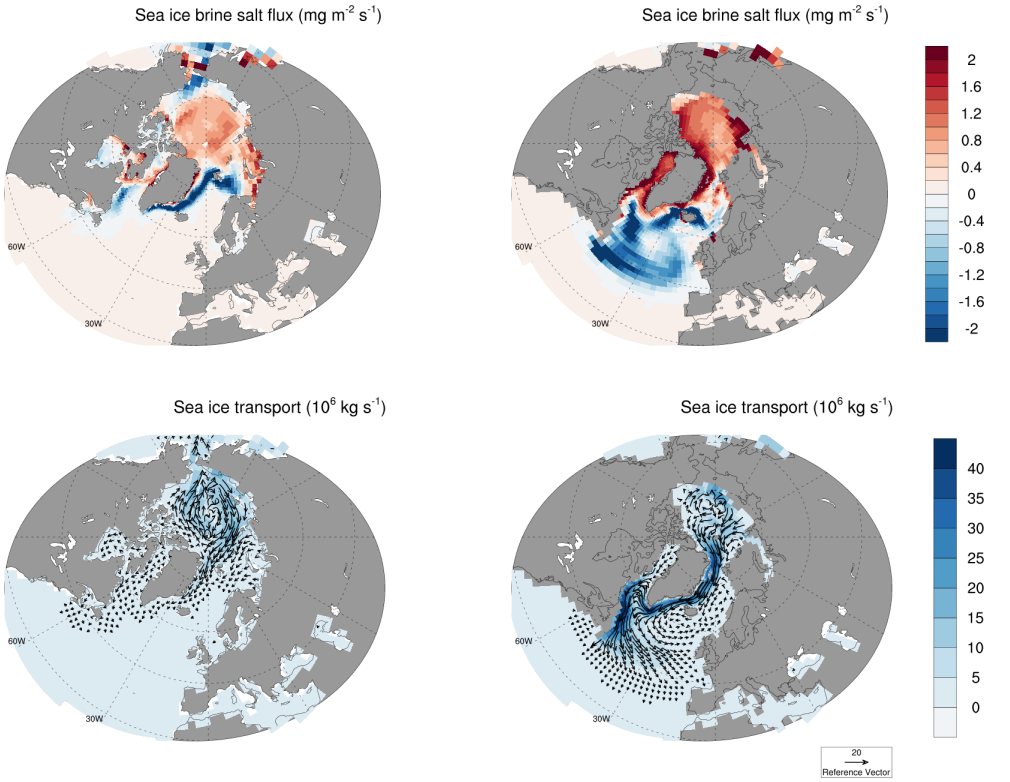

Figure 4.4: Brine release (mg m^{-2} s^{-1}; top) and sea ice transport (10^6 kg s^{-1}; bottom) in CTRL (left) and lgmCTRL (right).

column. Sea ice export through Denmark Strait is small for pre-industrial. At LGM, the water column is rather stable in the Irminger Sea. Thus, the deepest mixed layer depth at LGM in the northern North Atlantic does not exceed 500 m and is located to the south-east of Iceland (Fig. 4.3). At pre-industrial, the mixed layer depth in the Irminger Sea reaches 1,500 m and 1,000 m to the south-east of Iceland indicating that there is much more water to be cooled (Fig. 3.2, 4.2). The entire North Atlantic SPG shows strong cooling at LGM. Here the surface freshening stabilizes the water column and most of the SPG is covered by sea ice in winter (Fig. 4.3, 4.2).

At LGM, the Arctic is the main area of deep water formation in the Northern Hemisphere, some deep water also forms in the Nordic Seas. The maximal mixed layer depth in the Arctic reaches 3,400 m with a corresponding maximal ventilated volume of $3.99\times$ 10^{15} m^3. In Nordic Seas, the maximal mixed layer depth is nearly 2,800 m with a maximal ventilated volume of $0.53\times$ 10^{15} m^3 (this value is four times smaller than in the pre-industrial experiment). Intermediate water forms in the Baffin Bay and south-west to Iceland with a maximal mixed layer depth of 700 m and 500

m, correspondingly. The Arctic deep water outflows via Fram Strait and mixes with deep water formed in the Nordic Seas. This water mass is the source for the overflow waters at Denmark Strait, which after entraining a large fraction of ambient water forms glacial NADW.

The main mechanism for the Arctic deep water formation during the glacial is rather different from the mechanism for pre-industrial and present-day formation of NADW. For the pre-industrial, freshwater forcing and heat flux forcing have an opposite effect on the density. Whereas the heat loss to the atmosphere enhances density, the positive net freshwater input from atmosphere and river runoff reduces surface density. In the present mode of operation with fast overturning, the effect of the cooling is dominating. For slow overturning rates and long exposure times to the surface interaction, the heat loss is strongly reduced and the effect of the freshwater gain is dominating. In the case of a strong AMOC, warm and salty subtropical water is advected to the Nordic Seas and the heat loss is strong resulting in a rather mild climate in north and west Europe.

During LGM, the sea ice export from the Arctic through Fram Strait is three times higher than at pre-industrial (0.22 Sv at LGM vs. 0.07 Sv at pre-industrial). The main export route is along the east coast of Greenland through Fram Strait and continuing further through Denmark Strait into the subpolar north Atlantic (Fig. 4.4). As a consequence, the sea ice formation in the Arctic and the Nordic Seas is much higher than at pre-industrial resulting together with cold temperatures in a considerable brine release. Meteoric freshwater input (precipitation, river runoff) at LGM is only half of the pre-industrial value (0.08 Sv at LGM vs 0.16 Sv at pre-industrial). Most of this reduction can be explained by a reduction of river input into the Arctic due to a combination of reduced precipitation during LGM due to colder temperatures and a different river routing. Thus, the net freshwater forcing in the Arctic changes sign: for LGM there is a net negative freshwater forcing of -0.14 Sv, for pre-industrial, it is positive, 0.08 Sv. This has drastic consequences for the Arctic water column. Whereas today's Arctic is characterized by a very stable with a strong halocline and rather fresh surface waters, the simulated glacial Arctic is characterized by an almost homogenized water column close to freezing point with deep mixed layers, driven by haline surface forcing. Except for the temperatures rather similar to present-day net evaporative basins, like e.g. the Mediterranean or the Red Sea. Most of the sea ice melt takes place in the North Atlantic SPG, which is responsible for the low salinities in this area, explaining the

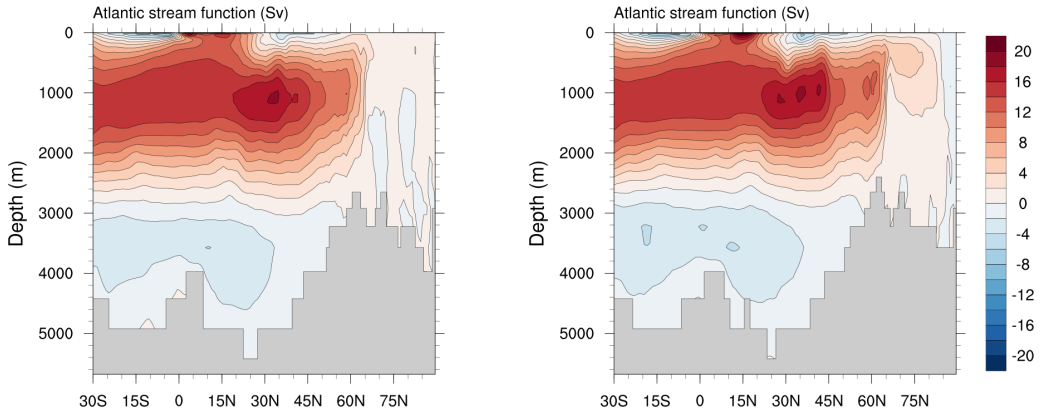

Figure 4.5: AMOC stream function (Sv) in CTRL (left) and lgmCTRL (right). Positive numbers denote clockwise flow direction, negative numbers denote counter-clockwise flow direction.

reversal of the salinity distribution compared to present-day.

Baffin Bay at LGM is also characterized by strong sea ice export and reactive high SSS. However, the water masses formed are not salty and dense enough to form deep water. After leaving through Davis Strait, they form an intermediate water mass in the glacial Labrador Sea. Pre-industrial Baffin Bay has as well a net brine release, but it is much weaker than at LGM. However, in pre-industrial, Baffin Bay also receives more than 1 Sv of fresh Arctic waters through the Canadian archipelago, which explains low salinities there and the strong anomalies with regard to LGM. There is no deep water formation in the North Atlantic SPG in LGM as this region is covered by a freshwater lid due to melting sea ice (Fig. 4.4).

The general picture of the NADW and AABW cells on the MOC plots for the Atlantic are very similar for pre-industrial and LGM (Fig. 4.5). The NADW cell has a maximum strength of nearly 17.5 Sv in the CTRL and the lgmCTRL at nearly the same location at 26°N in 1200 m depth. The AABW cell has a maximal strength of roughly 3 Sv in both experiments. In lgmCTRL, the border between the NADW and the AABW cells is flat and located at approximately 2,600 m depth, 200 m shallower than in the pre-industrial experiment CTRL. Pre-industrial NADW cell extends to 65°N, glacial NADW extends to 85°N.

Whereas the AMOC is almost the same for both climates, the horizontal circulation shows some differences (Fig. 4.6). At LGM, both STG and SPG, become stronger which is mainly caused by the stronger winds in LGM (Fig. 4.7). The increase in wind stress is caused by the presence of ice sheets and

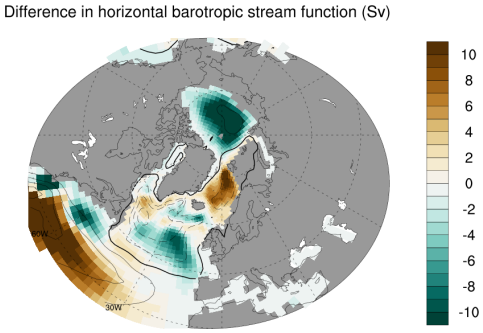

Figure 4.6: Difference in barotropic stream function (Sv) between lgmCTRL and CTRL. Contour lines depict gyres in CTRL.

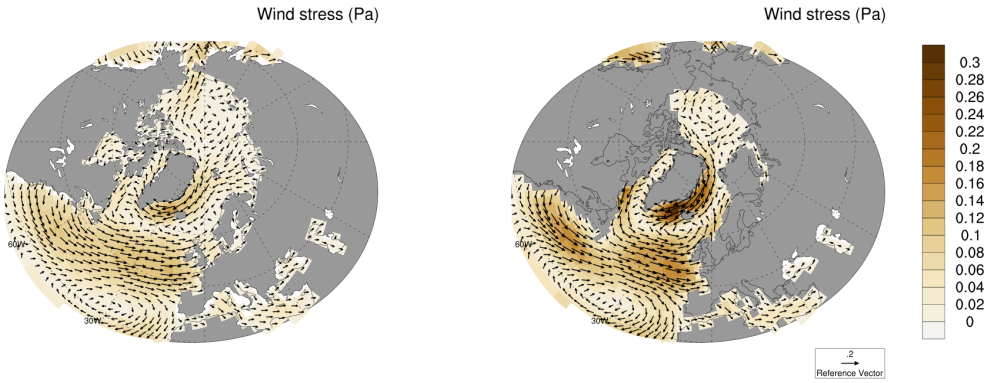

Figure 4.7: Wind stress (Pa) in CTRL (left) and lgmCTRL (right).

an increase in the meridional gradient of air temperature. The water masses in the North Atlantic STG are colder and saltier, the surface water masses in the subpolar are much colder and fresher (Fig. 4.3). In general, the density difference between the gyres has changed in the glacial simulation. In the central North Atlantic, the SPG extends further southward which contributes to the freshening to the south of the British Isles, in the Celtic Sea and Bay of Biscay. Off Newfoundland, the STG slightly extends to the north-west limiting the southward expansion of sea ice.

The northward Atlantic heat transport at LGM is higher than at pre-industrial with strongest anomalies around 30°N (Fig. 4.8). This coincides with the stronger STG in the North Atlantic. The heat transport at 26°N is 0.73 PW for pre-industrial conditions and 0.96 PW for LGM. Atlantic heat transport has two main drivers, meridional overturning and horizontal gyre circulation. Thus, northward heat transport in LGM is higher than in pre-industrial (Fig. 4.8). The strong northward heat transport is latitude

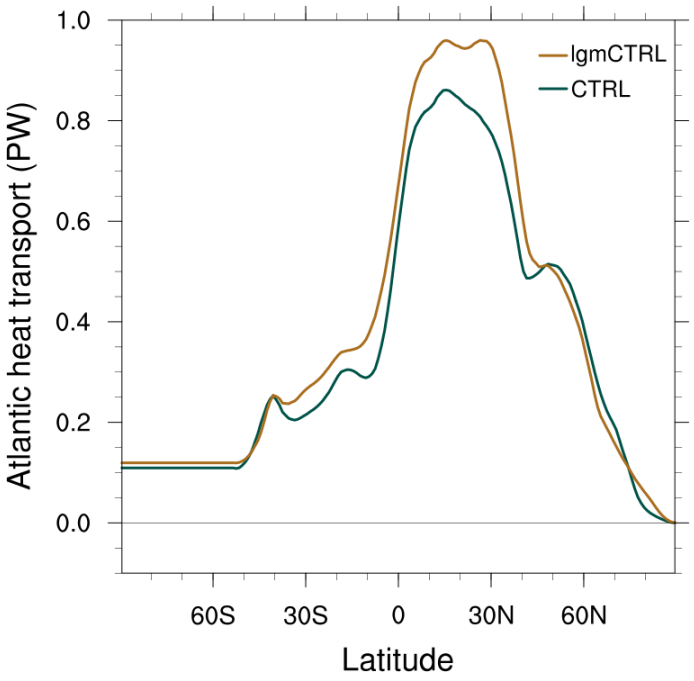

Figure 4.8: North Atlantic heat transport (PW) versus latitude in CTRL (green) and lgmCTRL (brown).

dependent and lies on the border between the STG and the SPG which is located close to 45°N (Fig. 4.6). North of 45°N, the northward heat transport is lower at LGM inspite of an intensified subpolar gyre. This can be explained by the reduced zonal temperature gradient.

The estimates from paleo record reconstructions based on different methods reveal contradictory glacial AMOC strength (e.g., Yu et al., 1996; McManus et al., 2004). Model studies also show different results. Thus, previous studies have pointed towards processes that explain why the AMOC remains strong in climate models during the LGM. Using simulations from the PMIP 3 and 4, Kageyama et al. (2020, in review) attributed a strong LGM AMOC in the participating models to changes in the atmospheric circulation over the North Atlantic and changes in the North Atlantic freshwater balance. Studies with coupled atmosphere-ocean models showed that the AMOC strength significantly dependents on the height of the North American ice sheet (Ullman et al., 2014; Klockmann, 2017). Changes in the atmospheric circulation are associated with an increased northward salt transport, which strengthens the NADW formation (Muglia and Schmittner, 2015). Only few models were able to simulate a weakening of the AMOC for LGM climate conditions, as shown from a comparison of model simulations

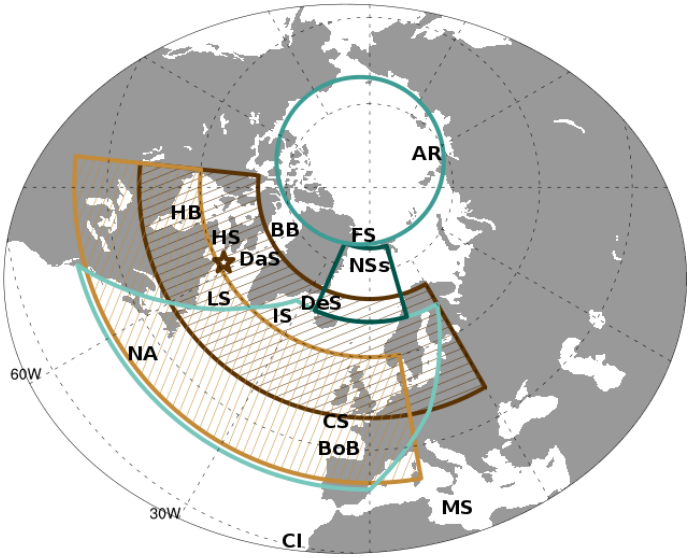

Figure 4.9: Location of hosing sites in the LGM experiments: brown star denotes the injection location in lgmIB, lgmIBnoLH, lgmFWPS; light brown box in FWNA40X60; dark brown box in FWNA50X70. Light green, medium green, and dark green boxes denote locations of the northern North Atlantic (NA), the Arctic ocean (AR), and the Nordic Seas (NSs) basins, respectively. Abbreviations are BB - Baffin Bay; BoB - Bay of Biscay; CI - Canary Islands; CS - Celtic Sea; DaS - Davis Strait; DeS - Denmark Strait; HB - Hudson Bay; HS - Hudson Strait; FS - Fram Strait; IS - Irminger Sea; MS - Mediterranean Sea; LS - Labrador Sea.

participating in PMIP 2 (Weber et al., 2007). In a study with an intermediate complexity model, the weakening of the AMOC during the LGM has been attributed to changes in the freshwater export out of the Atlantic drainage basin (Schmittner et al., 2002). A reduced net evaporation over the Atlantic during the LGM leads to a decrease of the SSS and reduction in NADW formation. While the SSS over the North Atlantic SPG is reduced in lgmCTRL, the deep water formation is mainly taking place in the Arctic, which explains the strong AMOC in the simulation.

4.2 Set-up of hosing experiments

For LGM, a similar set of idealized hosing experiments has been performed as for pre-industrial (Table 5), hosing sites are shown in Fig. 4.9. Icebergs were injected at a location in the Labrador Sea, off the location where for present-day Hudson Strait is located (lgmIB; brown star in Fig. 4.9). In a sensitivity experiment the effect of latent heat of icebergs is investigated by setting the latent heat of iceberg melting to zero (lgmIBnoLH). The effect of different freshwater hosing methods is calculated in three sensitivity

experiments: a point source at the same location used for iceberg hosing (lgmFWPS), and uniformly distributed over two different latitude belts in the Atlantic, between 50° and 70°N (lgmFWNA50x70; dark brown belt in Fig. 4.9); or within 40° to 60°N (lgmFWNA40x60; medium brown belt in Fig. 4.9) that is an additional experiment for LGM conditions. This range is chosen as it is closer to the "Ruddiman belt" where most of the IRD was found. This set is rather close to the one used for pre-industrial, allowing for a direct comparison with the results for the pre-industrial simulations analyzed in the previous chapter. The set of experiments is completed by a control simulation (lgmCTRL), which was already analyzed above.

As for the pre-industrial climate, the model is forced with a slowly changing input rate (rate of change of 0.1 Sv in 1,000 yr) starting from 0 Sv and increasing to 0.35 Sv in the first 3,500 years and then decreasing to 0 Sv within the next 3,500 years. After the hosing is turned off, the experiments are continued for 500 additional years until a new equilibrium state is reached.

4.3 Results

4.3.1 LGM ocean response to hosing

The design of LGM hosing experiments with a slowly varying input rate aims st understanding the system's sensitivity to the hosing strength and the different type of hosing (freshwater vs. icebergs) for climate conditions different from pre-industrial. In addition to timeseries of key variables from these experiments (Fig. 4.10), the AMOC strength vs. the input rate is shown in Fig. 4.12. The effect of the type of hosing on the AMOC sensitiv-

Experiment	Experiment description
lgmIB	Iceberg experiment
lgmIBnoLH	Iceberg experiment with no latent heat
lgmFWPS	Freshwater point source experiment
lgmFWNA50x70	Freshwater North Atlantic experiment with hosing between 50° to 70°N
lgmFWNA40x60	Freshwater North Atlantic experiment with hosing between 40° to 60°N
lgmCTRL	Control experiment

Table 5: List of LGM experiments.

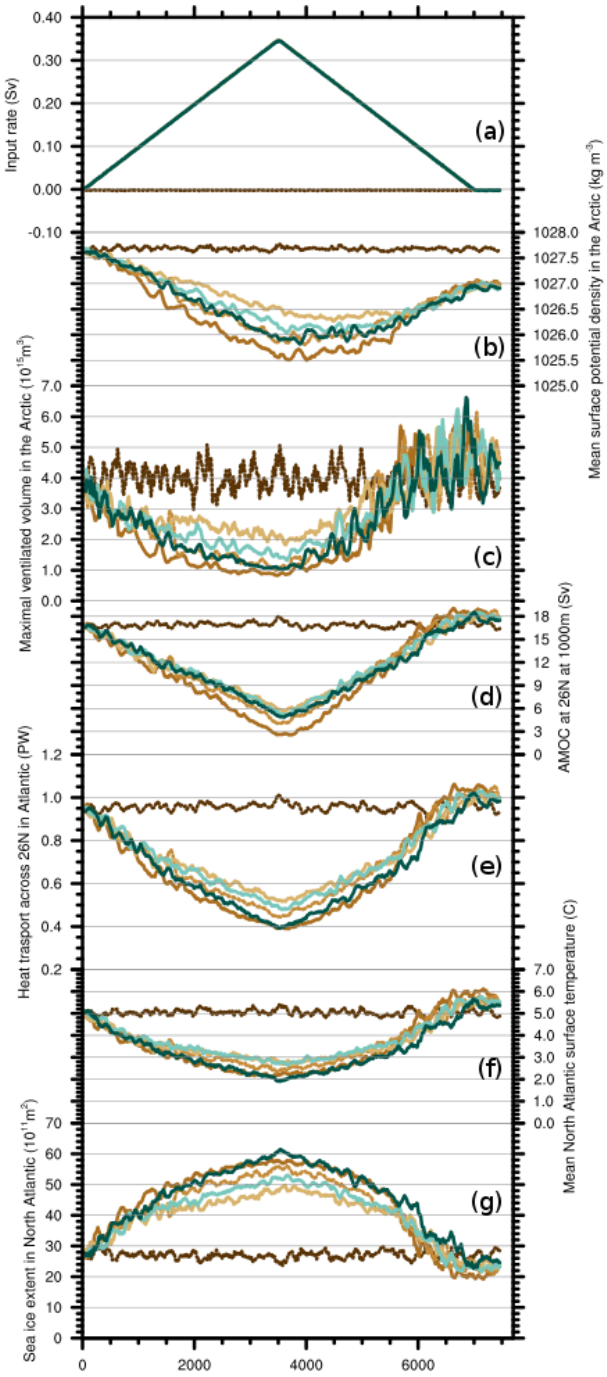

Figure 4.10: 100-years running mean of (a) input rate (Sv); (b) mean surface potential density in Arctic (kg m^{-3}); (c) maximal ventilated volume in Arctic (m^3); (d) AMOC at 26°N at 1,000 m (Sv); (e) heat transport across 26°N in Atlantic (PW); (f) mean SST in the northern North Atlantic (°C); (g) sea ice extent in the northern North Atlantic (m^2). Brown dotted line corresponds to lgmCTRL, light brown to lgmFWPS, medium brown to lgmFWNA40x60, dark brown to lgmFWNA50x70; dark green to lgmIB, and light green to lgmIBnoLH.

ity is much less pronounced for LGM climate than it is for the pre-industrial climate (compare Fig. 4.10 and Fig. 3.3). Part of the explanation is that for LGM climate condition, due to relatively remote disposition of release sites and the main deep water formation area, only a small part of released fresh/ meltwater interacts with the deep water formation area in the Arctic. This results in less effective and nearly linear ocean circulation response to hosing in LGM when compared with the pre-industrial experiments. The Nordic Seas deep water formation is less prominent in the LGM background climate. Therefore, all LGM hosing experiments perform rather similar without showing signs of abrupt mode transitions. The other part of the explanation is the mechanism of deep water formation. This aspect will be discussed further below.

In all LGM hosing experiments, nearly the same amount of the released fresh/ meltwater gradually arrives at the deep water formation in the Arctic, causing a gradual surface density decrease (Fig. 4.10). The same is true for the Nordic Seas surface density (timeseries are not shown). When the released fresh/ meltwater reaches areas of deep water formation in the Arctic and the Nordic Seas, the maximal ventilated volume starts to decrease as dense surface water mixes with less dense input fresh/ meltwater resulting in density decrease and consequent stabilization of the water column.

The weakening of the AMOC as a consequence of the imposed hosing has a strong effect on Arctic climate. The strong surface cooling leads to a strong increase of sea ice volume in the Arctic. The export of Arctic sea ice is reduced to two thirds of the value of lgmCTRL (Fig. 4.11). Cause is the enhanced stiffness of the thicker sea ice. Consequently the net sea ice formation (and the brine release in the Arctic) are reduced as well. The meteoric freshwater input into the Arctic is reduced by 10 to 15% due to the colder and drier climate over the Arctic and its drainage basin. The negative freshwater forcing of the Arctic is reduced from -0.14 Sv to -0.08 Sv. However, the forcing does not change its sign and the Arctic ocean receives a buoyancy forcing which tends to reestablish deep water formation in the Arctic basin.

This situation is qualitatively different from the pre-industrial. During the collapse of the AMOC, the net freshwater forcing of the Arctic surface ocean is reduced from 0.085 Sv to 0.02 Sv. Most of the effect are due to higher sea ice export through Fram Strait (increase from 0.065 Sv to 0.11 Sv). A slowing down of the AMOC has quite different effect on the SSS of the Arctic. In the pre-industrial climate, longer exposure times lead to a

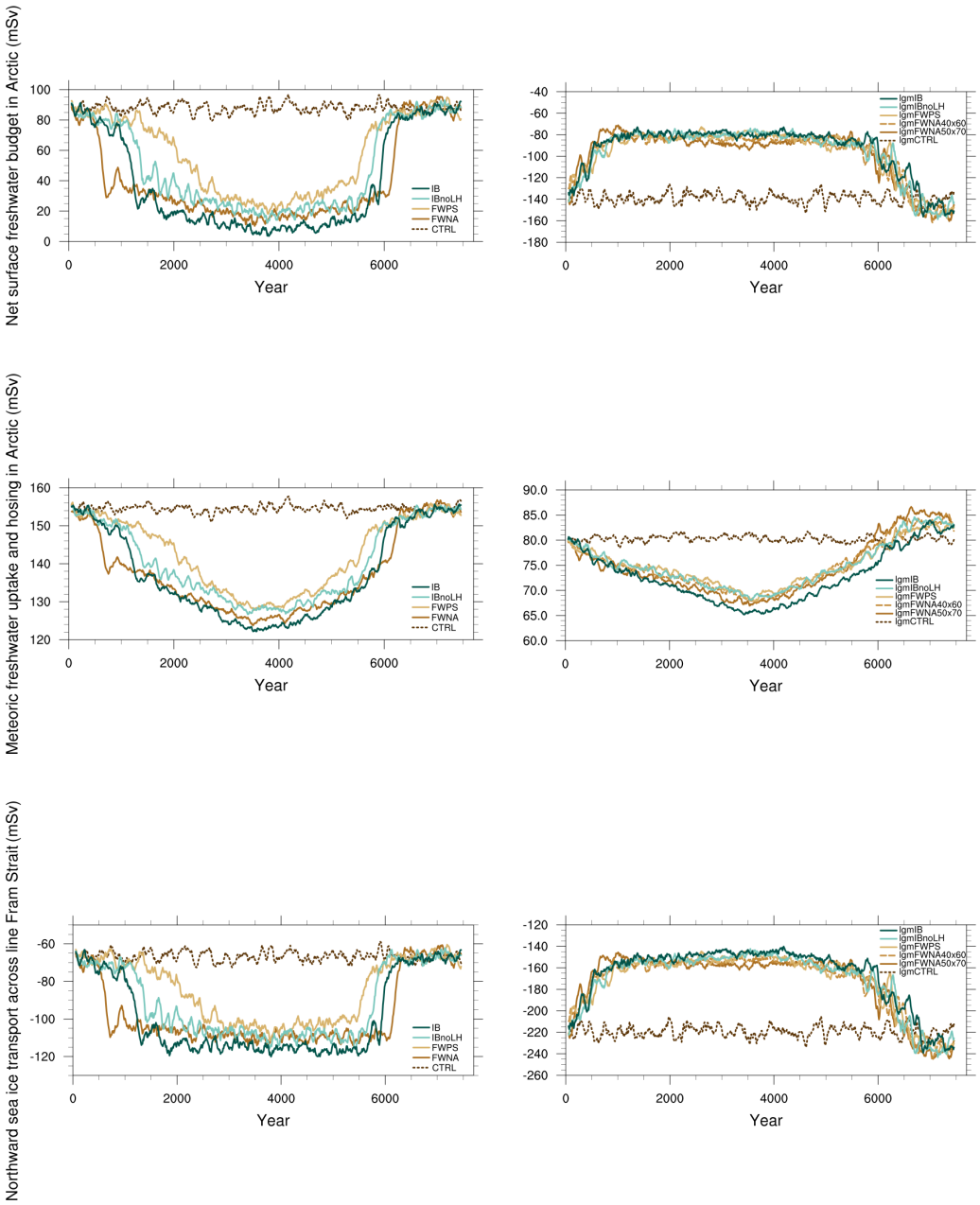

Figure 4.11: 100-years running mean of net surface freshwater budget in Arctic (mSv; top), meteoric freshwater uptake and hosing in Arctic (mSv; middle), and northward sea ice transport across line Fram Strait (mSv; bottom) in pre-industrial (left) and LGM (right) experiments. Net surface freshwater budget is a sum of meteoric uptake (including hosing) and sea ice transport.

further decrease in SSS (partially compensated by the enhanced sea ice export). For the glacial state, longer exposure times to negative freshwater fluxes lead to an increase of SSS, effectively destabilizing the water column. The only term preventing deep water formation in the Arctic is the fact that

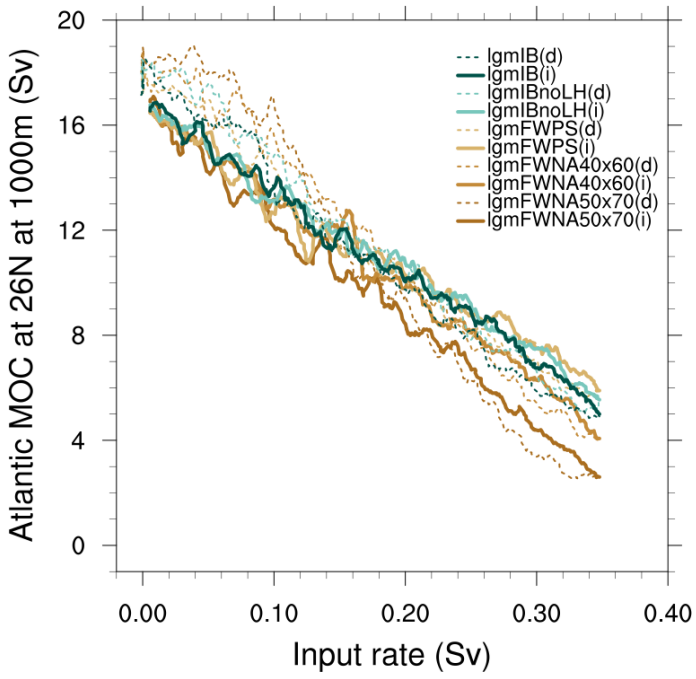

Figure 4.12: 100-years mean AMOC strength at 26°N at 1,000 m (Sv) versus the input rate (Sv) for the LGM climate. Solid lines (i) depict the first part of experiments when input rate increases; dashed lines (d) correspond to the second part of experiments when input rate decreases.

the near surface North Atlantic water, which constitutes the inflow into the Nordic Seas and the Arctic, is getting much fresher than the salinity effect due to direct freshwater forcing in the Arctic. The advective feedback, which is a main constituent of the possibility for multiple steady states of the AMOC in pre-industrial climate, has changed sign between the climate states and is a damping mechanism rather than a positive feedback.

Due to hosing in the LGM experiments, Denmark Strait overflow water is now a mixture of fresher and, consequently, less dense Arctic deep water, and the more fresh deep water formed in the Nordic Seas. Consequently, the entrainment of this fresher water masses leads to significantly less dense NADW properties south of Denmark Strait.

All hosing experiments perform very similarly, showing a rather similar freshening effect (Fig. 4.10). The surface density, the maximal ventilated volume, and the AMOC strength changes perform rather similar and do not depend on the type of hosing. Nevertheless, there are some differences in the response strength. The most different is the experiment lgmFWNA50x70 that shows the strongest decline as the 50° to 70°N band, where the freshwater is homogeneously injected, partly lies in the Nordic

Seas and, therefore, immediately interacts with the deep water formation there. This latitude band also lies closer to the deep water formation sites than the fresh/ meltwater input in the other hosing experiments, allowing more freshwater to reach the Arctic. The weakest decline, as in pre-industrial, is in the experiment lgmFWPS as the release location is the most remote from deep water formation areas. Both iceberg experiment lgmIB and lgmIBnoLH show a stronger response than in lgmFWPS but smaller than in lgmFWNA50x70, indicating that both freshwater experiments perform differently than the real interaction due to unrealistic freshwater spatial distribution. The additional experiment lgmFWNA40x60 performs more similar to the other freshwater hosing runs with respect to the icebergs experiment, indicating that the 40° to 60°N latitude band is a better approximation of the iceberg meltwater spatial distribution. The meltwater water pattern will be discussed in more details below (see chapter 4.3.3).

The coldest experiment is the experiment lgmIB that is explained not only by reduced northward heat transport but also by additional heat loss of the surface ocean required to melt icebergs (Fig. 4.10). Nearly the same or slightly reduced cooling shows the experiment lgmFWNA50x70 due to the comparably effective interaction with the deep water formation areas in the north and the subsequently highest decrease of the northward Atlantic heat transport. Experiments lgmIBnoLH and lgmFWPS show the weakest cooling effect among all experiments. This is a result of the less effective interaction with deep water formation areas due to the remoteness of fresh/ meltwater release locations resulting in a less effective decrease in heat transport. Experiment lgmFWNA40x60 shows a slightly smaller thermal response than the experiment lgmFWNA50x70 showing stronger heat transport reduction but weaker SST decrease when compared with the experiment lgmIB indicating that freshwater hosing can not fully replace the iceberg hosing.

Different SST cooling causes differences in the sea ice response. Thus, the sea ice in the northern North Atlantic, Labrador and Nordic Seas, and Arctic increases with an input rate increase (here shown only for North Atlantic in Fig. 4.10). Experiments lgmIB and lgmFWNA50x70 perform very similarly as a similar cooling rate causes similar sea ice response. Experiments lgmFWPS and lgmIBnoLH show the smallest sea ice increase that also is in agreement with SST and the heat transport changes. The experiment lgmFWNA40x60 shows slightly less effective increase in sea

ice than the experiment lgmFWNA50x70 that is also smaller than in the experiment lgmIB. From this, it can be concluded, that experiments with a direct freshwater injection can not fully reproduce the effect showing in experiments with icebergs due to a luck of the crucial mechanism behind icebergs' lifetime.

As in pre-industrial experiments, for the LGM climate, the AMOC strength declines with an input rate increase and increases with an input rate decrease (Fig. 4.12). In contrast to the set of experiments for pre-industrial climate, all experiments perform very similarly, showing a linear dependency of the AMOC strength on the input rate without abrupt changes. Therefore, the term AMOC-decline-response-rate is used instead of AMOC-collapse-response-rate. These values are expressed as hosing needed to change the AMOC strength by 1 Sv. The iceberg hosing experiments lgmIB and lgmIBnoLH have AMOC-decline-response-rates of -30.23 mSv in lgmIB and -31.48 mSv in lgmIBnoLH. The smallest AMOC-decline-response-rate is -25.08 mSv and is reached in the experiment lgmFWNA50x70. The closest to this value is the AMOC-decline-response-rate of -28.10 mSv in the experiment lgmFWNA40x60. The last freshwater experiment lgmFWPS, shows the highest AMOC-decline-response-rate of -32.70 Sv Sv^{-1} indicating the weakest circulation changes as a response to hosing.

Therefore, the most effective in the AMOC strength decline is the experiment lgmFWNA50x70, where the AMOC decreases to 2.60 Sv. The most resistant to hosing is the experiment lgmFWPS, where the AMOC strength minimum is 5.88 Sv. The experiment lgmIB has its minimum of 4.97 Sv that is close to the value of 4.09 Sv in the experiment lgmFWNA40x60. The experiment lgmIBnoLH performs in between of experiments lgmIB and lgmFWPS with a minimal AMOC strength of 5.43 Sv.

The AMOC recovery with a decrease of the input rate also performs very similar in all experiments, but rather different compared with the pre-industrial set of experiments, as the AMOC-recovery-response-rate is smaller than the decline rate for all hosing experiments (Fig. 4.12). The value is positive indicating the AMOC strength growth in response to decreasing hosing. Absolute values of the AMOC-recovery-response-rate is nearly 12% lower than the AMOC-decline-response-rate for all freshwater experiments, 29.02 mSv in lgmFWPS, 21.89 mSv in lgmFWNA50x70, and 24.93 mSv in lgmFWNA40x60. This value is about 14% lower for both iceberg experiments, 25.87 mSv in lgmIB and 27.50 mSv in lgmIBnoLH. This indicates that the recovery phase in LGM experiments is less resistant to

decreasing hosing than the decline phase and that the AMOC strength recovers faster to its initial strength.

Similar hosing experiments were performed for the LGM climate by Levine and Bigg (2008) and Bigg et al. (2011) with a constant input rate. Their study includes experiments similar to the experiment lgmIB (2D feedback) and lgmFWPS with hosing among other locations in the Hudson Strait. Their findings show similar circulation response to hosing as found here, namely, the AMOC strength decline, for both, icebergs and freshwater hosing. They also concluded that the injection location has an important role as it defines how much of released fresh/ meltwater reaches the convection region. Differently from this study, Levine and Bigg (2008) and Bigg et al. (2011) found an abrupt AMOC collapse in all experiments. In their study, collapses are more pronounced in freshwater experiments when compared with icebergs for hosing locations in the eastern North Atlantic. This can be attributed to the fact that the deep water formation area in their experiments is located in the central and eastern Atlantic that makes it easier for direct freshwater injection experiments to interact with it. For hosing sites in the Arctic and Europe, the AMOC response is slower as released hosing needs more time to reach the deep water formation area. Freshwater experiments are more efficient than iceberg experiments as the meltwater gradually arrives at the convection region. In the freshwater experiments, the freshwater is directly transported there. Similarly to this study, the system returns to its initial state after the hosing flux was turned off.

Jongma et al. (2013) performed hosing experiments similar to the lgmIB, lgmIBnoLH, and lgmFWNA50x70 at the LGM climate. In iceberg experiments, icebergs were released from the Laurentide ice sheet. Hosing in freshwater experiments was homogeneously distributed within the IRD belt. In their experiments, there are two areas of deep water formation, namely, to the south of Iceland in the North Atlantic and the Nordic Seas. Similarly to studies by Levine and Bigg (2008) and Bigg et al. (2011), the model was forced with a constant input rate. Jongma et al. (2013) found that the model response to hosing not depending on the hosing type shows a nearly linear AMOC strength decline with no signs of abrupt changes. The strongest decline shows the freshwater experiment, the full iceberg experiment shows a smaller decline but very close to the freshwater experiment. The experiment that does not account for the latent heat results in the smallest decline, whereas a similar experiment in this study performed very similar to other

experiments. Another similarity to this study is the strongest increase in sea ice in the full iceberg experiment indicating that the latent heat is an important component that should not be neglected. Overall, Jongma et al. (2013) showed that the Earth system reacts differently depending on the type of hosing. The freshwater experiments tend to show stronger effect of hosing and can not reproduce adequate changes in sea ice whereas full iceberg set-up solves these problems.

For the LGM climate, the AMOC strength linearly responds to hosing with faster recovery to the initial state. There is no indication of abrupt changes in the response and no signs of multiple steady states. The simulations show an almost linear return to the standard LGM AMOC strength with an overshooting and, after a couple of centuries, arrive at almost the same climate conditions but with global freshening of 1 psu. The recovery to the initial state in LGM experiments requires more time than in pre-industrial.

4.3.2 The AMOC sensitivity to the type of hosing

To get further insight into the response of the LGM climate to hosing, two time slices are further investigated: one time slice with rather small changes, where the system response is still linear, and one time slice with strong hosing and a weak AMOC, where potential nonlinearities in the response could already be visible. For the time slices, input rates of 0.04 and 0.31 Sv are chosen, in analogy with the analysis of the pre-industrial hosing experiments.

For LGM climate, the effect of different types of prescribed hosing is much less pronounced than in pre-industrial. This can partly be explained by the different location of the deep water formation in the Arctic, but also by the different contribution from heat fluxes and freshwater forcing to the surface buoyancy flux. In the freshwater hosing experiments, freshwater is injected either directly at calving sites (lgmFWPS) or within the latitude belt between 50° to 70°N (lgmFWNA50x70) or 40° to 60°N (lgmFWNA40x60). In both iceberg experiments, as a result of iceberg drift and melt, the iceberg meltwater flux is heterogeneously injected across the northern North Atlantic with a maximal melt rate at the calving site (see section 4.3.3). It is worth to note, that only in experiments lgmFWNA50x70 and lgmIB, for small prescribed input rates, fresh/ meltwater directly interacts with the deep water formation in the Nordic Seas. In all other

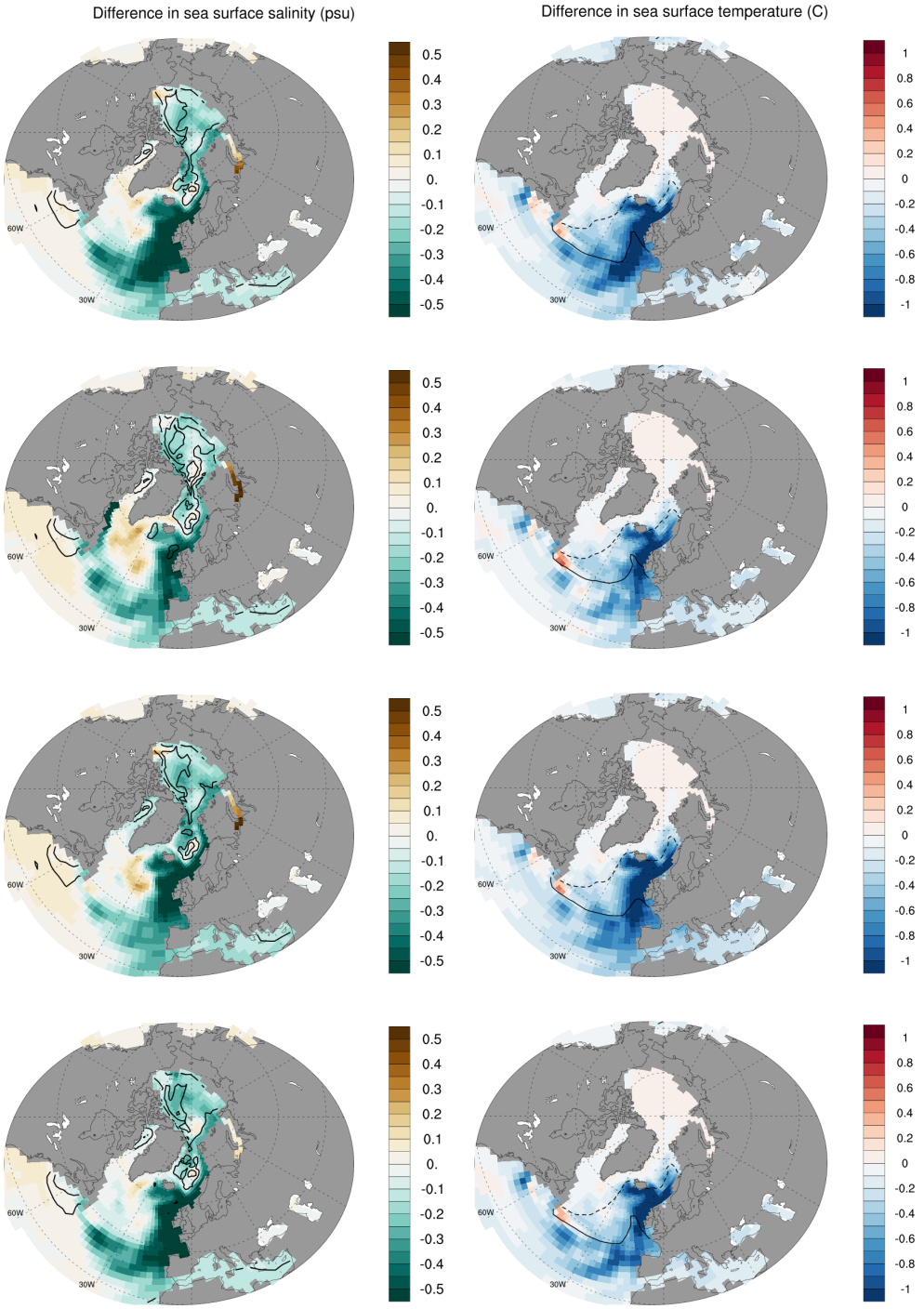

Figure 4.13: Difference in 200-years mean SSS (psu; left) between hosing experiment and lgmCTRL. Isolines denote mixed layer depth (m; 500 m, 1,500 m, 2,500 m, and 3,500 m). Difference in 200-years mean SST (°C; right) between hosing experiment and lgmCTRL. Isolines denote sea ice concentration of 15% in hosing experiment. Solid line corresponds to winter and dashed to summer sea ice concentration. Hosing experiments are lgmIB (first); lgmFWPS (second); lgmFWNA50x70 (third), and lgmFWNA40x60 (fourth). All differences are calculated at the input rate of 0.04 Sv.

experiments, there is no hosing related fresh/ meltwater input at the deep water formation areas, and fresh/ meltwater from hosing can only reach these locations by advection with the ocean circulation.

The freshening of the ocean surface is rather similar for all experiments (Fig. 4.13; left). Strongest anomalies can be seen in the north-east Atlantic with a clear extension into the Arctic. Anomalies in the western part of the North Atlantic SPG are generally close to zero. The freshening causes the water potential density decrease resulting in water column stratification that leads to the AMOC strength decrease and a corresponding reduction of the heat transport that, in its turn, induces ocean surface cooling (Fig. 4.10) and amplifies the freshening at the surface. Surface cooling is more pronounced in the north-eastern North Atlantic, as for salinity most pronounced in areas free of sea ice (Fig. 4.13). In the eastern part of the SPG, the enhanced stability leads to less mixing with deeper warmer and saltier water masses, which also reduced the heat release to the atmosphere in this region (not shown). The consequence is that at depth, warmer and saltier water that has lost less heat to the atmosphere is reaching the Arctic leading there to reduction of the sea ice formation, as some of the heat is needed to cool the subsurface ocean water. Consequence is reduced sea ice export from the Arctic (Fig. 4.11). This again leads to reduced sea ice export into the North Atlantic subpolar gyre with reduced sea ice melt in the western SPG, which obviously roughly compensates the effect of the prescribed hosing on SSS in this region (Fig. 4.13; left). The freshening effect in the STG is more pronounced in the experiment lgmFWNA40x60 as more freshwater is directly injected to the STG than in the experiment lgmFWNA50x70.

Overall, in all experiments, the freshening occurs in the eastern North Atlantic, the north-eastern part of the STG, the Nordic Seas, and the Arctic, and there is almost no freshening within the summer sea ice extent in the north-western North Atlantic (Fig. 4.13; left). The strongest freshening effect in the eastern North Atlantic is reached in the experiment lgmIB. This can be attributed to the fact that more iceberg meltwater is injected in this area when compared with other experiments. The smallest freshening effect occurs in the experiment lgmFWPS as all freshwater is released close to the Hudson Strait leaving Hudson Bay by advection with the Labrador current. The negative salinity anomaly in the STG spreads southward with the Canary Current. In the North Atlantic, a significant part spreads into the STG resulting in an only a small amount of released freshwater transport

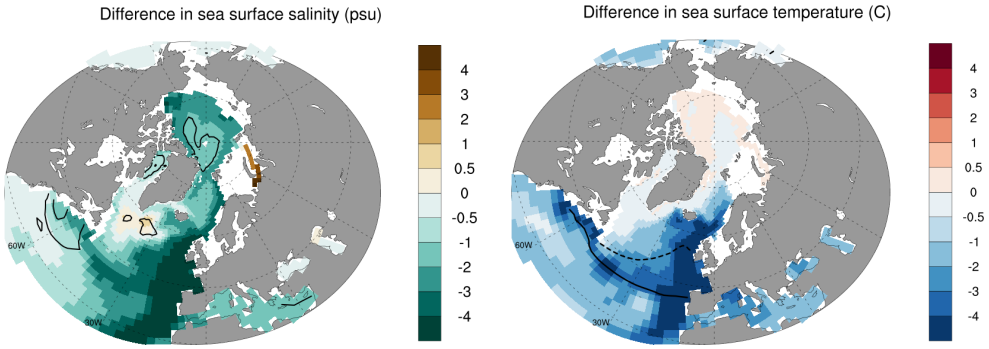

Figure 4.14: Difference in 200-years mean SSS (psu; left) between lgmIB and lgmCTRL. Isolines denote mixed layer depth (m; 500 m, 1,500 m, 2,500 m, and 3,500 m). Difference in 200-years mean SST (°C; right) between lgmIB and lgmCTRL. Isolines denote sea ice concentration of 15% in lgmIB. Solid line corresponds to winter and dashed to summer sea ice concentration. All differences are calculated at the input rate of 0.31 Sv.

to the north-eastern North Atlantic, the Nordic Seas, and the Arctic.

All experiments show cooling as a response to hosing due to the AMOC weakening and reduced heat transport (Fig. 4.13; right) and in the eastern North Atlantic, due to reduced wintertime mixing of surface water with the underlying warmer and saltier water masses. Areas covered by sea ice and with ocean temperatures close to freezing point cannot show a substantial cooling, as the ocean temperature is limited by the freezing point. The strongest cooling is reached in the experiment lgmIB where the melting of icebergs extracts additional heat from the uppermost part of the ocean.

At an input rate of 0.31 Sv, the effect of the weak AMOC on climate is dominant. The effect of the type of hosing is much smaller. Therefore, SSS and SST anomalies are shown only for the iceberg experiment lgmIB (Fig. 4.14). Similarly to the ocean response to a prescribed input rate of 0.04 Sv, freshening and cooling are the strongest in the eastern part of the North Atlantic SPG, where no sea ice is simulated, and in the north-eastern part of the STG in the domain of the Canary Current. The Arctic ocean SST has not significantly changed as it is close to the freezing point in all experiments. The deep water formation in the Arctic and Nordic Seas has ceased, but with weak stratification in some places extending down to 1,000 m (Fig. 4.14). The northward Atlantic ocean heat transport is reduced by approximately 50% of its value in the unperturbed experiment lgmCTRL (Fig. 4.10). Cold conditions cause sea ice expansion with the winter sea ice extent covering the entire North Atlantic up to 40°N (Fig. 4.14).

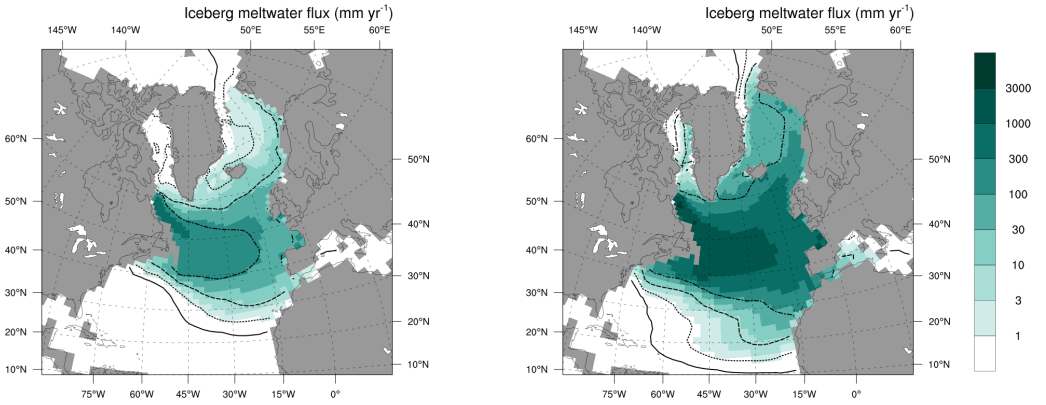

Figure 4.15: 200-years mean iceberg meltwater flux (mm yr^{-1}) at the input rates of 0.04 Sv (left) and 0.31 Sv (right) in lgmIB. Isolines denote iceberg volume (solid $10^6 m^3$, dotted $10^7 m^3$, dashed $10^8 m^3$, dashed-dotted $10^9 m^3$). Input rate in lgmFWNA50x70 is 210 mm yr^{-1}, 157 mm yr^{-1} in lgmFWNA40x60, and 20,861 mm yr^{-1} in lgmIB, lgmIBnoLH, and lgmFWPS at 0.04 Sv. Input rate in lgmFWNA50x70 is 1,630 mm yr^{-1}, 1,220 mm yr^{-1} in lgmFWNA40x60, and 161,675 mm yr^{-1} in lgmIB, lgmIBnoLH, and lgmFWPS at 0.31 Sv. Note the logarithmic scale of the colorbar.

4.3.3 Iceberg meltwater flux response to changes in the ocean circulation

In this subsection, the distribution of the iceberg melting and the effect of changes in the ocean due to the iceberg melting are discussed. The analysis focuses on the experiment lgmIB. After release off Hudson Strait, icebergs are transported with ocean currents to the open ocean south-eastward. In areas with high sea ice concentrations, in the Baffin Bay and in the Arctic, iceberg drift velocities are mainly determined by sea ice velocities. In the open ocean, iceberg velocities are mainly determined by ocean currents. The spatial distributions of the iceberg meltwater flux for input rates of 0.04 Sv and 0.31 Sv are shown in Fig. 4.15. In the open ocean, the effect of ocean currents and strong westerly winds define the drift path of the icebergs. Icebergs drift as far north as the Nordic Seas, where the released iceberg meltwater directly interacts with the local deep water formation. To the south-east, icebergs drift as far as the Canary Islands. Icebergs from the ice stream through Hudson Strait do not reach the Arctic as the southward flow of sea ice through Fram Strait prevents a propagation into the Arctic. Therefore there is no direct interaction between Arctic deep water formation and melting of icebergs.

The pattern of iceberg melting shows a marked effect of the climate changes due to a strong weakening of the AMOC (Fig. 4.15). The cooling

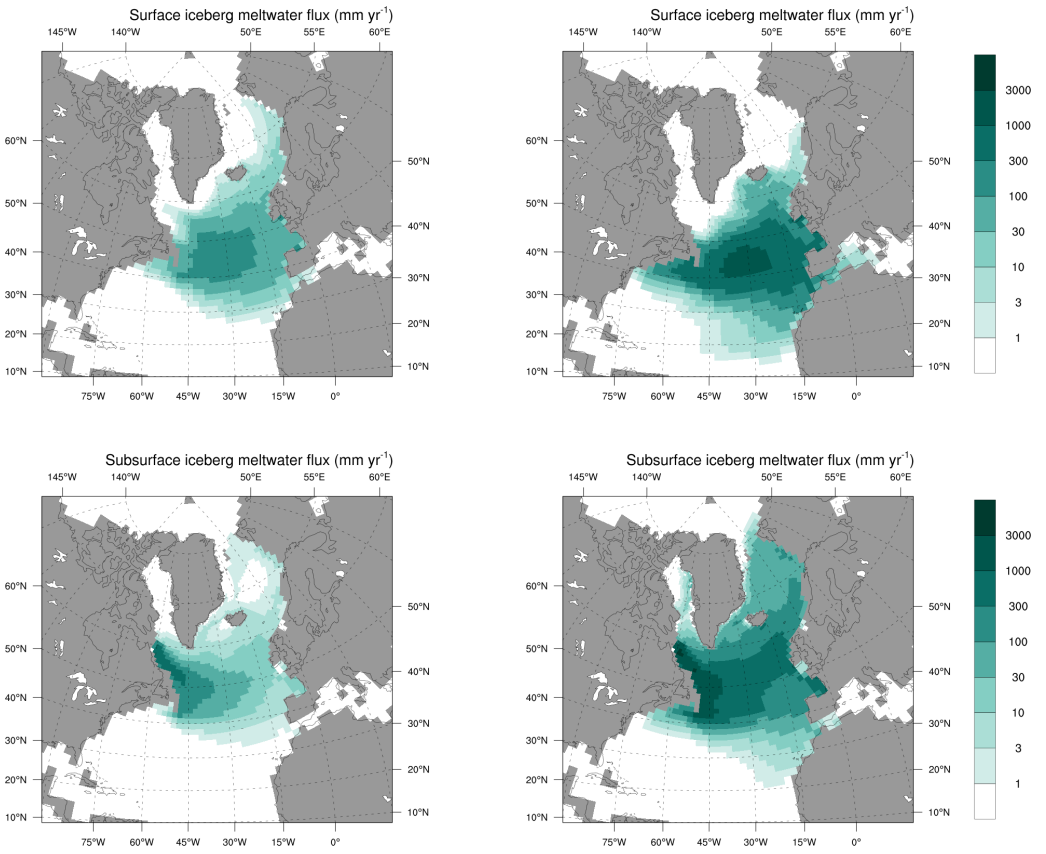

Figure 4.16: 200-years mean iceberg surface (top) and subsurface (bottom) meltwater flux (mm yr^{-1}) at the input rates of 0.04 Sv (left) and 0.31 Sv (right) in lgmIB. Note the logarithmic scale of the colorbar.

in the surface ocean (Fig. 4.13, 4.14) reduces iceberg melting, leads to an enhancement of the lifetime of iceberg, allowing them to drift further away from the release site. With an input rate increase, icebergs can drift further to the north to the Baffin Bay and slightly further to the north in the Nordic Seas. To the south, icebergs reach down to 20°N at the input rate of 0.04 Sv and 10°N at the input rate of 0.31 Sv.

Icebergs melt along their drift trajectories with the highest melting rate typically close to the calving site. Whereas in the pre-industrial iceberg hosing experiment subsurface melt of icebergs at small input rates plays only a minor role (8%), it is almost as large as the surface melt at the LGM climate (41%). The explanation is the colder surface temperatures and the strongly extended sea ice cover in the north-western Atlantic, which prevent/reduce surface relative iceberg melting in this area causing relative subsurface melt increase. In the north-east Atlantic, where the SST are warmer and no sea ice is present, surface melt contribution is dominating

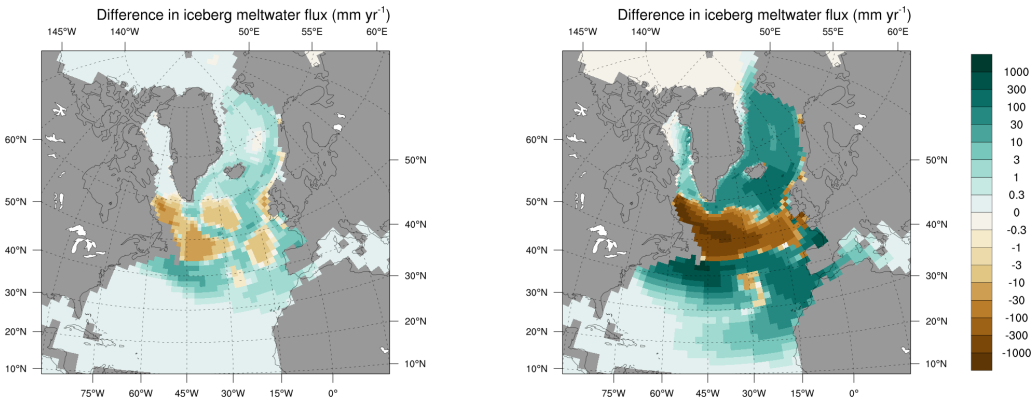

Figure 4.17: Difference in 200-years mean iceberg meltwater flux (mm yr^{-1}) between lgmIB and lgmCTRL at input rates of 0.04 Sv (left) and 0.031 Sv (right). Note the logarithmic scale of the colorbar.

the entire melt (Fig. 4.16). Another factor contributing to the dominance of surface melt in the north-eastern Atlantic is the shift in the size distribution towards smaller icebergs, typical for places far remote from the source. The shift at LGM is even enhanced due to the strong subsurface melt contribution, which effects large icebergs more than small icebergs. This indicates not only the dominant surface melting but also that mainly small iceberg capable of drifting to some remote regions. Therefore, the iceberg surface and subsurface meltwater fluxes are different. For higher input rates and colder surface conditions in the North Atlantic, the spatial distribution of iceberg melting changes, and the contribution of subsurface melt increases from 41% to 50%

To investigate the feedbacks between prescribed iceberg input rate, ocean circulation and climate change, and iceberg melting, the spatial distribution of the iceberg meltwater flux in the experiment lgmIB is compared with the corresponding distribution derived from the experiment lgmCTRL. In this experiment, the icebergs are run in diagnostic mode, that is without affecting the ocean climate. The anomalies between the run with fully coupled iceberg and the run with diagnostic icebergs shown in Fig. 4.17, 4.18. The figures demonstrate the feedback on the iceberg melt pattern. For the weak input rate of 0.04 Sv, there is less melt at the calving site and between 45° and 60°N in the northern North Atlantic in experiment lgmIB due to the cooling induced by the climate changes and the cooling due to iceberg melt. This effect is even stronger for the strong prescribed input rate of 0.31 Sv.

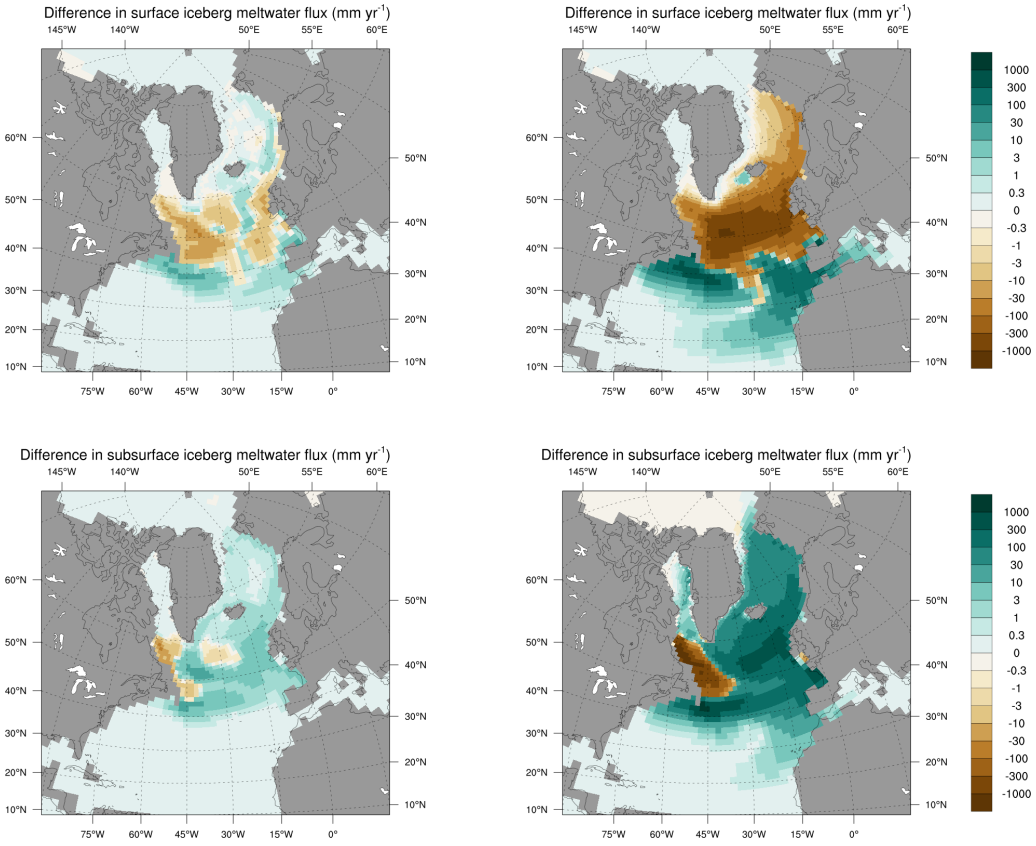

Figure 4.18: Difference in 200-years mean iceberg surface (top) and subsurface (bottom) meltwater flux (mm yr^{-1}) between lgmIB and lgmCTRL at the input rates of 0.04 Sv (left) and 0.031 Sv (right). Note the logarithmic scale of the colorbar.

Iceberg-climate feedbacks reduce surface melt north of 45°N, especially for the strong input rate case (Fig. 4.18). This is obviously an effect of the strong surface cooling due to a collapsed/weakened AMOC. Close to the calving site, there is also less subsurface melt due to the imposed cooling by melting icebergs. With prognostic icebergs, subsurface melting reduces the ocean subsurface temperature so that further melting is not possible. Reduced melt in an early part of the iceberg trajectory enhances iceberg lifetime and leads to an increase in melting further north and south. This pattern is most pronounced for the strong input rate time slice. The increase in iceberg melting and presence is relatively symmetric to the main melt latitude of 50°N. There are, however, substantial differences in the contribution from surface and subsurface melt. Whereas subsurface melt increases everywhere except close to the calving site, the anomaly of surface melt shows a clear dipole pattern, a strong reduction north of approximately 45°N and an increase south of it. Maxima are reached close to the north-

ern edge of the Gulf Stream in the west and in the trade wind regime in the east including the Canary Current. As the effect on ocean climate is larger for higher input rates, obviously the strength of the feedback on the melting of icebergs increases as well.

4.3.4 The AMOC sensitivity to latent heat needed to melt icebergs

In order to separate the role of iceberg meltwater and latent heat consumption during iceberg melting, a separate sensitivity experiment lgmIBnoLH has been conducted, where the latent heat required to melt icebergs is set to zero. Otherwise this experiment is identical to the standard iceberg hosing experiment lgmIB.

The analysis of the timeseries shown in Fig. 4.10 reveals that the strongest difference can be seen in the northern North Atlantic SST. The difference between the two experiments gets larger the more icebergs are released, in line with the growing amount of heat required to melt the icebergs. At peak input rate of 0.35 Sv including latent heat of icebergs leads to a nearly 1°C extra cooling at the ocean surface in the northern North Atlantic. The colder SSTs also leads to a local extension of the sea ice cover. Overall, the role of the iceberg latent heat is only minor causing an enhancement of iceberg lifetime that results in more iceberg meltwater accessible directly in areas of deep water formation.

To understand the effect of the iceberg latent heat, I consider the anomalies in the surface and the subsurface iceberg meltwater flux, ocean salinity, and temperature between experiments lgmIB and lgmIBnoLH at the input rate of 0.04 Sv (Fig. 4.19). Latent heat release induced cooling reduces surface melt over the northern North Atlantic between 45° and 60°N that is partly sea ice covered and subsurface melt close to the calving site in the experiment lgmIB (Fig. 4.19). Such a difference can be explained by the fact that in the experiment lgmIB, newly released icebergs relatively fast reduce ocean temperature to the freezing point when melting is no longer possible. In both experiments, icebergs melt directly in one area of deep water formation in the Nordic Seas but do not enter the Arctic due to the southward sea ice flow through Fram Strait and do not directly affect the main area of deep water formation there. Advection by ocean currents is the only way, how the meltwater can reach the Arctic. Icebergs in the experiment lgmIB are capable to melt slightly further to the north and much further to the south when compared with the experiment IBnoLH due to

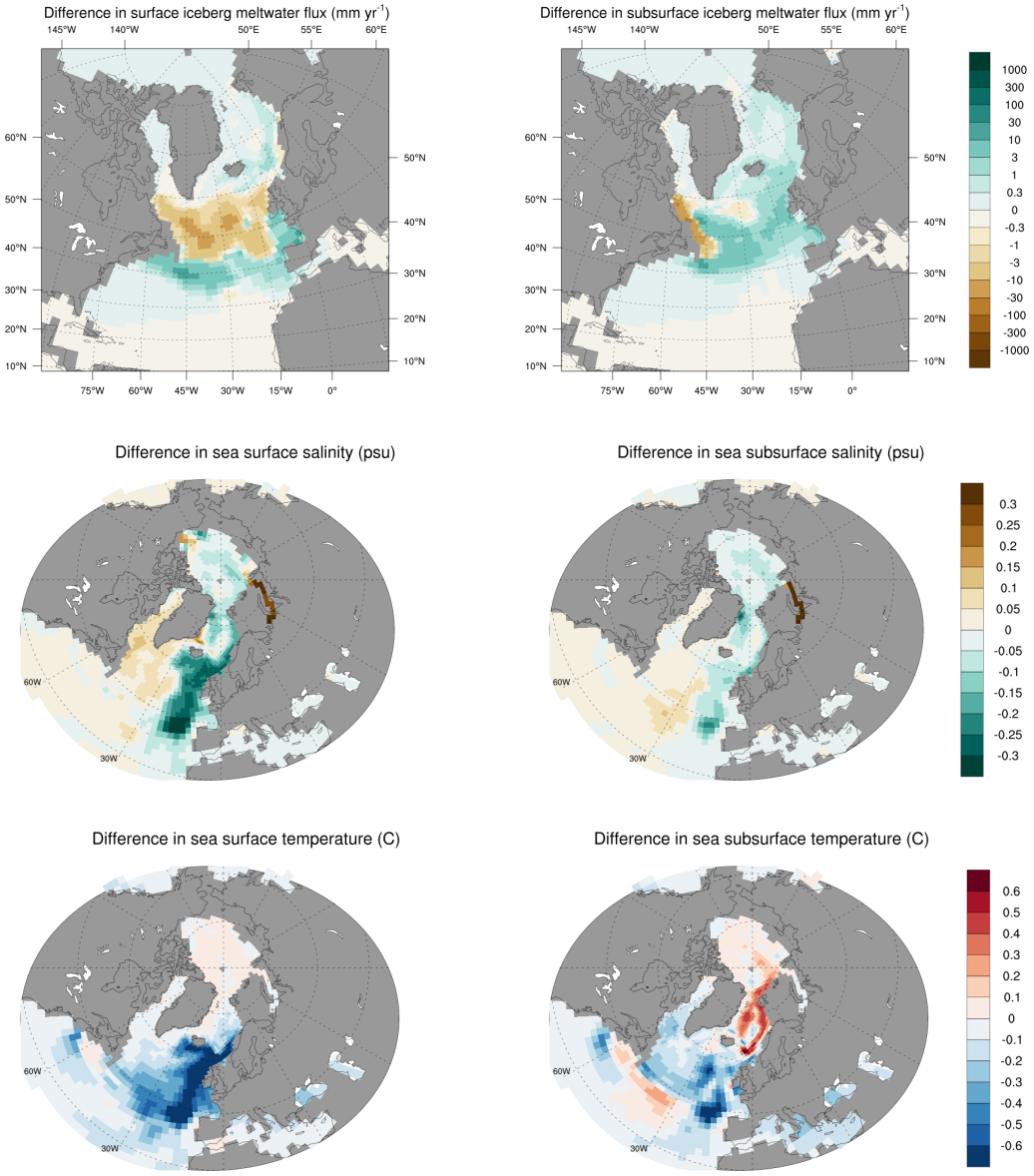

Figure 4.19: Difference in 200-years mean surface/ subsurface (left/ right) iceberg meltwater flux (mm yr^{-1}; top); surface/ subsurface salinity (psu; middle) and surface/ subsurface temperature (°C; bottom) between lgmIB and lgmIBnoLH at the input rate of 0.04 Sv. Note the logarithmic scale of the colorbar of the iceberg meltwater flux (top).

enhanced iceberg lifetime.

In the experiment lgmIB, the reduced melting in the north-western North Atlantic, to the west of 30°W, cause this area both on the surface and subsurface to be slightly more saline when compared with the experiment lgmIBnoLH (Fig. 4.19). The surface in the north-eastern North Atlantic, to the east of 30 W, is much fresher in the experiments lgmIB than in

lgmIBnoLH, indicating that more icebergs melt occurs there in addition to the meltwater that is transported by the SPG. The effect is less pronounced in the subsurface. Nevertheless, there is still more freshening in the north-eastern North Atlantic in the experiment lgmIB. Therefore, the freshening effect in areas relatively close to areas of deep water formation is stronger in the experiment lgmIB than in lgmIBnoLH, indicating that more iceberg meltwater is transported to these areas.

The experiment lgmIB shows the strongest cooling among all hosing experiments due to the additional contribution from the latent heat of iceberg melting (Fig. 4.10). As in the corresponding pre-industrial experiments, the ocean surface is cooler in areas where many icebergs melt in the experiment lgmIB as they require heat to make the melting possible. Therefore, the highest cooling is reached along the north-eastern North Atlantic. In the north-western North Atlantic, the Nordic Seas, and the Arctic the ocean surface shows very little extra cooling, as the temperature is already close to the freezing point and cannot be cooled below that point. The lower SSS in the Nordic Seas in the standard iceberg experiment lgmIB is dominated by the northward advection of fresher waters in the north-eastern North Atlantic. This stabilizes the water column and reduces the mixing with underlying warmer and saltier water masses of Atlantic origin. Thus, this waters are not cooled by contact with the atmosphere/cold ocean surface layer, but keep their somewhat warmer temperatures, what explains the pronounced positive temperature anomaly in subsurface temperatures in the Nordic Seas.

The main effect of iceberg latent heat in LGM iceberg hosing experiments is the reduced iceberg melt in the belt 40°to 60°N and the resulting shift in the melt pattern of icebergs to the north-eastern North Atlantic and into the Nordic Seas. This leads to a more efficient transport into the Nordic Seas and a strengthening in the reduction in AMOC.

4.4 The effect of the background climate

To understand the AMOC response to a different type of hosing for different background climates, I consider the AMOC profile at 26°N at two different input rates of 0.04 and 0.31 Sv (Fig. 4.20). AMOC profiles in control experiments for different climate conditions, the pre-industrial CTRL and the LGM lgmCTRL, are very similar (Fig. 4.20; dashed dark brown lines). A maximum of the NADW cell at 26°N of about 17.5 Sv is reached in 1,200

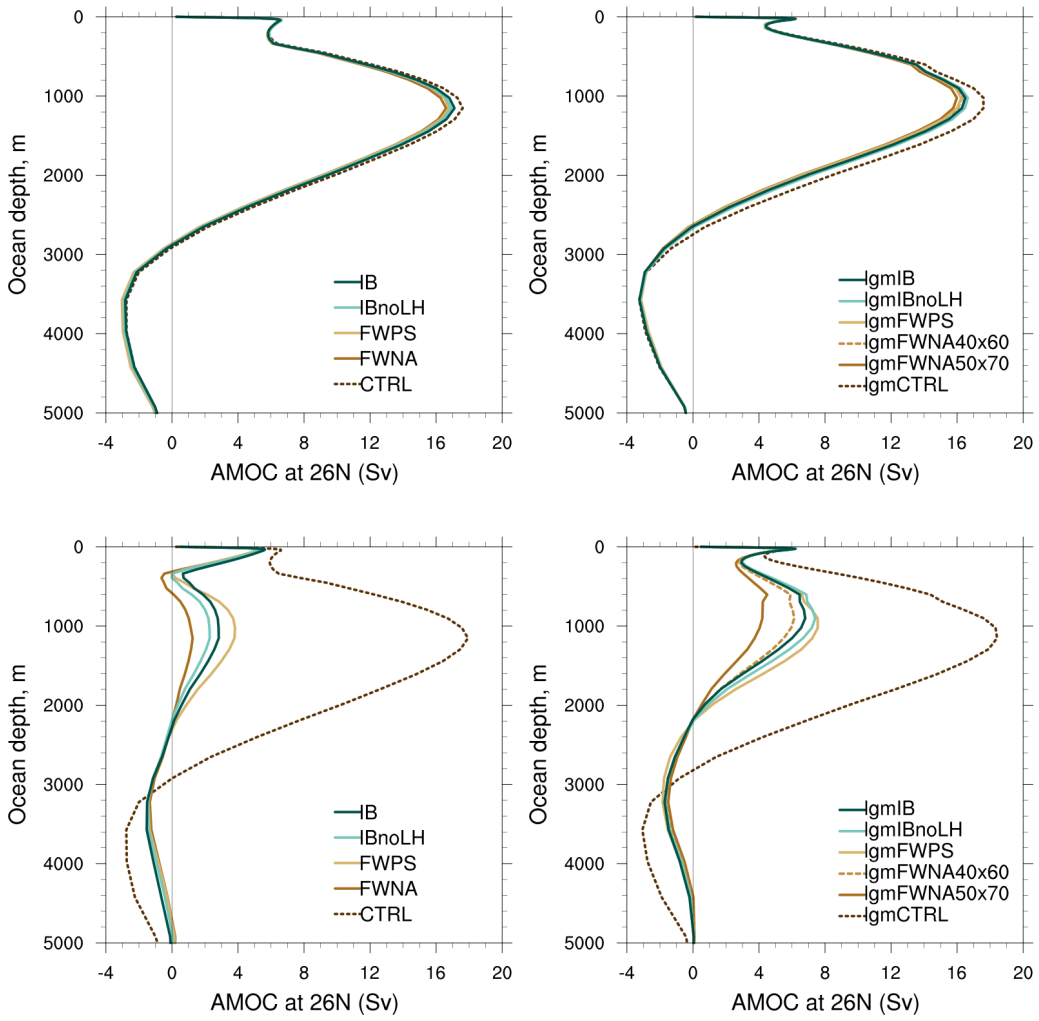

Figure 4.20: 200-years mean AMOC strength at 26°N profile (Sv) for the input rates of 0.04 Sv (top) and 0.31 Sv (bottom) for the pre-industrial (left) and the LGM (right) climate.

m in both set-ups. The maximum of the AABW cell is also similar in both control experiments and is nearly 3 Sv occurring in 3,600 m. Profiles depict differences in the NADW cell depth of nearly 200 m with the shallower NADW cell at LGM. Another difference is the depth of the wind-driven cell that is nearly 200 m deeper in the pre-industrial experiment.

At the input rate of 0.04 Sv, the AMOC strength decreases in all hosing experiments. The decrease is very similar for all hosing types for the same climate, but the rate of decrease depends on the background climate. Thus, the NADW cell maximum strength at 26°N declines to nearly 16.5 Sv for the LGM climate and only 17 Sv for the pre-industrial climate. The strength of the AABW cell almost does not change in all hosing experiments.

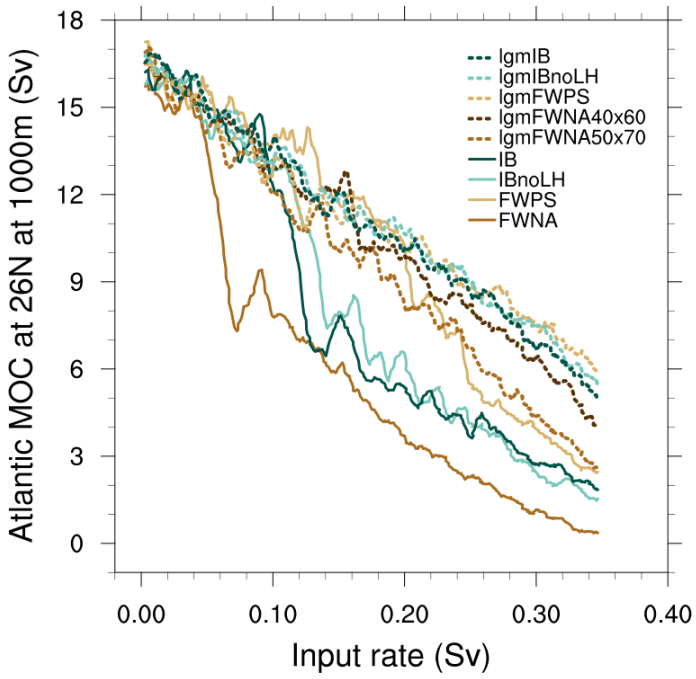

Figure 4.21: 100-years mean AMOC strength at 26°N at 1,000 m (Sv) versus the input rate (Sv) for the pre-industrial (solid lines) and the LGM (dashed lines) climate.

At the input rate of 0.31 Sv, the circulation response is much stronger for both climates. For pre-industrial, the NADW cell maximum reduces to the range 1–4 Sv depending on the type of hosing. The range for the LGM climate is higher, 4–7 Sv, indicating that the AMOC is more resistant to the hosing than in pre-industrial experiments. The AABW cell now expands upwards, reaching 2,300 m in pre-industrial and 2,100 m at LGM, respectively. The maximal strength of the AABW cell decreases to 1.5 Sv in pre-industrial and 1.7 Sv in LGM. The maximal AABW strength in LGM shifts to nearly 3,200 m, in pre-industrial it is located in the same depth. Freshwater point source experiments show the smallest response to hosing, and freshwater North Atlantic experiments show the highest decline. The AMOC response in both iceberg experiments lie in between freshwater point source and both North Atlantic experiments. For the pre-industrial climate, the experiment IBnoLH shows the strongest decline among both icebergs set-ups. At LGM, the strongest decline shows the experiment lgmIB.

Plotting directly the AMOC strength vs. the input rate (Fig. 4.21) reveals marked differences of the response from the background climate. For pre-industrial hosing one (or more) clear jumps to weaker overturning is obvious. The shape of the transition strongly depends on the hosing type.

For LGM, no clear jumps (or abrupt shifts from a strong AMOC to a weaker AMOC) are visible. The response is de facto linear. Due to the lack of jumps to a weaker AMOC modes in LGM, the remaining strength of the AMOC for strong hosing lies well above the corresponding result for pre-industrial hosing. The explanation for this different behavior lies in the sign of the feedbacks. For the pre-industrial hosing, the combination of positive freshwater hosing at high latitudes, strong temperatures restoring and the advective feedback leads to potentially multiple steady states (or at least abrupt switches from a strong AMOC mode to a weak AMOC mode and vice versa). For the LGM, in contrast, the effective net freshwater loss due to the dominance of brine release in the Arctic makes the AMOC relative stable and is effectively damping the effect of the hosing.

Overall, the AMOC response to hosing strongly depends on the type of hosing and the background climate. A hosing type defines the location of fresh/ meltwater injection, whereas the background climate defines the location of deep water formation areas and the spread of released fresh/ meltwater with currents. Altogether, this determines the relative disposition between hosing locations and deep water formation areas and the effectiveness of the ocean response to the hosing. For a small input rate, the response is more similar for the two climates, but the difference increases with the input rate increase. The sensitivity to the type of hosing is given for both background climates, however, the difference between the individual runs is much larger for pre-industrial than for LGM.

5 Long transient glacial-deglacial simulation with a coupled climate-ice sheet model with an interactive iceberg module

The goal of the development of the new iceberg module presented here was the application in new model system containing in addition to a coupled GCM components interactive coupling of ice sheets and solid earth for the simulation of the last deglaciation. Here first results from a test simulations are presented, quasi as proof of concept.

5.1 Model setup

The model system consists of the already applied in previous chapters coarse resolution version of MPI-ESM-CR-Iceberg model (GR30L40, T31, 5 iceberg classes; see chapter 2.1). The Max Planck Institute subversion of the Parallel Ice Sheet Model (PISM; Bueler and Brown, 2009; Winkelmann et al., 2011) mPISM Ziemen et al. (2014, 2019) is coupled to the model set-up. The surface mass balance of the ice sheets is calculated using an energy balance model (Kapsch et al., 2020). The model includes interactive river rerouting (Riddick et al., 2018) and interactive bathymetry generation (Meccia and Mikolajewicz, 2018). The Model set-up includes interactive glacial isostatic adjustment component, the global VIscoelastic Lithosphere and MAntle model (VILMA; Martinec, 2000). To save computational costs, here an asynchronous coupling technique has been applied (Voss and Sausen, 1996; Mikolajewicz et al., 2007) where ice sheet and solid earth run in real time with the imposed forcing, but atmosphere and ocean see the forcing accelerated by a factor of ten (like e.g. in Ziemen et al., 2014). In practice, this means that first atmosphere, ocean and land vegetation are calculated for 10 years. The forcing is then used for 100 years of ice sheet/solid earth calculation. The new topography and freshwater fluxes from the ice sheets are then applied for the simulation of the next 10 years of MPI-ESM. The iceberg module is forced with the calving flux of the ice sheet model. The iceberg meltwater flux is affecting the ocean

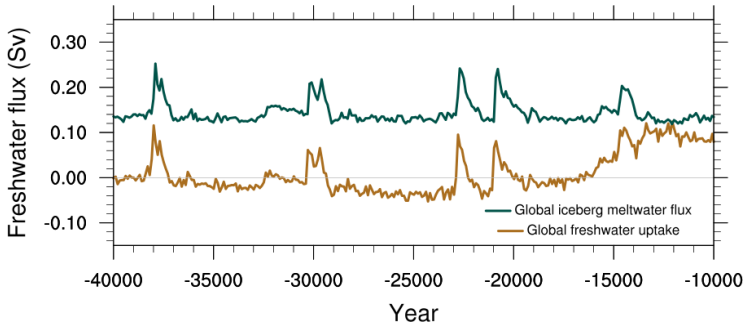

Figure 5.1: 10-years mean (ocean time scale) global freshwater uptake (Sv; brown) and global iceberg meltwater flux (Sv; green).

component. Thus, in this set-up, the iceberg forcing contains many input points and the resulting iceberg and iceberg meltwater flux distribution is realistic. As only prescribed forcing, insolation is calculated according to Berger and Loutre (1991) and atmospheric greenhouse gas concentrations are taken from Köhler et al. (2017). The simulation starts from 46,000 years BP and is integrated to present-day. Due to the acceleration in the atmosphere-ocean model, this simulation can only serve as proof of concept. The variability occurring in this simulation can be distorted by the asynchronous coupling. This is especially true for variability affecting the AMOC, e.g. "Heinrich"-like event variability.

5.2 Results from a long transient simulation

In the analysis of the transient simulation, I will only focus on the icebergs' performance in the coupled set-up. The experiment starts in the year 46,000 BP; the results here are analyzed only from year 40,000 BP, to avoid the effects of initial drift. The main goal of this simulation was the optimization of the ice sheet parameters to obtain a realistic model behavior. During the deglaciation, accelerated simulations show a delay in surface warming compared to the corresponding synchronous simulations and an artificial decoupling of the deep ocean due to the too fast surface warming (on atmosphere-ocean time scales, which is 10× shorter than the ice sheet time scale). Therefore, in the year 10,000 BP, the model set-up was artificially perturbed by replacing the transient temperature and salinity fields of the ocean with data from a synchronously coupled simulation. Therefore the data for the early Holocene will not be analyzed here. The final state, however, can be used to compare the model state with present-day

distribution of icebergs.

Fig. 5.1 shows timeseries of 100-years averages (ice sheet time-scale, corresponding to 10 atmosphere-ocean years) of the global ocean freshwater uptake (brown) and the global iceberg meltwater flux (green). The global freshwater uptake represents essentially the rate of change of the ice sheet mass. This water can either enter the ocean in liquid form, that means runoff, or in solid form as calving of icebergs. The global iceberg meltwater flux is a part of the global freshwater uptake that depicts the rate with which the iceberg meltwater is added to the ocean. This quantity depends on the total amount of icebergs in the module as well as on the climate state, which affect the iceberg lifetime. Over 30,000 years of the simulation considered here, four major events occurs which indicate strong iceberg calving events with typical amplitudes of roughly 0.1 Sv, clearly visible in both time series. These events occur in the year 38,000 BP, the year 30,000 BP, years 23,000–20,000 BP and have a typical duration between 1,000 to 3,000 years. From year 16,000 BP onward, the glacial ice sheets start to disintegrate, and the climate system performs the transition from cold glacial to warm Holocene conditions.

The strong iceberg surge events, which show the typical characteristics of HEs, have a substantial effect on the simulated climate. The melting icebergs induce surface freshening and a corresponding reduction of the surface potential density, reduction of the deep convection, AMOC strength decrease, and decrease of the northward heat transport that results in a surface cooling (not shown). With a simulated global freshwater uptake increase by 0.1 Sv, the AMOC strength decreases by 2 to 3 Sv, the SST and SSS in the North Atlantic decrease by 0.2°C and 0.04 psu, correspondingly. After the surge phase, the system returns to the state close to the state before the surge event. However, it needs to be kept in mind, that the asynchronous coupling technique here leads to substantial distortion. A discharge event of 1,000 years will be seen by atmosphere/ocean as a discharge event of 100 years. As a consequence, the amplitude of the simulated changes is strongly underestimated when compared with results of the simulated HEs (Ziemen et al., 2014, 2019).

5.3 Iceberg meltwater flux

Fig. 5.2 depicts the simulated global iceberg volume and the global iceberg meltwater flux. An increase in the global volume of icebergs in the module

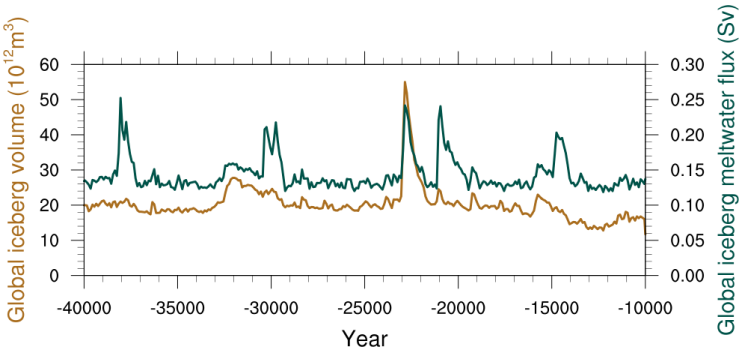

Figure 5.2: 10-year mean (ocean scale) global total iceberg volume (m^3; brown) and global iceberg meltwater flux (Sv; green).

is indicative of a strong increase in the calving flux from the ice sheets. The global iceberg meltwater flux is the flux to the ocean due to melting icebergs, similar to the one in Fig. 5.1. An increase in the global iceberg meltwater flux coincides with a global iceberg volume increase (Fig. 5.2). The latter is a consequence of ice surge events. As was shown before, there are four ice surge events on the time interval 40,000–10,000 yrs BP. The main location of the iceberg surge events is Hudson Strait, where the eastern part of the Laurentide ice sheet is undergoing periodic surge events, very similar to the ones described in Ziemen et al. (2019). The peak around 23,000 years BP shows a rather untypical behavior. Here the increase in iceberg volume is much larger than for the other events. The reason for this is the different calving site. Whereas the other events are surges through Hudson Strait with a rapid spreading (and melting) over the entire northern North Atlantic and rather fast melting, this event is caused by a strong surge to the Arctic, roughly following the path of the present-day Mackenzie river. The icebergs added to the Arctic can effectively melt only when they leave to the northern North Atlantic via the Denmark Strait as, due to cold Arctic conditions, the melting there is rather limited. Therefore, the iceberg lifetime in this event is much longer compared to the other events resulting in a much stronger iceberg volume increase compared to the other events. In the year 15,000 BP, the global iceberg volume starts gradually to decrease, whereas the global iceberg meltwater flux is almost unchanged and around 14,000 BP even increases. This is a consequence of the slow global warming due to prescribed rising atmospheric greenhouse gas concentrations.

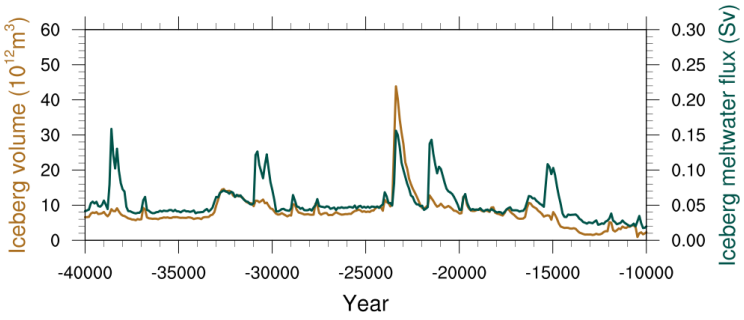

Figure 5.3: 10-years mean total iceberg volume (m^3; brown) and iceberg meltwater flux (Sv; green) in the Northern Hemisphere.

5.3.1 Northern Hemisphere

The time evolution of the Northern Hemisphere integrated values of iceberg volume and iceberg meltwater flux are very similar to the global values which just reflects the fact, that the major surge events are originating from the Laurentide ice sheet (Fig. 5.3). The integrated calving flux from Antarctica does not show marked long-term variability, inspite that it is on average higher than its Northern Hemisphere counterpart. As for the global values (Fig. 5.2), there are four events where iceberg volume in the Northern Hemisphere increases associated with ice surge events. Consequently, there are four associated events with an increased global iceberg meltwater flux. As mentioned before, the peak at 23,000 yrs BP in the iceberg volume is due to a surge event from the Laurentide ice sheet to the Arctic.

Ruddiman (1977) reconstructed the ice rafted debris (IRD) deposition rates from deep-sea sediment cores for different time slices in the North Atlantic. IRD is a proxy for the melting of icebergs. Thus the pattern should be comparable to the iceberg meltwater flux, if the terrestrial material is evenly distributed within the icebergs. Comparison of the modelled iceberg meltwater flux and the reconstructed IRD deposition rates for the two available time intervals, 40,000 to 25,000 yrs BP and 25,000 to 13,000 yrs BP (Fig. 5.4), shows that the patterns of two quantities are rather similar for both time intervals. In the earlier period (40,000–25,000 yrs BP) the modelled icebergs travel a bit further to the south than indicated by the IRD distribution. The iceberg melt is strongest in vicinity of the release sites, the main source of icebergs is located in the Labrador Sea off Hudson Strait. However, there are many other sources. IRD contours are also

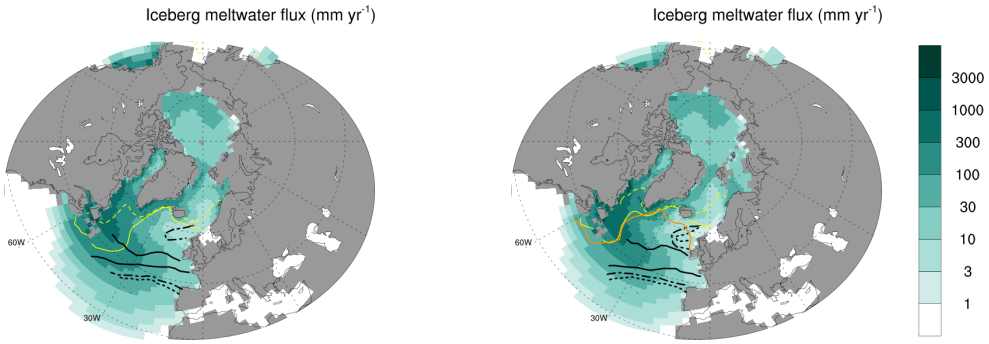

Figure 5.4: Iceberg meltwater flux (mm yr^{-1}) averaged over 40,000 to 25,000 yrs BP (left) and over 25,000 to 13,000 yrs BP (right) overlayed by mean rates of IRD deposition for the same periods from Ruddiman (1977) (black solid lines indicate deposition rates of 300 mg cm^{-2} per 1,000 yrs; black dashed-doted lines correspond to 100 mg cm^{-2} per 1,000 yrs; black dashed lines to 50 mg cm^{-2} per 1,000 yrs). Yellow lines depict simulated sea ice extent of the sea ice concentration of 15% (solid line depicts the winter extent, and dashed line depicts the summer extent). Orange line depicts the reconstructed winter sea ice extent from Ruddiman (1977). Note the logarithmic scale of the colorbar.

similar for the two time intervals with a wider range of the high IRD input in the later period, indicating a slightly more intense IRD deposition to the north-eastern North Atlantic between 25,000–13,000 yrs BP. There is the tendency for the main area of iceberg meltwater flux to be broader than the relative narrow belt of the maximal IRD deposition rate from Ruddiman's reconstruction. The reason for this could be an underestimation of the drift speed in the North Atlantic current due to the coarse model resolution. It also should be noted, that the model timing in the present set-up does not exactly follow the reconstructed and only depicts the general pattern of changes in the past. Nevertheless, the spatial distribution and the pattern of the iceberg meltwater flux to some extent follow the reconstructed IRD belt indicating that the coupled model system including the new Eulerian iceberg module is capable of producing a reasonable iceberg meltwater distribution. In the later period (25,000–13,000 yrs BP), the reconstructed winter sea ice extent is available (Fig. 5.4). It is similar to the one simulated by the model (Fig. 5.4). Reconstructed and modelled sea ice extents in the north-western North Atlantic match very well, whereas, in the north-eastern North Atlantic, the reconstructed extent reaches the British Isles and in the model, the winter sea ice margin is located a few degree further north.

Fig. 5.5 depicts timeseries of the simulated iceberg meltwater flux (left)

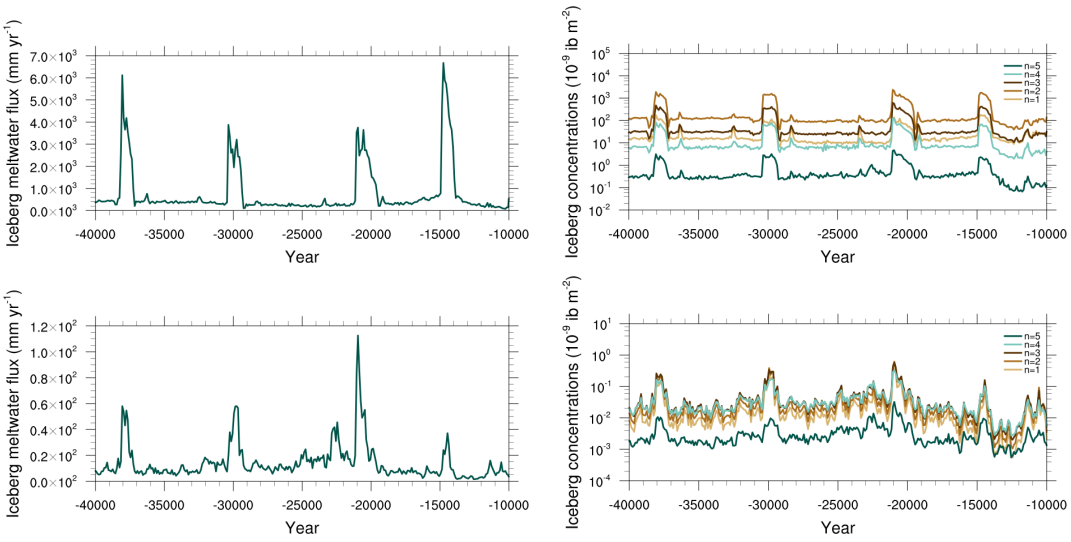

Figure 5.5: 10-years mean iceberg meltwater flux ((mm yr^{-1}; left) and iceberg concentration for every iceberg size class (right) at 60°W 60°N (first row) and 15°W 40°N (second row).

and iceberg concentrations of different iceberg size classes (right) in two locations, one in the north-western North Atlantic at 60°W 60°N (first row), the other in the north-eastern North Atlantic at 15°W 40°N (second row), relative close to the south-eastern margin of the domain with icebergs. The simulated iceberg meltwater fluxes show several abrupt increases over the entire experiment indicating four surge events. The iceberg meltwater fluxes at surge events are at least one order of magnitude larger than the background values. The corresponding changes in iceberg concentrations during surge events are typically one order of magnitude larger than the background values. The values in the north-eastern point are several orders of magnitude smaller than the values in the north-west. The simulated size distribution depends on the location. In the north-west, close to the release sites (west coast), the second iceberg size class is dominating throughout the simulation. This coincides with a dominance of this class in the prescribed distribution of the iceberg calving. The relative small size of the icebergs in this class makes them the most frequent ones in concentration in the prescribed calving, although the total contribution of this size class in terms of volume contribution is only 13% (see Table 1) and thus much less than the contribution from the larger size classes three and four. In the remote location (east coast), the number of icebergs of the size classes one to four is very similar with almost equal concentrations. The biggest iceberg size class is less present in both locations due to the

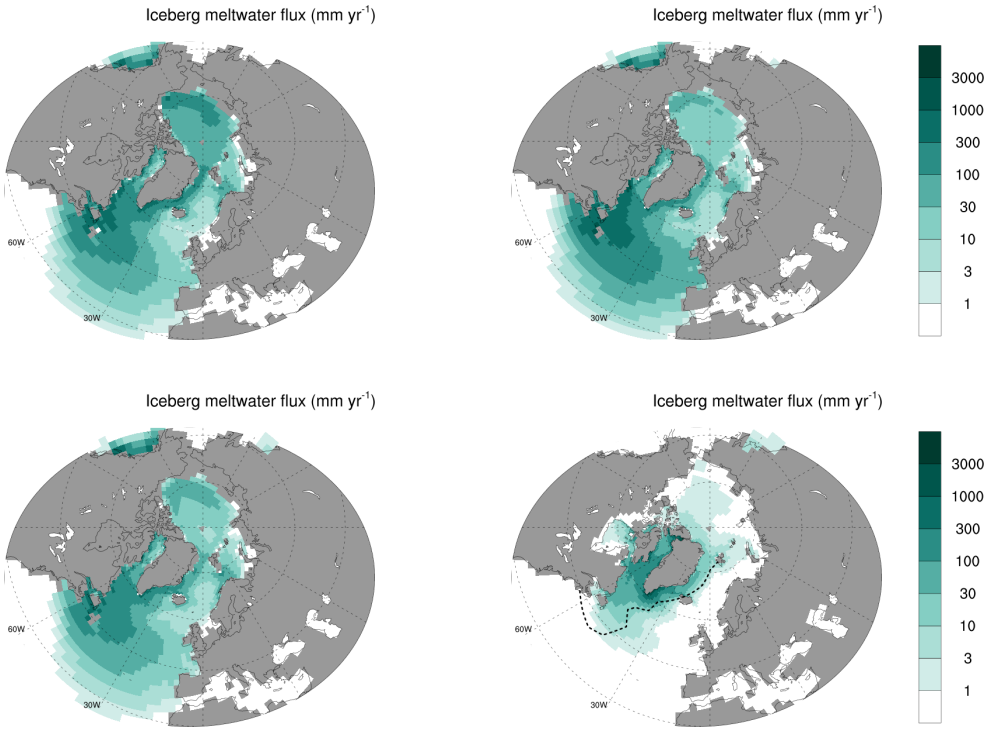

Figure 5.6: The mean iceberg meltwater flux (mm yr^{-1}) averaged before (31,000–32,000 yrs BP; top left), during (30,000–29,000 yrs BP; top right), after (28,000–27,000 yrs BP; bottom left) the ice surge event and in the end of the experiment (bottom right). Black dashed line denotes the normal iceberg extent from observations (Jongma et al., 2009). Note the logarithmic scale of the colorbar.

assumed rather small fraction of occurrence after ice sheet calving. The small icebergs have not survived the long travel to the east and most of them have melted. So the small icebergs far away from the calving sites are mostly remnants of bigger icebergs that have lost a substantial part of their size due to melting and were transferred to smaller size classes.

Fig. 5.6 depicts the iceberg meltwater flux corresponding to four different time slices, before the ice surge event (31,500 yrs BP), during the surge event (29,500 yrs BP), after the surge event (27,500 yrs BP), and at the end of the simulation at pre-industrial conditions. The last time slice shows also the observed present-day iceberg extent (Jongma et al., 2009). Due to cold conditions and strong winds, icebergs can cross the northern North Atlantic and 20°N before, during, and after the surge event. Before the surge event, the iceberg meltwater flux has a moderate extent and pattern when compared with other time slices. The strongest iceberg meltwater flux corresponds to the time slice during the ice surge event when the huge amount of icebergs are already added to the module and have

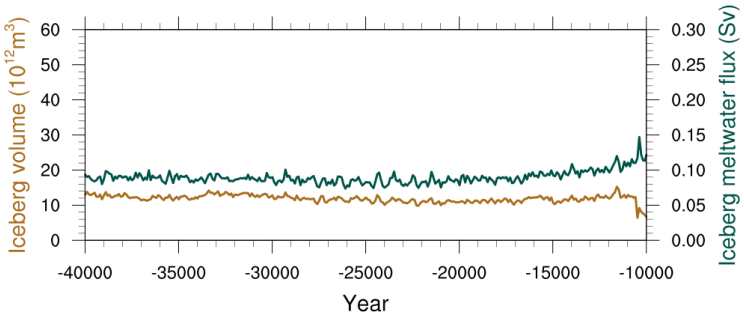

Figure 5.7: 10-years mean total iceberg volume (m^3; brown) and iceberg meltwater flux (Sv; green) in the Southern Hemisphere.

spread across the northern North Atlantic. The colder SSTs and the large amount of calved icebergs lead to a southward shift of the margin of the occurring icebergs, reaching the Canary Islands in the southeast.

At the end of the experiment, when the model has reached a new equilibrium state with warm late Holocene climate conditions and reduced wind strength, there are significantly fewer icebergs present with almost leaving Greenland as the only relevant iceberg source in the north. Icebergs now can not drift to the north-eastern North Atlantic anymore, as they did during glacial times, and reach only 40°N due to significantly warmer climate when most of the melting occurs in the vicinity of the calving sites. The iceberg meltwater flux extent lies in the agreement with the observational estimates with some deviations which can be attributed to the coarse model resolution.

5.3.2 Southern Hemisphere

The iceberg volume and the iceberg meltwater flux in the Southern Hemisphere show - in contrast to the Northern Hemisphere - no abrupt changes (Fig. 5.7). During the deglaciation, there is an increase of the iceberg meltwater flux due to the disintegration of parts of the Antarctic ice sheet as a response to warming and rising sea levels.

Fig. 5.8 depicts the distribution of iceberg meltwater flux for glacial (29,500 yrs BP; left) and late Holocene (pre-industrial; right) conditions. The latter corresponds to present-day conditions and is shown together with the observational iceberg extent (Wagner et al., 2017). Similarly to the Northern Hemisphere, the most iceberg melt takes place close to the calving sites along the margin of the Antarctic ice sheet and strongly de-

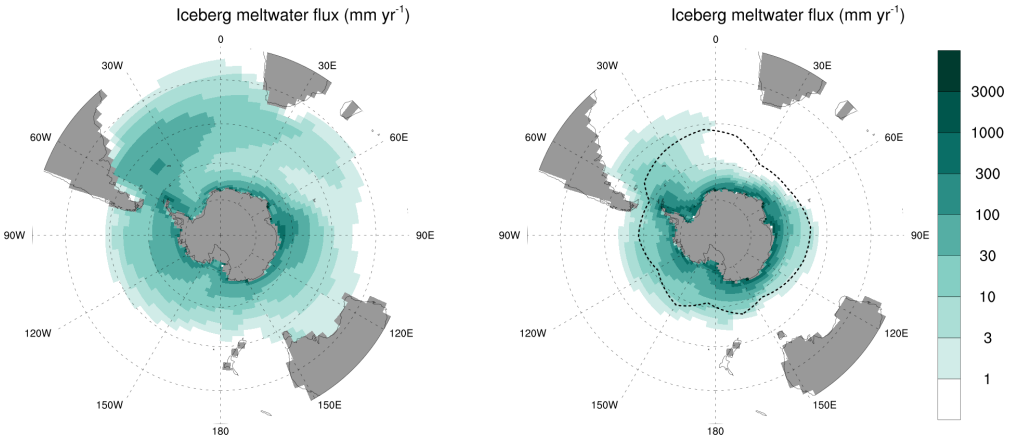

Figure 5.8: The mean iceberg meltwater flux (mm yr^{-1}) averaged during the surge event in the Northern Hemisphere (30,000–29,000 yr; left) and in the end of the experiment (right). Black dashed line denotes the normal iceberg extent from observations (Wagner et al., 2017). Note the logarithmic scale of the colorbar.

creases with the distance from calving sites. The advection in the Weddell gyre is clearly visible. During LGM, due to the cold conditions, icebergs can drift in the Atlantic as far north as 27°S. Here the Weddell gyre advects the icebergs from the Weddell ice self to the north where they are spread eastward with the Antarctic Circumpolar Current. In other regions, the extent hardly reaches 30°S. At the end of the experiment, at the new equilibrium, due to reduced ice mass release and warmer ocean, icebergs can drift only up to 40°S in the Atlantic and 50°S in other basins. The simulated iceberg meltwater flux extent lies in agreement with the observational extent with some fluctuation due to coarse model resolution.

6 Summary and Conclusions

In this work, I presented a new Eulerian iceberg module that can be used for long-term climate simulations in ESMs at low computational costs. The module allows to account for ice discharge from ice sheets into the ocean, e.g. as occurred during HEs, when huge amounts of icebergs were released into the northern North Atlantic. Previous studies have investigated HEs and their impact on the ocean circulation by directly injecting freshwater into the ocean. Depending on the location of the freshwater injection, the AMOC sensitivity is either stronger or weaker as compared to adding an actual ice mass into the ocean. As the most important aspect of icebergs is the melting, especially the iceberg meltwater flux, it is important to consider icebergs explicitly in climate models. To include interactive icebergs and account for iceberg physics, simulation of an adequate spatial distribution of the meltwater flux is therefore of great interest.

Only few recent studies of ice surge events exists, where EMICs were used together with Lagrangian iceberg modules. The Lagrangian framework allows the tracking of individual groups of icebergs and accounts for iceberg physics. However, it requires some module modifications when aiming to simulate surge event as the release of large number of icebergs leads to computationally expensive calculations. To avoid these complications, I have shown a formulation of an iceberg module in the Eulerian framework that simplifies the coupling of the iceberg module and the ocean component of the ESM. The Eulerian approach requires a reformulation of the prognostic variables: now they are iceberg concentrations and iceberg velocities. The implementation of icebergs in the Eulerian framework requires a discretization of the size distribution. Here a 1D-distribution is chosen, requiring an assumption about the relation between horizontal extent of the iceberg and its height. The transition towards the Eulerian approach allows to reduce computational costs, as it does not depend on the number of icebergs anymore (not every single iceberg is tracked) but on the number of iceberg size classes.

It is a priori not clear, what is the best choice for the number of iceberg classes and for the prescribed relation between iceberg height and horizontal dimensions. The sensitivity of the results with respect to both uncertainties were tested in a series of experiments. The findings show a rather small sensitivity to the iceberg height parameterization. This in-

dicates that the exponential parameterization of iceberg height is a good choice as it provides a reasonable interaction with the ocean interior. The module is more sensitive to the choice of the number of iceberg size classes. A small number of iceberg size classes (two and three) results in unrealistically large amounts of meltwater release close to calving sites. This can be solved by increasing the number of size classes, which, in turn, requires more computational time. For more than five size classes, the improvement by adding additional classes is small. Therefore, the exponential iceberg height parameterization and five iceberg size classes are a good trade-off between the computational costs and the realism of the distribution of meltwater flux produced by the Eulerian iceberg module. For validation of the Eulerian iceberg module, present-day calving fluxes from Antarctica and Greenland are prescribed as forcing. The results show a realistic distribution of the iceberg meltwater flux.

To understand the effect of icebergs on HEs simulated with a climate model and to answer the research questions formulated in the introduction, I performed two sets of experiments with the coupled MPI-ESM-CR-Iceberg set-up for different climate conditions, pre-industrial and LGM. Both sets of experiments include classical freshwater point source and freshwater latitude belt hosing experiments as well as two iceberg experiments. The iceberg experiments comprise one full iceberg set-up and a set-up that accounts only for the iceberg meltwater spatial distribution and does not include the latent heat component needed to melt iceberg. For each climate condition, a control experiment was performed. Control experiments include diagnostic icebergs to discern the effect of circulation changes due to melting icebergs and changes in the iceberg meltwater spatial distribution induced by circulation changes. All experiments undergo the same perturbation with a slowly increasing and then decreasing input rate. The main goal of these experiments is to understand the effect of the background climate on the iceberg meltwater pattern and how different hosing interacts with the climate system depending on the background climate.

The LGM climate is significantly different from the pre-industrial climate, with a much colder and saline ocean. Another difference between the two simulations with a different background climate is in the mechanism and the location of the deep water formation. For the pre-industrial climate, the AMOC is thermally driven with the main deep water formation site in the Nordic Seas. For the LGM, it is driven by brine release with the main deep water formation site in the Arctic. This results in a different

sensitivity of the AMOC to hosing and quite different feedbacks.

RQ 1 How does the climate system response differ to hosing as icebergs rather than as a direct freshwater input?

The evaluation of the AMOC sensitivity to hosing applied as a direct freshwater injection or as iceberg discharge shows that the response of the AMOC is sensitive to the type of hosing. Such sensitivity to the type of hosing was investigated in a similar experiment using EMICs coupled to Lagrangian iceberg modules and showed similar results (e.g., Bigg et al., 2011; Jongma et al., 2013). The general mechanism for the interaction between hosing and the ocean does not depend on hosing type. Fresh/meltwater in areas of deep water formation causes the surface water density to decrease and, therefore, a stabilization of the water column that induces a weakening of the AMOC resulting in a reduction of the northward heat transport and the ocean cooling. The type of hosing defines the location of the injection and, therefore, the amount of fresh/meltwater that reaches areas of deep water formation. Thus, the injection of freshwater close to deep water formation areas results in a relatively high rate of water column stratification and a strong AMOC response. The injection in remote from deep water formation areas locations results in only a part of the released freshwater transport to these areas, leading to a slower rate of water column stratification there and a weak AMOC response. Iceberg drift redistributes hosing from the calving sites to the locations of deep water formation, where the icebergs melt and the meltwater becomes effective for the ocean.

The pre-industrial experiments show a hysteresis response to hosing (increase of input rate followed by a decrease), with a delay in the return to the initial state. Abrupt AMOC decreases occur, when the prescribed hosing exceeds certain values, henceforth called collapse rates. Depending on the hosing type and location of the fresh/meltwater input, the collapse rates differ by half an order of magnitude, between 0.046 Sv and 0.19 Sv for both freshwater injection experiments. The collapse rate for the iceberg experiments lies in the middle ($\sim$0.10 Sv). A typical collapse occurs in this model when the AMOC strength decreases abruptly from 11–15 Sv to 6–8 Sv. Slowly decreasing input rate leads to a recovery of the AMOC, typically with an abrupt increase for input rates smaller than a critical

value, termed recovery rate. Recovery rates for the freshwater experiments typically lie between 0.09–0.16 Sv. Freshwater experiments again show the smallest and the highest recovery rates, and iceberg experiments perform in the middle. The AMOC recovery occurs abruptly from a strength of 7.5–8 Sv to 13–15 Sv. In the pre-industrial experiments, no stable AMOC in a range 8–11 Sv is simulated, indicating that there are no multiple steady states. These results indicate that the sensitivity of the AMOC response to hosing depends on the type of hosing.

The LGM experiments show a similar response of the AMOC, namely, a slowing down of the AMOC with an increase in the input rate. However, no abrupt transitions occur and the response to the hosing is rather linear and there is no hysteresis response to the hosing. Besides that, the sensitivity to the type of hosing is much smaller than for the pre-industrial climate. For LGM, brine release in the Arctic is the dominant factor in the freshwater budget of the Arctic. A slowing down of the AMOC leads to longer residence times of water in the Arctic, that - unlike the situation in the pre-industrial climate - leads to an accumulation of salt due to the brine release, a feedback dampening the effect of the hosing on the AMOC. Deep water formation occurs rather far away from the location of fresh/meltwater input, therefore the type of hosing does not matter much. Similarly to the pre-industrial experiments, there are no indications of multiple steady-states. A similar AMOC response to hosing as a direct freshwater injection for different climate conditions was found by Ganopolski and Rahmstorf (2001).

When icebergs melt, they extract heat from the ocean. To evaluate the effect of the additional heat loss, I performed two iceberg experiments with and without the latent heat loss from the ocean. The findings show that the major component determining AMOC changes is the spatial distribution of the meltwater. The spatial distribution determines the amount of meltwater that is transported to areas of deep water formation where it stabilizes the water column. The latent heat has the opposite effect on the ocean, as surface cooling destabilizes the water column. Hence, it partly compensates for the stabilization due to surface freshening. However, the additional ocean cooling also leads to an increase of the lifetime of iceberg and to a melting further away from the calving site. Therefore, more meltwater is reaching the

sites of NADW formation in the simulation including the latent heat effect. The simulation with all iceberg processes included leads to a more effective water column stratification in the deep water formation areas. The additional ocean heat loss also results in enhanced sea ice coverage in the northern North Atlantic. The latent heat effect is similar for both, pre-industrial and LGM experiments. Therefore, it is important to account for latent heat in the iceberg module.

The Eulerian iceberg module accounts for the physical mechanism behind the iceberg's lifetime, thereby, providing an adequate spatial meltwater flux across the ocean. Including an interactive Eulerian iceberg module, that accounts for the latent heat of melt, in MPI-ESM allows for an adequate modeling of calved ice from ice sheets and to simulate ice surge events, such as HEs.

RQ 2 What is the effect of the background climate on the iceberg meltwater flux? How does the background climate affect the climate system response to different type of hosing?

The iceberg meltwater flux spatial distribution, surface, and subsurface iceberg meltwater fluxes are significantly different for pre-industrial and LGM conditions. They also differ significantly depending on the input rate. As compared to pre-industrial, in LGM simulations the cold ocean surface lead to significant increase in the iceberg lifetime and strong winds allows icebergs to drift farther away from calving sites. The vertical distribution of iceberg meltwater flux is also dependent on the background climate: at LGM there is less melt on the surface and more melt in the subsurface when compared to pre-industrial. The same is true within the same time slice for different input rates: with an input rate increase, the ocean becomes colder and fresher that results in changes in the iceberg meltwater flux. Therefore, the simulated iceberg meltwater flux strongly depends on ocean circulation and climate. Assuming a fixed meltwater flux pattern would distort the system response to hosing.

The background climate also determines the mechanism, locations, and the strength of deep water formation. The AMOC response to hosing strongly depends on the relative distance between release sites and deep water formation areas. The AMOC either collapses abruptly, when an input rate reaches a collapse rate (pre-industrial) or shows a rather gradual response to increasing input rate without

clear collapses. Whereas in the pre-industrial simulation, NADW is formed in the Nordic Seas by open ocean convection in a region of net freshwater gain by the ocean, deep water in the LGM simulations is formed in the Arctic under sea ice due to brine release. Whereas in the pre-industrial simulation, hosing is amplifying negative perturbations of the surface salinity, in the LGM simulations it is rather damping them, resulting in a more stable system. Therefore, the background climate also defines efficiency of fresh/ meltwater interaction with the ocean.

RQ 3 Can the iceberg module reproduce a plausible iceberg meltwater flux over glacial simulations?

In the end, a long transient simulation with a coupled MPI-ESM-CR-Iceberg module was performed covering the last 46,000 years. The experimental set-up also includes interactive ice sheets, glacial isostatic adjustment, interactive river rerouting, and bathymetry. Including an interactive Eulerian iceberg module within such a model set-up for a long simulation covering glacial and deglacial periods allows for a physically more complete representation of ice surge events. Here the iceberg surges are no longer prescribed, but they are a result of internal variability of the coupled model system, originating from simulated surge events of ice sheet. In earlier model version, the calved ice mass was treated as a direct freshwater injection at the calving sites. This resulted in a strongly simplified and distorted representation of the interaction between icebergs and the ocean.

Over the entire experiment, the model undergoes four major surge events with calved ice mass treated as interactive icebergs. All surge events occur in the Northern Hemisphere and cause a temporal weakening of the AMOC. Over the entire experiments, the iceberg meltwater flux responds to changes in the ocean circulation with a wide iceberg spread across the ocean during the cold glacial phase and significantly reduced spread during the warm late Holocene period. In the pre-industrial climate, the ocean is much warmer and only the Antarctic and Greenland ice sheets are present. During this time, the iceberg meltwater flux extent shrinks as the total iceberg volume is reduced and most of the melting occurs close to the calving sites. Both, the simulated past and present-day iceberg meltwater flux extents lie within the reconstructed past extent and observational present-day

extent. This shows that the Eulerian iceberg module is capable of simulating a realistic climate-dependent iceberg meltwater flux.

To summarize, I designed the Eulerian iceberg module and integrated it into the ocean component of MPI-ESM. The Eulerian iceberg module produces a reasonable iceberg meltwater flux and can be used in transient long-term simulations with the coupled MPI-ESM-Iceberg set-up at low computational costs. Horizontal and vertical distribution of iceberg meltwater flux strongly depends on the background climate and changes with changes in the ocean circulation. Hosing experiments for different climate conditions were conducted to compare the effect of icebergs versus the classical freshwater hosing. In the classical freshwater hosing approaches, the AMOC response is either too strong or to weak, as the direct freshwater injection either exaggerates freshwater transport to areas of deep water formation or underestimates it. Implementing icebergs into the model produces a better spatial meltwater patterns and, therefore, results in a more adequate description of the icebergs interaction with the ocean. The results emphasize that it is essential to include iceberg modules into ESMs for long-term climate studies, especially when aiming at simulating ice surge events. Further studies with an interactive Eulerian iceberg module should include:

1. Sensitivity experiments under different background climates.

2. Sensitivity experiments with different hosing locations. Thus, running experiments for LGM climate conditions with a different hosing location, e.g. in the Arctic (Mackenzie River), close to the main area of deep water formation, could show a different sensitivity with, e.g. abrupt changes like for the pre-industrial climate.

3. Their combinations, e.g., a set of sensitivity experiments for the same background climate but with hosing in different locations.

4. Transient experiments to compare the effect of freshwater versus iceberg hosing. So far, only the transient experiment with an interactive iceberg presented in this thesis exists. Conducting such experiments in different coupled model setups might allow to investigate uncertainties due to the underlying model components.

5. Hosing experiments with a focus on the Southern Hemisphere and the role of icebergs in the AABW formation. Including icebergs into the

set-up can result in a better representation of the ocean circulation in the Southern Ocean.

6. Previous studies have also shown that AMOC sensitivity varies for different climate models (e.g., Stouffer et al., 2006). Therefore, these studies of "Heinrich"-like events as a direct freshwater injection should be revised as forcing with icebergs results in a different AMOC sensitivity.

Abbreviations and symbols

Abbreviations

1D	One dimensional
2D	Two dimensional
3D	Three dimensional
AABW	Antarctic Atlantic Bottom Water
AMOC	Atlantic Meridional Circulation
CMIP	Climate Model Intercomparison Project
CR	Coarse Resolution
ECHAM6	Atmospheric component of MPI-ESM
EMIC	Earth Models of Intermediate Complexity
ESM	Earth System Model
JSBACH	Land component of MPI-ESM
GCM	General Circulation Model
HE	Heinrich Event
HD	the river runoff module in MPI-ESM
IRD	Ice Rafted Debris
LGM	Last Glacial Maximum
MPI-ESM	Max Planck Institute Earth System Model
MPI-OM	Ocean component of MPI-ESM
NADW	North Atlantic Deep Water
OASIS3	The atmosphere and the ocean coupler in MPI-ESM
PISM	Parallel Ice Sheet Model
mPISM	Max Planck Institute subversion of Parallel Ice Sheet Model
PMIP	Paleo Model Intercomparison Project
SPG	SubPolar Gyre
STG	SubTropical Gyre
SSS	Sea Surface Salinity
SST	Sea Surface Temperature
VILMA	VIscoelastic Lithosphere and MAntle model

Physical Constants

a	the wave amplitude
A_{si}	the sea ice concentration
$C(n)$	the iceberg concentration
$c_{a,h}$	the horizontal air drag coefficient
$c_{a,v}$	the vertical air drag coefficient
c_r	the wave radiation coefficient
$c_{si,v}$	the vertical sea ice drag coefficients
$c_{w,h}$	the horizontal water drag coefficient
$c_{w,v}$	the vertical water drag coefficient
$\vec{F}_a(n)$	the air drag
$\vec{F}_w(n)$	the water drag
$\vec{F}_{si}(n)$	the sea ice drag
$\vec{F}_r(n)$	the wave radiation force
$\vec{F}_p(n)$	the pressure gradient
$\vec{F}_{cor}(n)$	the Coriolis force
$\vec{g}$	the Earth gravity
$H(k)$	the height of the iceberg in the ocean layer k
$H(n)$	the height of an iceberg
H_k	the iceberg keel height
H_{max}	the maximal height of the biggest iceberg size class
H_s	the iceberg sail height
H_{si}	the sea ice thickness
k	the ocean layer index ($k = \overline{1; k_{bot}}$)
k_{sf}	the surface ocean velocity
k_{bot}	the ocean layer index corresponding to the bottom of the iceberg
L_c	the cutoff length
L_t	the upper wave limit
L_w	the wave length
$L(n)$	the length of an iceberg
$m(n)$	the mass of an iceberg
$M_{bc}(n)$	the mass loss due to the buoyant convection
$M_{bas}(n)$	the basal melt
$M_{we}(n)$	the mass loss due to the wave erosion
n	iceberg size class ($n = \overline{1; N}$)
N	the total number of iceberg size classes in the model
Ω	the Earth rate of rotation
ϕ	the latitude in radians
P	the measure of resistance of sea ice
P^*	the sea ice strength threshold value
ρ_a	the density of air

ρ_{ice}	the ice density
ρ_{si}	the sea ice density
ρ_w	the water density
S_s	the sea state function
dt	the time step
T_{ib}	the iceberg temperature ($-4.0°C$)
T_{freeze}	the ocean freezing temperature ($-1.9°C$)
T_{sf}	the ocean surface temperature
$T_w(k)$	the ocean temperature of the layer k
$\vec{v}_a$	the air velocity
$\vec{v}_{dr}(n)$	the iceberg drift velocity
$\vec{v}(n)$	the iceberg velocity
$\vec{v}_{si}$	the sea ice velocity
$\vec{v}_w$	the ocean velocity of the ocean layer k
$V(n)$	the volume of an iceberg
$V_{melt}(n)$	the melted volume of an iceberg
$V_{source}(n)$	the iceberg volume of a class n added due to ice sheet calving
$W(n)$	the width of an iceberg
W_{min}	the minimal iceberg width
ζ	the sea surface elevation

List of Figures

List of Tables

References

Alley, R. B. and Clark, P. U.: The deglaciation of the northern hemisphere: a global perspective, Annual Review of Earth and Planetary Sciences, 27, 149–182, 1999.

Andrews, J. T. and Voelker, A. H.: "Heinrich events"(& sediments): A history of terminology and recommendations for future usage, Quaternary Science Reviews, 187, 31–40, 2018.

Arakawa, A. and Lamb, V. R.: Computational design of the basic dynamical processes of the UCLA general circulation model, General circulation models of the atmosphere, 17, 173–265, 1977.

Bamber, J., den Broeke, M., Ettema, J., Lenaerts, J., and Rignot, E.: Recent large increases in freshwater fluxes from Greenland into the North Atlantic, Geophysical Research Letters, 39, 2012.

Berger, A. and Loutre, M.-F.: Insolation values for the climate of the last 10 million years, Quaternary Science Reviews, 10, 297–317, 1991.

Bigg, G. R. and Wilton, D. J.: Iceberg risk in the Titanic year of 1912: was it exceptional?, Weather, 69, 100–104, 2014.

Bigg, G. R., Wadley, M. R., Stevens, D. P., and Johnson, J. A.: Modelling the dynamics and thermodynamics of icebergs, Cold Regions Science and Technology, 26, 113–135, 1997.

Bigg, G. R., Levine, R. C., and Green, C. L.: Modelling abrupt glacial North Atlantic freshening: rates of change and their implications for Heinrich events, Global and Planetary Change, 79, 176–192, 2011.

Bigg, G. R., Cropper, T., O'Neill, C. K., Arnold, A. K., Fleming, A. H., Marsh, R., Ivchenko, V., Fournier, N., Osborne, M., and Stephens, R.: A model for assessing iceberg hazard, Natural Hazards, pp. 1–24, 2018.

Böhm, E., Lippold, J., Gutjahr, M., Frank, M., Blaser, P., Antz, B., Fohlmeister, J., Frank, N., Andersen, M., and Deininger, M.: Strong and deep Atlantic meridional overturning circulation during the last glacial cycle, Nature, 517, 73–76, 2015.

Bond, G., Heinrich, H., Broecker, W., Labeyrie, L., McManus, J., Andrews, J., Huon, S., Jantschik, R., Clasen, S., Simet, C., et al.: Evidence for massive discharges of icebergs into the North Atlantic ocean during the last glacial period, Nature, 360, 245–249, 1992.

Bond, G. C. and Lotti, R.: Iceberg discharges into the North Atlantic on millennial time scales during the last glaciation, Science, 267, 1005–1010, 1995.

Broecker, W. S.: The great ocean conveyor, Oceanography, 4, 79–89, 1991.

Broecker, W. S., Andree, M., Bonani, G., Wolfli, W., Oeschger, H., Klas, M., Mix, A., and Curry, W.: Preliminary estimates for the radiocarbon age of deep water in the glacial ocean, Paleoceanography, 3, 659–669, https://doi.org/10.1029/PA003i006p00659, URL https://agupubs.onlinelibrary.wiley.com/doi/abs/10.1029/PA003i006p00659, 1988.

Bueler, E. and Brown, J.: Shallow shelf approximation as a "sliding law" in a thermodynamically coupled ice sheet model, J. Geophys. Res., 114, https://doi.org/10.1029/2008JF001179, URL http://www.agu.org/pubs/crossref/2009/2008JF001179.shtml, 2009.

Bügelmayer, M., Roche, D., and Renssen, H.: Representing icebergs in the i LOVECLIM model (version 1.0)–a sensitivity study, Geoscientific Model Development, 8, 2139, 2015.

Bügelmayer-Blaschek, M., Roche, D. M., Renssen, H., and Andrews, J. T.: Internal ice-sheet variability as source for the multi-century and millennial-scale iceberg events during the Holocene? A model study, Quaternary Science Reviews, 138, 119–130, 2016.

Clark, P. U., Pisias, N. G., Stocker, T. F., and Weaver, A. J.: The role of the thermohaline circulation in abrupt climate change, Nature, 415, 863–869, 2002.

Clarke, G. K. and La Prairie, D. I.: Modelling iceberg drift and ice-rafted sedimentation, in: Continuum mechanics and applications in geophysics and the environment, pp. 183–200, Springer, 2001.

Death, R., Siegert, M. J., Bigg, G. R., and Wadley, M. R.: Modelling iceberg trajectories, sedimentation rates and meltwater input to the ocean from the Eurasian Ice Sheet at the Last Glacial Maximum, Palaeogeography, Palaeoclimatology, Palaeoecology, 236, 135–150, 2006.

Diemand, D.: Icebergs.[w:] Encyclopedia of Ocean Sciences, 2001.

Dowdeswell, J., Maslin, M., Andrews, J., and McCave, I.: Iceberg production, debris rafting, and the extent and thickness of Heinrich layers (H-1, H-2) in North Atlantic sediments, Geology, 23, 301–304, 1995.

Dowdeswell, J. A. and Forsberg, C. F.: The size and frequency of icebergs and bergy bits derived from tidewater glaciers in Kongsfjorden, northwest Spitsbergen, Polar Research, 11, 81–91, 1992.

El-Tahan, M., Venkatesh, S., and El-Tahan, H.: Validation and quantitative assessment of the deterioration mechanisms of Arctic icebergs, Journal of Offshore Mechanics and Arctic Engineering, 109, 102–108, 1987.

Ganopolski, A. and Rahmstorf, S.: Rapid changes of glacial climate simulated in a coupled climate model, Nature, 409, 153–158, 2001.

Gladstone, R. M., Bigg, G. R., and Nicholls, K. W.: Iceberg trajectory modeling and meltwater injection in the Southern Ocean, Journal of Geophysical Research: Oceans, 106, 19 903–19 915, 2001.

Gregory, J., Saenko, O., and Weaver, A.: The role of the Atlantic freshwater balance in the hysteresis of the meridional overturning circulation, Climate dynamics, 21, 707–717, 2003.

Hagemann, S. and Dümenil, L.: A parametrization of the lateral waterflow for the global scale, Climate dynamics, 14, 17–31, 1997.

Heinrich, H.: Origin and consequences of cyclic ice rafting in the northeast Atlantic Ocean during the past 130,000 years, Quaternary research, 29, 142–152, 1988.

Hibler, W. D.: A Dynamic Thermodynamic Sea Ice Model, Journal of Physical Oceanography, 9, 815–846, URL https://doi.org/10.1175/1520-0485(1979)009<0815:ADTSIM>2.0.CO;2, 1979.

Hill, J. C. and Condron, A.: Subtropical iceberg scours and meltwater routing in the deglacial western North Atlantic, Nature Geoscience, 7, 806, 2014.

Hunke, E. C. and Comeau, D.: Sea ice and iceberg dynamic interaction, Journal of Geophysical Research: Oceans, 116, 2011.

Jongma, J., Renssen, H., and Roche, D.: Simulating Heinrich event 1 with interactive icebergs, Climate Dynamics, 40, 1373–1385, 2013.

Jongma, J. I., Driesschaert, E., Fichefet, T., Goosse, H., and Renssen, H.: The effect of dynamic–thermodynamic icebergs on the Southern Ocean climate in a three-dimensional model, Ocean Modelling, 26, 104–113, 2009.

Jungclaus, J., Keenlyside, N., Botzet, M., Haak, H., Luo, J.-J., Latif, M., Marotzke, J., Mikolajewicz, U., and Roeckner, E.: Ocean circulation and tropical variability in the coupled model ECHAM5/MPI-OM, Journal of climate, 19, 3952–3972, 2006.

Jungclaus, J., Fischer, N., Haak, H., Lohmann, K., Marotzke, J., Matei, D., Mikolajewicz, U., Notz, D., and Storch, J.: Characteristics of the ocean simulations in the Max Planck Institute Ocean Model (MPIOM) the ocean component of the MPI-Earth system model, Journal of Advances in Modeling Earth Systems, 5, 422–446, 2013.

Kageyama, M., Merkel, U., Otto-Bliesner, B., Prange, M., Abe-Ouchi, A., Lohmann, G., Ohgaito, R., Roche, D., Singarayer, J., Swingedouw, D., et al.: Climatic impacts of fresh water hosing under Last Glacial Maximum conditions: a multi-model study, Climate of the Past, 9, 935–953, 2013.

Kageyama, M., Harrison, S. P., Kapsch, M.-L., Löfverström, M., Lora, J. M., Mikolajewicz, U., Sherriff-Tadano, S., Vadsaria, T., Abe-Ouchi, A., Bouttes, N., et al.: The PMIP4-CMIP6 Last Glacial Maximum experiments: preliminary results and comparison with the PMIP3-CMIP5 simulations, Climate of the Past, 2020.

Kapsch, M.-L., Mikolajewicz, U., Ziemen, F. A., Rodehacke, C. B., and Schannwell, C.: Analysis of the Surface Mass Balance for Deglacial Climate Simulations, The Cryosphere Discussions, pp. 1–40, 2020.

Keghouche, I., Bertino, L., and Lisæter, K. A.: Parameterization of an iceberg drift model in the Barents Sea, Journal of Atmospheric and Oceanic Technology, 26, 2216–2227, 2009.

Klockmann, M.: The AMOC and its sensitivity to different climate forcings in the range of glacial to modern conditions, Ph.D. thesis, Universität Hamburg Hamburg, 2017.

Kohfeld, K. E., Fairbanks, R. G., Smith, S. L., and Walsh, I. D.: Neogloboquadrina pachyderma (sinistral coiling) as paleoceanographic tracers in polar oceans: Evidence from Northeast Water Polynya plankton tows,

sediment traps, and surface sediments, Paleoceanography, 11, 679–699, 1996.

Köhler, P., Nehrbass-Ahles, C., Schmitt, J., Stocker, T. F., and Fischer, H.: A 156 kyr smoothed history of the atmospheric greenhouse gases CO2, CH4, and N2O and their radiative forcing, Earth System Science Data, 9, 363–387, 2017.

Levine, R. C. and Bigg, G. R.: Sensitivity of the glacial ocean to Heinrich events from different iceberg sources, as modeled by a coupled atmosphere-iceberg-ocean model, Paleoceanography and Paleoclimatology, 23, 2008.

Lichey, C. and Hellmer, H. H.: Modeling giant-iceberg drift under the influence of sea ice in the Weddell Sea, Antarctica, Journal of Glaciology, 47, 452–460, 2001.

Lynch-Stieglitz, J.: The Atlantic meridional overturning circulation and abrupt climate change, Annual review of marine science, 9, 83–104, 2017.

MacAyeal, D.: Binge/purge oscillations of the Laurentide ice sheet as a cause of the North Atlantic's Heinrich events, Paleoceanography, 8, 775–784, 1993.

Maier-Reimer, E. and Mikolajewicz, U.: Experiments with an OGCM on the cause of the Younger Dryas, Max-Planck-Institut für Meteorologie Hamburg, 1989.

Marsh, R., Ivchenko, V., Skliris, N., Alderson, S., Bigg, G. R., Madec, G., Blaker, A. T., Aksenov, Y., Sinha, B., Coward, A. C., et al.: NEMO–ICB (v1. 0): interactive icebergs in the NEMO ocean model globally configured at eddy-permitting resolution, Geoscientific Model Development, 8, 1547, 2015.

Marsland, S. J., Haak, H., Jungclaus, J. H., Latif, M., and Röske, F.: The Max-Planck-Institute global ocean/sea ice model with orthogonal curvilinear coordinates, Ocean modelling, 5, 91–127, 2003.

Martin, T. and Adcroft, A.: Parameterizing the fresh-water flux from land ice to ocean with interactive icebergs in a coupled climate model, Ocean Modelling, 34, 111–124, 2010.

Martinec, Z.: Spectral–finite element approach to three-dimensional viscoelastic relaxation in a spherical earth, Geophysical Journal International, 142, 117–141, 2000.

Mauritsen, T., Bader, J., Becker, T., Behrens, J., Bittner, M., Brokopf, R., Brovkin, V., Claussen, M., Crueger, T., Esch, M., et al.: Developments in the MPI-M Earth System Model version 1.2 (MPI-ESM1. 2) and its response to increasing CO2, Journal of Advances in Modeling Earth Systems, 11, 998–1038, 2019.

McManus, J. F., Francois, R., Gherardi, J.-M., Keigwin, L. D., and Brown-Leger, S.: Collapse and rapid resumption of Atlantic meridional circulation linked to deglacial climate changes, Nature, 428, 834–837, 2004.

Meccia, V. L. and Mikolajewicz, U.: Interactive ocean bathymetry and coastlines for simulating the last deglaciation with the Max Planck Institute Earth System Model (MPI-ESM-v1. 2), Geoscientific Model Development, 11, 4677–4692, 2018.

Mikolajewicz, U. and Maier-Reimer, E.: Mixed boundary conditions in ocean general circulation models and their influence on the stability of the model's conveyor belt, Journal of Geophysical Research: Oceans, 99, 22 633–22 644, 1994.

Mikolajewicz, U., Gröger, M., Maier-Reimer, E., Schurgers, G., Vizcaíno, M., and Winguth, A. M.: Long-term effects of anthropogenic CO 2 emissions simulated with a complex earth system model, Climate Dynamics, 28, 599–633, 2007.

Mountain, D.: On predicting iceberg drift, Cold Regions Science and Technology, 1, 273–282, 1980.

Muglia, J. and Schmittner, A.: Glacial Atlantic overturning increased by wind stress in climate models, Geophysical Research Letters, 42, 9862–9868, 2015.

Otto-Bliesner, B. L. and Brady, E. C.: The sensitivity of the climate response to the magnitude and location of freshwater forcing: last glacial maximum experiments, Quaternary Science Reviews, 29, 56–73, 2010.

Peltier, W. R., Vettoretti, G., and Stastna, M.: Atlantic meridional overturning and climate response to Arctic Ocean freshening, Geophysical Research Letters, 33, https://doi.org/10.1029/

2005GL025251, URL https://agupubs.onlinelibrary.wiley.com/doi/abs/10.1029/2005GL025251, 2006.

Rackow, T., Wesche, C., Timmermann, R., Hellmer, H. H., Juricke, S., and Jung, T.: A simulation of small to giant Antarctic iceberg evolution: Differential impact on climatology estimates, Journal of Geophysical Research: Oceans, 122, 3170–3190, 2017.

Rahmstorf, S.: On the freshwater forcing and transport of the Atlantic thermohaline circulation, Climate Dynamics, 12, 799–811, 1996.

Rahmstorf, S.: Ocean circulation and climate during the past 120,000 years, Nature, 419, 207–214, 2002.

Reick, C., Raddatz, T., Brovkin, V., and Gayler, V.: Representation of natural and anthropogenic land cover change in MPI-ESM, Journal of Advances in Modeling Earth Systems, 5, 459–482, 2013.

Riddick, T., Brovkin, V., Hagemann, S., and Mikolajewicz, U.: Dynamic hydrological discharge modelling for coupled climate model simulations of the last glacial cycle: the MPI-DynamicHD model version 3.0, Geoscientific Model Development, 11, 4291–4316, 2018.

Rignot, E., Jacobs, S., Mouginot, J., and Scheuchl, B.: Ice-shelf melting around Antarctica, Science, 341, 266–270, 2013.

Roberts, W. H., Valdes, P. J., and Payne, A. J.: A new constraint on the size of Heinrich Events from an iceberg/sediment model, Earth and Planetary Science Letters, 386, 1–9, 2014.

Roche, D. M., Paillard, D., Caley, T., and Waelbroeck, C.: LGM hosing approach to Heinrich Event 1: results and perspectives from data–model integration using water isotopes, Quaternary Science Reviews, 106, 247–261, 2014.

Röske, F.: An Atlas of surface fluxes based on the ECMWF Re-Analysis: a climatological dataset to force global ocean general circulation models, Max-Planck-Institut für Meteorologie Hamburg, 2001.

Ruddiman, W. F.: Late Quaternary deposition of ice-rafted sand in the subpolar North Atlantic (lat 40 to 65 N), Geological Society of America Bulletin, 88, 1813–1827, 1977.

Sarnthein, M., Jansen, E., Weinelt, M., Arnold, M., Duplessy, J. C., Erlenkeuser, H., Flatøy, A., Johannessen, G., Johannessen, T., Jung, S., et al.: Variations in Atlantic surface ocean paleoceanography, 50°-80° N: A time-slice record of the last 30,000 years, Paleoceanography, 10, 1063–1094, 1995.

Savage, S.: Aspects of iceberg deterioration and drift, in: Geomorphological Fluid Mechanics, pp. 279–318, Springer, 2001.

Schiller, A., Mikolajewicz, U., and Voss, R.: The stability of the North Atlantic thermohaline circulation in a coupled ocean-atmosphere general circulation model, Climate Dynamics, 13, 325–347, 1997.

Schmittner, A., Meissner, K., Eby, M., and Weaver, A.: Forcing of the deep ocean circulation in simulations of the Last Glacial Maximum, Paleoceanography, 17, 5–1, 2002.

Schneck, R., Reick, C. H., and Raddatz, T.: Land contribution to natural CO2 variability on time scales of centuries, Journal of Advances in Modeling Earth Systems, 5, 354–365, 2013.

Smith, R. S. and Gregory, J. M.: A study of the sensitivity of ocean overturning circulation and climate to freshwater input in different regions of the North Atlantic, Geophysical research letters, 36, 2009.

Smith, S. D.: Hindcasting iceberg drift using current profiles and winds, Cold regions science and technology, 22, 33–45, 1993.

Stevens, B., Giorgetta, M., Esch, M., Mauritsen, T., Crueger, T., Rast, S., Salzmann, M., Schmidt, H., Bader, J., Block, K., et al.: Atmospheric component of the MPI-M Earth system model: ECHAM6, Journal of Advances in Modeling Earth Systems, 5, 146–172, 2013.

Stickley, C. E., St John, K., Koç, N., Jordan, R. W., Passchier, S., Pearce, R. B., and Kearns, L. E.: Evidence for middle Eocene Arctic sea ice from diatoms and ice-rafted debris, Nature, 460, 376–379, 2009.

Stommel, H.: Thermohaline convection with two stable regimes of flow, Tellus, 13, 224–230, 1961.

Stouffer, R. J., Yin, J., Gregory, J. M., Dixon, K. W., Spelman, M. J., Hurlin, W., Weaver, A. J., Eby, M., Flato, G. M., Hasumi, H., Hu, A., Jungclaus, J. H., Kamenkovich, I. V., Levermann, A., Montoya, M., Murakami, S.,

Nawrath, S., Oka, A., Peltier, W. R., Robitaille, D. Y., Sokolov, A., Vettoretti, G., and Weber, S. L.: Investigating the Causes of the Response of the Thermohaline Circulation to Past and Future Climate Changes, Journal of Climate, 19, 1365–1387, https://doi.org/10.1175/JCLI3689.1, URL https://doi.org/10.1175/JCLI3689.1, 2006.

Tarasov, L., Dyke, A. S., Neal, R. M., and Peltier, W. R.: A data-calibrated distribution of deglacial chronologies for the North American ice complex from glaciological modeling, Earth and Planetary Science Letters, 315, 30–40, 2012.

Turnbull, I. D., Fournier, N., Stolwijk, M., Fosnaes, T., and McGonigal, D.: Operational iceberg drift forecasting in Northwest Greenland, Cold Regions Science and Technology, 110, 1–18, 2015.

Ullman, D. J., LeGrande, A. N., Carlson, A. E., Anslow, F. S., and Licciardi, J. M.: Assessing the impact of Laurentide Ice Sheet topography on glacial climate, Climate of the Past, 10, 487–507, https://doi.org/10.5194/cp-10-487-2014, URL https://cp.copernicus.org/articles/10/487/2014/, 2014.

Valcke, S.: The OASIS3 coupler: a European climate modelling community software, Geoscientific Model Development, 6, 373–388, 2013.

Voigt, I., Cruz, A., Mulitza, S., Chiessi, C. M., Mackensen, A., Lippold, J., Antz, B., Zabel, M., Zhang, Y., Barbosa, C., et al.: Variability in mid-depth ventilation of the western Atlantic Ocean during the last deglaciation, Paleoceanography, 32, 948–965, 2017.

Voss, R. and Sausen, R.: Techniques for asynchronous and periodically synchronous coupling of atmosphere and ocean models, Climate Dynamics, 12, 605–614, 1996.

Wagner, T. J., Dell, R. W., and Eisenman, I.: An analytical model of iceberg drift, Journal of Physical Oceanography, 47, 1605–1616, 2017.

Weber, S. L., Drijfhout, S. S., Abe-Ouchi, A., Crucifix, M., Eby, M., Ganopolski, A., Murakami, S., Otto-Bliesner, B., and Peltier, W. R.: The modern and glacial overturning circulation in the Atlantic ocean in PMIP coupled model simulations, Climate of the Past, 3, 51–64, URL https://hal.archives-ouvertes.fr/hal-00298062, 2007.

Weeks, W. and Mellor, M.: Some Elements of Iceberg Technology, CRREL Report, 1978.

Wiersma, A. P. and Jongma, J. I.: A role for icebergs in the 8.2 ka climate event, Climate dynamics, 35, 535–549, 2010.

Winkelmann, R., Martin, M. A., Haseloff, M., Albrecht, T., Bueler, E., Khroulev, C., and Levermann, A.: The Potsdam Parallel Ice Sheet Model (PISM-PIK) Part 1: Model description, The Cryosphere, 5, 715–726, URL http://www.the-cryosphere.net/5/715/2011/tc-5-715-2011.pdf, 2011.

Yu, E.-F., Francois, R., and Bacon, M. P.: Similar rates of modern and last-glacial ocean thermohaline circulation inferred from radiochemical data, Nature, 379, 689–694, 1996.

Ziemen, F., Rodehacke, C., and Mikolajewicz, U.: Coupled ice sheet–climate modeling under glacial and pre-industrial boundary conditions, Climate of the Past, 10, 1817–1836, 2014.

Ziemen, F., Kapsch, M.-L., Klockmann, M., and Mikolajewicz, U.: Heinrich events show two-stage climate response in transient glacial simulations, Climate of the Past, 15, 153–168, 2019.

Acknowledgements

I am grateful to many people without whose support and counsel writing this dissertation would not be possible.

First of all, I want to thank my supervisor Uwe Mikolajewicz for guiding me through this journey, always having open doors for any question, and sharing knowledge with me. Not only do you irradiate professionalism and knowledge but also a good sense of humor and critical thinking, which is a necessary property to a researcher. I learned a lot during our regular discussions on both scientific and daily matters. I am very thankful to my co-supervisor Gerhard Schmiedl and Advisory Panel chair Hartmut Graßl for kind, friendly, and very productive meetings during the course of this research. This helped me a lot in staying on the right track. I also would like to thank my examination committee Uwe Mikolajewicz, Gerhard Schmiedl, Hartmut Graßl, Felix Ament, and Dirk Notz for the fruitful final disputation and evaluation of my research.

Next, my daily and scientific life would be much more complicated without the support from the IMPRS office. Thank you, Antje, Connie, and Michaela, your organizational work is unprecedented!

Many thanks go to current and former members of the Ocean physics group, I am very proud to be a part of it and pleased to meet all of you. Marie and Virna, it was a great pleasure to share the office with you and have nice conversations! I am especially thankful to Marie and Clemens for reading and commenting on this thesis, your input is significant and I gained valuable pieces of knowledge from our discussions.

I would also like to thank the MPI twitter team for our weekly brainstorming ideas on how to communicate science. It was a great pleasure and fun to be a part of the team and contribute to the MPI twitter development from the very beginning.

Last but not least, I thank my family, especially my mom Irina and my parents-in-law Galina and Igor, and my friends for constant support and for believing in me, and my cat for being fluffy! And Yaroslav, I am especially thankful that you are always by my side and keep the home warm while I am in science, without your love and support my life would be less colorful.

Versicherung an Eides statt

Versicherung an Eides statt Declaration of oath Hiermit versichere ich an Eides statt, dass ich die vorliegende Dissertation mit dem Titel: "A new Eulerian iceberg module for climate studies: Formulation and application to the investigation of the sensitivity of the AMOC to iceberg calving" selbstständig verfasst und keine anderen als die angegebenen Hilfsmittel – insbesondere keine im Quellenverzeichnis nicht benannten Internet-Quellen – benutzt habe. Alle Stellen, die wörtlich oder sinngemäß aus Veröffentlichungen entnommen wurden, sind als solche kenntlich gemacht. Ich versichere weiterhin, dass ich die Dissertation oder Teile davon vorher weder im In- noch im Ausland in einem anderen Prüfungsverfahren eingereicht habe und die eingereichte schriftliche Fassung der auf dem elektronischen Speichermedium entspricht.

Hamburg, den 11.08.2020

Olga Erokhina

Hinweis / Reference

Die gesamten Veröffentlichungen in der Publikationsreihe des MPI-M
„Berichte zur Erdsystemforschung / Reports on Earth System Science“,
ISSN 1614-1199

sind über die Internetseiten des Max-Planck-Instituts für Meteorologie erhältlich:
http://www.mpimet.mpg.de/wissenschaft/publikationen.html

All the publications in the series of the MPI -M
„Berichte zur Erdsystemforschung / Reports on Earth System Science“,
ISSN 1614-1199

are available on the website of the Max Planck Institute for Meteorology:
http://www.mpimet.mpg.de/wissenschaft/publikationen.html